



UNIVERSITÀ  
DEGLI STUDI  
DI PADOVA

**UNIVERSITÀ DEGLI STUDI DI PADOVA**

DIPARTIMENTO DI INGEGNERIA INDUSTRIALE DII

DIPARTIMENTO DI TECNICA E GESTIONE DEI SISTEMI INDUSTRIALI

CORSO DI LAUREA MAGISTRALE IN INGEGNERIA MECCANICA

**THERMOMECHANICAL AND MICROSCOPY  
INVESTIGATION OF FATIGUE DAMAGE  
DEVELOPMENT IN A 3D E-GLASS/EPOXY WOVEN  
COMPOSITE**

*Relatore: Prof. Marino Quaresimin*

*Relatore Estero: Prof. Stephen Louis Ogin*

*Laureanda: ELISA NOVELLO 1058716*

ANNO ACCADEMICO 2013-2014



*Ai miei genitori*



# Contents

Abstract .....	9
<b>INTRODUCTION .....</b>	<b>I</b>
<b>CHAPTER 1 Literature review .....</b>	<b>1</b>
1.1 Introduction .....	1
1.2 Classification of composite systems.....	1
1.3 2D Reinforcement Structure: Woven Fabric.....	2
1.3.1 Plain weave.....	3
1.3.2 Twill weave .....	4
1.3.3 Satin weaves .....	4
1.4 Translaminar-reinforced composites: through-thickness stitched and z-pinned composites ..	5
1.5 3D unitary textile preforms .....	6
1.5.1 Weaves .....	6
1.5.2 Knits .....	7
1.5.3 Braids.....	8
1.6 History and applications of 3D composites.....	10
1.7 2D versus 3D composites .....	11
1.7.1 Studies of comparison between 3D and 2D composites.....	13
1.8 Comparison between elastic modulus and fatigue performance of 3D woven, stitched and pinned composite.....	17
1.9 Microstructure of 3D woven composite specimen.....	19
1.10 Development of damage in 3D woven composite.....	20
1.11 Thermographic observations on damage evolution.....	23
<b>CHAPTER 2 Materials and experimental methods.....</b>	<b>25</b>
2.1 Introduction .....	25
2.2 Materials and experimental methods.....	25
2.3 Fiber volume fraction measurement.....	28
2.4 Preparation of test-specimens.....	29
2.5 Quasi-static and tensile fatigue tests.....	30
2.6 Optical and scanning electron microscopy.....	32
2.7 Scanning Electron Microscope.....	34
2.8 X-ray Micro Computed Tomography.....	35
2.9 Thermographic observations .....	37

2.10	Summary .....	38
<b>CHAPTER 3 Characterization of the microstructure .....</b>		<b>39</b>
3.1	Introduction .....	39
3.2	Architecture of the fabricated composite .....	39
3.3	Fiber volume fraction determination .....	43
3.4	Defects of the fabricated material: voids and micro delamination .....	45
3.5	Summary .....	49
<b>CHAPTER 4 Quasi-static tensile test results .....</b>		<b>51</b>
4.1	Introduction .....	51
4.2	Response of the material tested in the warp direction .....	51
4.3	Response of the material tested in the weft direction .....	55
4.4	Comparison between warp and weft direction .....	59
4.5	Concluding remarks .....	61
<b>CHAPTER 5 Tensile-tensile fatigue tests-low stress results .....</b>		<b>63</b>
5.1	Introduction .....	63
5.2	Mechanical investigation: energy dissipation and stiffness reduction .....	63
5.2.1	Fatigue at a peak stress of 150 MPa .....	66
5.2.2	Fatigue at a peak stress of 100 MPa .....	68
5.2.3	Fatigue at a peak stress of 75 and 50 MPa .....	69
5.2.4	Comparison of fatigue behaviour for the warp direction at different peak stresses .....	71
5.3	Optical and scan electron microscopy investigation .....	70
5.4	Fatigue tests at 150 MPa, interrupted at different number of cycles .....	73
5.4.1	Fatigue at a peak stress of 150 MPa stopped after 300 cycles .....	76
5.4.2	Fatigue at a peak stress of 150 MPa stopped after 5000 cycles .....	78
5.4.3	Fatigue at a peak stress of 150 MPa stopped after 100'000 cycles .....	80
5.5	Concluding remarks .....	79
<b>CHAPTER 6 Tensile-tensile fatigue tests – high stress results .....</b>		<b>81</b>
6.1	Introduction .....	81
6.2	Response of the material tested along warp direction .....	81
6.2.1	S-N curve .....	81
6.2.2	Mechanical investigation: energy dissipation and stiffness reduction .....	84
6.2.3	Investigation of damage development .....	88
6.2.4	Width effects in the fatigue of warp samples .....	91
6.3	Response of the material tested along weft direction .....	93
6.3.1	S-N curve .....	93

6.3.2	Mechanical investigation: energy dissipation and stiffness reduction .....	95
6.3.3	Investigation of damage development.....	99
6.3.4	Width effect in the fatigue of weft samples.....	102
6.4	Concluding remarks .....	103
<b>CHAPTER 7 Thermographic observations .....</b>		<b>107</b>
7.1	Introduction .....	107
7.2	Temperature evolution of early stages of damage.....	107
7.3	Thermo-mechanical response of the material during fatigue life.....	110
7.4	Concluding remarks .....	115
<b>CHAPTER 8 Conclusions and further work .....</b>		<b>117</b>
8.1	Conclusions .....	117
8.2	Further work.....	119
Appendix A Definitions .....		121
Appendix B Quasi-static tensile tests .....		123
Appendix C Fatigue tensile- tensile tests .....		127
Appendix D Optical micrographs.....		131
Appendix E Micro CT images.....		135
<b>REFERENCES .....</b>		<b>137</b>





# Abstract

In this work damage development of a glass/epoxy non-crimp 3D orthogonal woven fabric composite during fatigue life has been examined.

The material was firstly characterized determining the average fiber volume fraction while the internal structure of untested specimens was examined by means of optical microscopy. Pre-existing defects were thus detected, such as voids and micro-delaminations, due possibly to thermal shrinkage occurring in the course of the curing process.

Results of preliminary quasi-static tensile tests performed in both principal in-plane directions are then presented, verifying a different response depending on the loading direction.

Fatigue behavior of the material has been hence investigated, measuring stiffness reduction and energy dissipation, represented by the enclosed area of stress/strain hysteresis loops. Three stages characterizing fatigue lifetime could therefore be distinguished, singularly investigated combining optical and scanning electron microscopy with X-ray micro computed tomography and were found to be characterized by different damage mechanisms.

In particular, in the later stage the presence of extensive fibre fracture into warp tows closest to z-crown was detected as the principal mechanism leading the specimens to final failure.

To get further information on the events preceding the ultimate failure, an IR thermal camera was then used during fatigue tests, allowing the in situ detection of failure zones. The combination of the nondestructive techniques of thermography and X-ray micro CT tomography, will assist to reach a comprehensive damage mapping, especially during the latest stages of life.



# Introduction

Technological development has been made possible by innovations and progresses achieved in the field of materials. This has permitted to respond to the quests of improved performance that structural engineering needed, including less weight, more strength and stiffness. Composites have thus represented the result of the effort to satisfy the demands of high-performance engineering materials. The combination of different constituents in a unique structure, in fact, has allowed to obtain new materials characterized by properties superior to those of the individual components. To the overall benefits guaranteed by composite material, the flexibility of design has to be added, since a composite material can be effectively tailored to suit a particular design need.

In modern times the use of composites have become widespread, especially in the form of fibre-reinforced polymers, finding applications either in technological advanced fields, such as military markets, recreational marine, wind energy and aerospace or in consumer sports goods, such as tennis racquets, baseball bats, skis, helmets and bicycle frames. Today the most common form in which composite materials are present, is constituted by laminate structures, based on the stacking at different orientations of layers of unidirectional fibers. However, a problem that afflicts 2D laminates consists of their poor impact damage resistance that, combined with the proneness to delamination, represents the most common cause of failure. A remedy came with the use of 3D woven fabrics incorporating through-thickness reinforcements which, providing a bridging action of z-binders across delamination cracks, allowed to achieve a higher damage tolerance. The advantages given by 3D composites are not limited to delamination suppression, since they additionally improve fracture toughness, impact, ballistic and blast performances.

Despite the advantages and potential benefits, however, these materials haven't found yet many commercial applications, due mainly to the lack of an extensive database of their properties, particularly regarding the fatigue effects. In fact, even if significant progresses have been made for quasi-static loading cases, literature is still scarce in the fatigue field.

Therefore, this project is set within the scientific actual background aiming to increase the knowledge about the development of fatigue damage for glass/epoxy non crimp 3D

orthogonal woven fabric composite, through an investigation that combines the use of optical microscopy, X-ray micro computed tomography, scan electron microscopy and thermography.

The structure of this thesis is as follows.

Chapter 1 presents a literature review ranging over the description of the most common 2D and 3D composite systems and their comparison.

Chapter 2 describes materials and experimental techniques involved in this project. It begins with the presentation of the non-crimp single ply 3D orthogonal reinforcement (provided by 3TEX Inc, USA) and the matrix of Shell Epikote 828 (Bisphenol-A) epoxy resin, for then spacing through the set up definition used for quasi-static and fatigue tests and for subsequent investigations conducted by optical and scan electron microscopy, X-ray micro-computed tomography and thermography.

Chapter 3 deals with the structure characterization, presenting the architecture of the fabricated composites and including the illustration of typical defects observed into untested specimens, such as voids and micro-delaminations. Furthermore, since the material has been characterized in terms of total fibre content of the material (volume fraction), the results of the burn off tests have been presented.

In Chapter 4, the outcomes of quasi-static tensile tests are reported. These have been carried out in both warp and weft directions, for which mechanical properties and damage development have been discussed and then compared each other.

Chapter 5 involves the presentation of fatigue tests results performed into warp results at low stress levels. A mechanical investigation is followed by a damage development detection carried out through the use of images collected by optical and scanning electron microscopy.

The results obtained from fatigue tests performed at high stress levels along both the directions have been reported in Chapter 6. This opens with the representation of S N curves obtained for the two cases, for then continuing with a mechanical investigation concerning the trend of energy dissipation and stiffness reduction and finally concludes with an analysis of

damage development. Moreover, preliminary considerations on the possible presence of a width effect have been draft.

In Chapter 7, thermographic observations are reported. The main effort was directed to verify the existence of a connection between temperature evolution and the structure of the composite material. A second issue dealt regarded the research of possible similarities that were shared between temperature evolution trend and energy dissipation recorded at the elapsing during fatigue life-time.

Finally, in Chapter 8 conclusions on emerged results have been drawn as well as suggestions on possible further future work.



# Chapter 1

## Literature review

### 1.1 Introduction

The present chapter provides an overview on the recent literature regarding studies conducted on 3D composite materials. After an initial classification of composite textile systems, principal 2D woven fabrics are illustrated, followed by a description of different 3D composite systems currently available. The outcomes of experimental studies comparing features of 2D and 3D composites are then presented, with particular attention to the behaviour of 3D woven orthogonal composites, since they constitute the object of research of this work.

### 1.2 Classification of composite systems

An initial classification of composite textile system based on the form in which the reinforcement is present in the composite material is reported in Table 1.1. Type I, which is representative of composite textile systems made of chopped fiber, is not generally suitable for structural composite applications because of the discontinuity, the uncontrolled orientation and lack of integration or entanglement of fiber. Type II, which is representative of linear filament yarn system, is acceptable for components subjected to simple tension, but the lack of filament integration or entanglement makes this system vulnerable to splitting and delamination among filament layers, reducing the field of possible applications. The laminar system (Type III), which represents simple fabrics as woven, knitted, braided and non-woven, is more suitable for load bearing panels in flat form. The principle drawbacks of the latter are the weakness in the through-thickness direction, where the presence of resin rich interfaces between the reinforced plies causes delamination, and the through-thickness coefficient of

thermal expansion higher than the in-plane ones is serious problem in applications requiring dimensional stability.

The risk of splitting and delamination is minimized into the IV type, which represents the most reliable system for general load bearing applications. The idea at the basis is to add some secondary fiber reinforcement in the direction perpendicular to the primary, in-plane reinforcement or redirect some of the primary fibers to the secondary reinforcement direction, resulting in an internal structure characterized by continuous fibers oriented and integrated in three directions. Three dimensional fabrics for structural composites can thus be defined as fully integrated continuous fiber assemblies having multi-axial in-plane and out-of-plane fiber orientation.

**Table 1.1** *Classification of textile composite systems*

<i>Type</i>	<i>Textile construction</i>	<i>Fiber length</i>	<i>Fiber orientation</i>	<i>Fiber entanglement</i>
I	chopped fiber	discontinuous	uncontrolled	none
II	filament yarn	continuous	linear	none
III	simple fabric	continuous	planar	planar
IV	advanced fabric	continuous	3D	3D

### 1.3 2D Reinforcement Structure: Woven Fabric

Two dimensional woven fabric are commonly used for composite reinforcement. They consist into the interlacing of two sets of yarns at right angles each other. The yarns that run parallel to the fabric are called warp ( or ends), whereas the yarns that run orthogonal to the fabric are called weft, filling or picks. The manner in which the weft and the warp are interwoven constitutes the weave pattern.

Weaves are usually defined using two numbers,  $n \times m$ . The first number  $n$  represents the number of the weft yarns crossed over while the second indicates the number  $m$  of weft yarns crossed under by the warp yarn. For example a 3X1 weave would run: over over over under over over over under etc.

The schematization of the weaving machine is represented in Figure 1.1. The principles of the weaving process can be summarized into different phases:



- Winding of parallel warp yarns onto a beam;
- following separation of warp yarns according to the chosen weave pattern to form an open channel (shedding);
- insertion of a filling yarn through the channel (picking);
- push of the filling yarn to the fabric edge for uniform yarn packing (beating up).

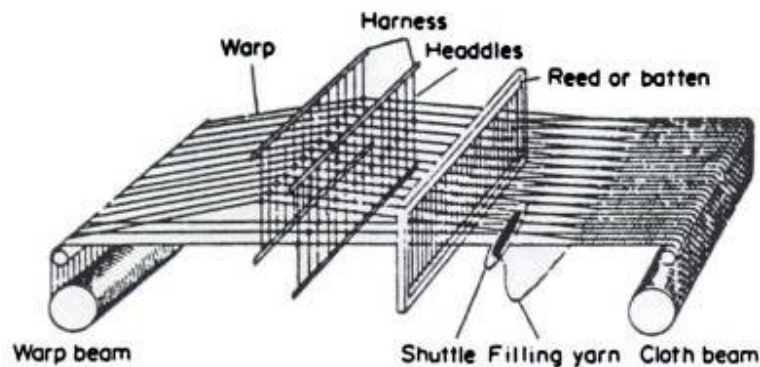


**Figure 1.1** Schematization of a weaving machine

A wide variety of weave patterns is commercially available, however the most of them are derived from three basic types of weave patterns described as follows:

### 1.3.1 Plain weave

The plain weave is the simplest weave known, being characterized by 1x1 weave, resulting in an alternating over and under pattern. This kind of weave provides the maximum stability and firmness with minimum yarn slippage, providing furthermore a good strength in the two yarns directions. When multiple ends and picks are woven following the same scheme of interlacement of plain weave ( $n1 \times n2$ ), the weave is called basket weave:  $n1$  refers to the number of picks an end passes over between interlacements and  $n2$  is the number of picks the same end passes under between the interlacements. For a standard basket weave the number  $n1$  must be equal to  $n2$ . The basket weave contains longer distance between interlacement for a yarn and thus the yarns are less crimped and the fabric is more conformable.

### 1.3.2 *Twill weave*

Twill weaves are so called by the diagonal lines or twills produced on the fabric surface. These lines typically range between  $15^\circ$  and  $75^\circ$ . In a  $n_1 \times n_2$  twill, a warp passes over  $n_1$  wefts and under  $n_2$  wefts in a repeat. It is not required that  $n_1 = n_2$ . If  $n_1 > n_2$  the twill is called warp face twill, if  $n_1 = n_2$  the twill is called balanced twill. Twill direction has to be specified: in a right hand twill the diagonal runs from bottom left to top right of the weave diagram.

### 1.3.3 *Satin weaves*

A satin is a warp-faced weave while a sateen is a weft faced weave. Both are characterized by loose weaves with long minimal interlacement, which results in a shiny appearance. They are described by the number of harnesses existing in a repeat: a  $n$ - harness presents an end lowered for one pick and raised for  $n-1$  picks. Interlacements aren't adjacent. The distance between successive interlacements is defined as counter, and it has to follow some rules:  $c \neq 1$ ;  $c \neq n$ ;  $c \neq (n-1)$  and  $c$  and  $n$  must not share a common factor: for  $n=6$   $c \neq (1,2,3,4,5,6)$  thus is impossible to produce six-harness satin.

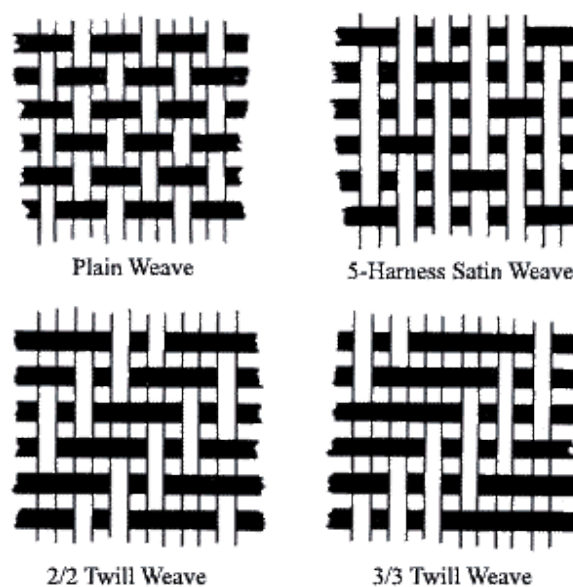


Figure 1.2 Weave patterns

## 1.4 Translaminar-reinforced composites: through-thickness stitched and z-pinned composites

Various types of 3D composite materials have been developed to overcome the shortcomings of 2D laminates, i.e. high fabrication costs, scarce through thickness mechanical properties and impact damage tolerance, as will be discussed more deeply in §1.7.

The 3D fabric composites are present in the actual market in different forms; a basic distinction is between the Translaminar Reinforced Composites and the Unitary 3D Textile (woven, braided and knitted) as reported by Mohamed et al. (2009). In the first case, the already manufactured stack of 2D reinforced plies of prepreg tape or fabric is bound together by a stitching thread or short rigid pins while in the second case the out-of-plane reinforcement (called Z-yarn or binder yarn) is inserted simultaneously with the other reinforcement becoming thus integral part of the preform. The through thickness stitched composites provide a great increase of both modes I and II interlaminar fracture toughness, which results in an increasing resistance to delamination growth and to impact damage. Furthermore, compared to 2D laminates, the stitched composites offer improved handling of preforms, preventing the plies from moving and improved interlaminar fatigue resistance. However the manufacture procedure, which consists into the penetration of a needle pulling sewing threads through already formed prepreg laminate, introduces damages and breakage of the in-plane fibers, altering the initial architecture of the reinforcements and resulting in a reduction in Young's modulus, strength and fatigue resistance of 10-20%. In addition to the damaging effects, the stitching procedure causes the formation of resin-rich through thickness channels around each stitch, which become zones of stress concentrations. This results in the loss of in-plane tensile and compressive stiffness and strength, fatigue life and durability.

The technique of Z-pinning is more recent in comparison with through thickness stitched composites, but shows many similarities in terms of in-plane and out-of-plane properties. The manufacture procedure implies the insertion of the pins through an uncured polymer laminate, typically a low pin content is required for large improvements to their impact damage resistance, and delamination toughness. The insertion of the pins, on the other hand, causes local damage to the microstructure, including out-of-plane crimping, in-plane distortion and fracture of the fibres and resin-rich regions where the fibres have been pushed aside. The flexural strength and fatigue life are lowered, as verified by Chang et al. (2007), as the degrade of the in-plane elastic modulus and ultimate strength under tension and compression have been proved. An additional drawback of these techniques is the request of a

supplementary manufacturing step and therefore equipment, which results in an increase of time and cost.

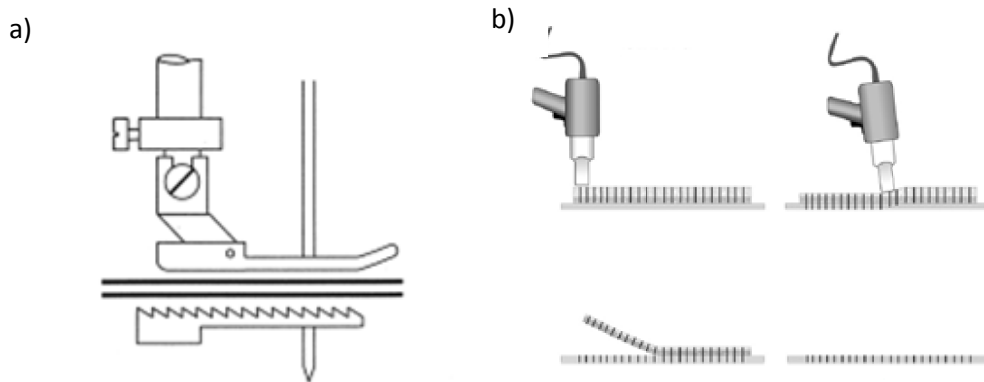


**Figure 1.3** Manufacturing process respectively of a) through thickness stitched and b) z-pinned composites

## 1.5 3D unitary textile preforms

Unitary 3D textile preforms constitute the only actual alternative to stitching and z-pinning prepreg laminates. Different types of 3D architecture can be distinguished, and a prime classification distinguishes between three classes: weaving, knitting and braiding. Each of these methods possesses its advantages and disadvantages, which have to be considered in function of the applications.

### 1.5.1 Weaves

Woven fabrics are formed interlacing more sets of yarn, the longitudinal are known as the warp while the widthwise yarns are known as the filling or the weft. The individual yarns in the warp are called an end instead the individual yarns in the filling direction are called a pick. The possible configurations are multiple, depending on the number of layers interlaced, the pattern of repeat and the presence of in-laid yarns. Figure 1.4 represents the transverse sections along the warp direction of the three preforms available at the present. 3D interlock weaving re-directs part of the warp-yarns to serve as out-of-plane reinforcement, reducing in-plane fiber volume fraction and creating crimp and waviness in the primary reinforcement. The layers can be bound together by interlacing warp ends in the structure with the filling of

adjacent layer (angle interlock 3D weaving), or by interlacing the face and back filling layers (warp interlock 3D weaving). If the Z yarns interlace with back layers in a vertical configuration, instead, the structure is called orthogonal weave. One of the main feature that characterizes the 3D orthogonal woven non.crimp fabrics, is the absence of crimp in all inner warp and fill yarn layers, only a minimum undulation is observed in the surface fill yarn layers for the interaction with the through thickness yarns. It has to be noted that the presence of Z-fibers reduces the in-plane fiber volume fraction and respective composite properties.

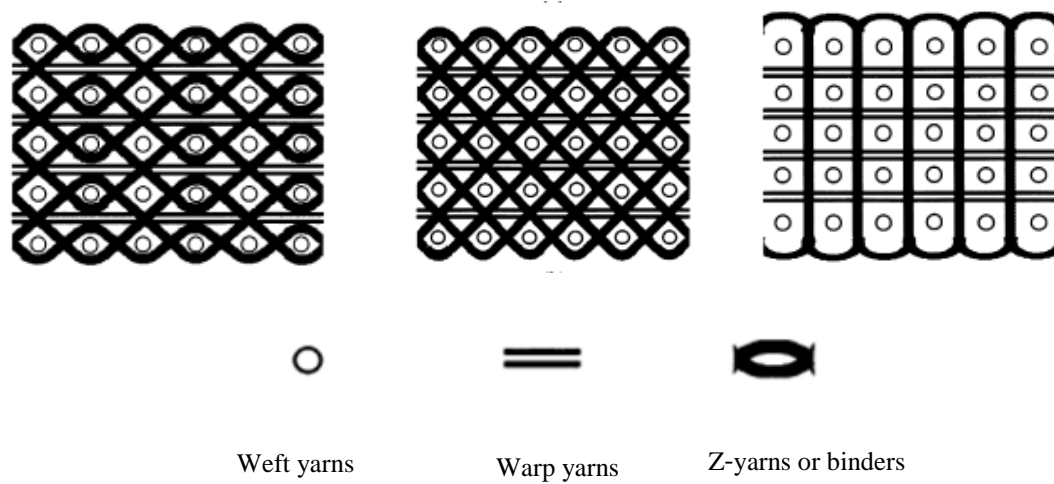


**Figure 1.4** Layer-to-layer angle interlock, through the thickness angle-interlock, orthogonal interlock.

### 1.5.2 Knits

The term knits refers to textile fabrics produced by intermeshing loops of yarns using knitting needles. The knitted preforms are characterized by a high degree of nesting (or mechanical interlocking) between individual layers of knitted fabric, resulting in a high Mode I fracture toughness, added to an excellent impact performance, which make them ideal for service conditions where energy absorption or damage tolerance is critical. As regards the in-plane mechanical properties, they lie between random mats and traditional 2D weaves, as it can be expected considering that the plain knit has very few straight sections of yarn, and none of significant length. However these properties can be radically changed by the knit architecture and the degree of stretch within the knit. There is a particular sub-group of knitted fabrics, non-crimp fabrics, capable of manufacturing parts with high in-plane mechanical performance at a reduced manufacturing cost. They consist in multiple layers of

straight yarns linked together by z-binders inserted using a warp knitting machine. Each layer is separated from the other ones, and they are not interlaced, in order to avoid crimp. In this fashion, they permit to combine aspects of weaving and knitting.

Moreover, from the manufacturing point of view, the use of 3D knitted composites permits the production of complex, net-shape preforms, although knitted preforms aren't capable of being produced with similar thickness dimensions to 3D woven or braided preforms. As it can be seen in Figure 1.5, 3D knitted composites are characterized by a noticeable curved nature of the yarn architecture, which results in a minor structural strength (compared to woven or braided fabrics) but also in a conformability suitable for non structural components of complex shapes.

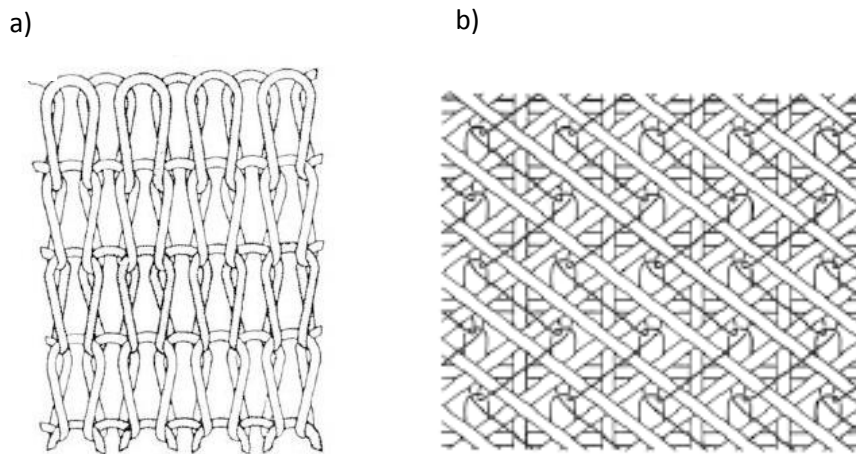


**Figure 1.5** Illustration of 3D nature of a) typical knitted fabric and b) multiaxial warp knit fabric (non crimp)

### 1.5.3 Braids

3D braided fabric are constructed by intertwining or orthogonal interlacing two or more yarn system to form an integral structure. There are two basic traditional braiding methods for producing the preforms: two-step, four-step, while more recent methods are 3D rotary braiding and multi-step braiding, which permits to make multidirectional 3D braided preforms. In the former one the braider yarns move among the axial yarns, which remain stationary. Its name is due to the process of manufacture: in the first step the braiders all move in one diagonal line but in alternating directions, in the second they move along the other diagonal line. In the four-step braiding process, instead, more passages are needed for

completing one machine cycle, as represented in Figure 1.6: in step 1 and 2 all the rows and columns move in alternating directions, then these carrier movements are reversed in steps 3 and 4. Whatever is the method of braiding used, the pattern is characterized by the angular orientation of the braider yarn,  $\theta_b$ , and the pitch length,  $h$ . The advantages of the use of this kind of fiber architecture include: the value of the angle formed by braiding yarns to axial direction minor than  $90^\circ$ , the possibility of the incorporation of axial yarns (aligned at  $0^\circ$ ), a wide obtainable range of thicknesses and a variety of shapes of which the unitary preforms can be produced.



**Figure 1.6** Model of a 3D braiding composite: the colour yellow indicates braiding yarns while blue indicates axial yarns (aligned at  $0^\circ$  degree to length direction)

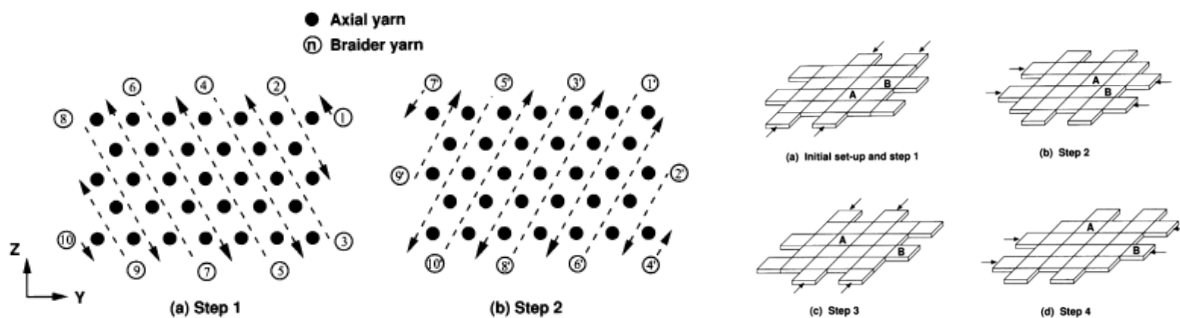


**Figure 1.7** 2-step and 4 step braiding process

The main advantage of 3D braided fabrics is the complete absence of delamination due to intertwine-type out-of-plane interlacement. On the converse side, however, they have low

transverse properties due to no yarns being equivalent to filling yarns in 3D woven fabric and there are size and thickness limitations. The in-plane properties can be improved with the insertion of  $\pm$ bias layers using the multi-axis 3D braided fabrics, which have multiple layers and no delamination, however this technique is at an early stage of development and needs to be fully automated, as observed by Bilisik, K. (2013).

## 1.6 History and applications of 3D composites

The appearance of 3D composites is not recent; during the late 1960's, in fact, they found their first applications in the emerging aerospace industry, which needed parts capable of withstanding multidirectional mechanical and thermal stresses. The first attempt was to replace expensive high temperature metal alloys in aircraft brakes, while, during the mid 1980's, the aims were to overcome the problems of production and maintenance encountered with the use of traditional 2D laminates. For the aircraft manufactures, in fact, the production of complex components from laminates was expensive, while the suffering to impact damage of laminates from dropped tools was a problem for aircraft maintenance engineers.

However not only the aircraft industry, but also the building industry has been interested into the development of 3D composites. An example of application of 3D composite is the use of I-beams for the roof of a ski chair-lift building in Germany, replacing the use of heavy steel beams, which were difficult to bring to the building site because of the steep terrain.

Despite the advantages and potential benefits, however, these materials have failed to find many commercial applications, due mainly to the lack of an extensive database of material properties, particularly regarding the fatigue effects. This makes difficult to determine the optimum weave architecture and yarn material required to provide the desired in-plane and through thickness properties for a specific structural design.

The future possible applications in the next years for this material could interest industries as maritime, civil infrastructure and land transportation, e.g. floors, floor beams in trains and fast ferries and flat load trays in trucks. One of the case studies reported from 3Tex, Inc. (1) regards the comparison of the costs of the construction of the baseline boat hulls made with 2D materials vs the costs of the same hulls made with 3WEAVE and highlighted the saving of 35\$ over a total expense of 470\$ of the former ones. Another case study investigates the cost of manufacturing of high performance powerboats. After switch to infusion methods using

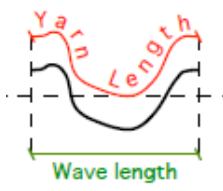


3WEAVE®, it has been proved that productivity increased by 50% and boat weights dropped 20%, while strength and stiffness increased at least 50%.

Other potential applications could be crash member in cars, buses and trucks, thanks to the improved impact energy absorption capacity of 3D woven composites. Their use could be involve also the production of shipping containers and other container transport applications, where the reduction in the weight of the container would allow heavier payloads to be carried. Another case study regards the fabrication of industrial pressure tanks made from textile composites: the replacement of 2D fabric with fewer layers of 3WEAVE fabric comported the reduction of labor by 50% and cycle time by 30%.

## 1.7 2D versus 3D composites

As already observed, the introduction of 3D composites is due to the effort to overcome the drawbacks given by 2D composites. One of the principal causes of failure of 2D laminated composite materials, in fact, is delamination, due principally to the formation of resin rich regions between the adjacent fiber layers that most of the composite structures made of more than one ply of unitary material with plies separated by weaker interfaces present. The effects of the presence of delaminations are the reduction of durability and fatigue life: its propagation can cause external and internal buckling, ply splitting at the free edges, open holes and other high stress concentration regions. The incorporation of through thickness reinforcement into the structure of three dimensional fabric preforms, instead, permit to virtually eliminate the problem, increasing also the impact damage resistance and post impact mechanical properties. The z-reinforcements, in fact, act as bridges across the delamination crack, obstacoling the spread of impact damage and minimising the loss of post-impact properties. Researches conducted 3TEX® have proved that the critical strain energy release rate increases of up to 20% with 2-3% through thickness fiber content by weight. The reduction of yarn undulation, or crimp, plays furthermore an important role on the advantages of 3D orthogonal composites compared to the 2D composites. A crimp is defined as follows:

$$\text{crimps} = \frac{\text{yarn lengths}}{\text{wave lengths}} \quad (2.1)$$


The stiffness is increased with reducing crimp and it is believed that the explanation could be the presence of a minor number of crimped strands which tend to straighten out instead of stretch when loaded in tension. Crimps also affects the strength of a composite material: if all strands in a fibre reinforced composite are straight they react at an external load simultaneously and the full strength is achieved. However if they are bent with different angles, diverse strands would carry diverse portion of loading and the ones which would bear higher load will fail earlier.

The presence of z- yarns, however, causes the degradation of the in-plane mechanical properties of composites. The in-plane stiffness and strength properties are affected by microstructural damage to the composite, which includes crimping, waviness and damage to the fibres, formation of polymer-rich zones and, in some cases, swelling, which reduces the average fibre volume content.

Nevertheless, the considerations made so far are general not considering the difference between the diverse methods of manufacturing 3D woven fabrics, which, for the most part, use an adapted version of the 2D weaving machines with cam, dobby or Jacquard shedding mechanisms. Using 3D different machines and process results in different fiber architecture of 3D woven preforms and therefore in different properties. The drawbacks of the solutions which use conventional 2D weaving machines are a high level of interlacing, which leads to a high degree of fiber crimp and waviness and a high amount of the fiber damage, caused by the moving machine parts. When the warp ends have to be drawn through the heddles on the harness frames of the shedding mechanism, they are subjected to a substantial degree of abrasion, which determines the reduction between 30% and 50% of pristine yarn strength. Dissimilarly, the 3D weaving process and machines used in manufacturing 3WEAVE® fabric impart less damage on warp yarns, which are not required to be drawn through the heddles of the shedding mechanism and remain stationary during weaving, while the Z-yarns are subjected to damage, being the only yarns moving during the weaving process. Different studies have concluded that while the 3D interlock weave composite is much inferior for

tension, compression, interlaminar strength and compression after impact vs 2D weave laminate while the 3D non crimp weave composite is competitive, showing considerably higher tensile modulus, tensile and compressive strengths in warp direction than the 2D weave laminate. It is clear that without making a distinction between the types of 3D woven preforms, it makes little sense talking about mechanical properties of 3D woven composites.

### 1.7.1 Studies of comparison between 3D and 2D composites

Lomov et al. (2009) have compared in their study in-plane mechanical properties of two single ply non-crimp 3D orthogonal weave composites, labelled 3D-96 and 3D-78, with the ones of a 4-ply plain weave composite laminate, labelled 2D-24, represented in Figure 1.8.

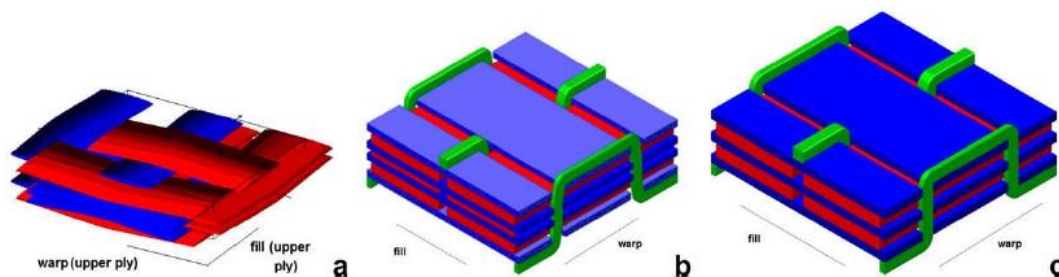


Fig. 1. Reinforcement structure of 2D-24 (a), 3D-96 (b), and 3D-78 (c) composites.

**Figure 1.8** Reinforcement structure of a) 2D-24 b) 3D-96 and c) 3D-78

The study resulted into the comparison of the mean values of Young's moduli, in-plane Poisson's ratio and stress-strain curves showed by the three materials. The results, reported in Table 1.2, can be summarised as follows:

- Young's moduli values for the three composites were very similar, even if the mean value was slightly higher for 2D-24 composite;
- 2D-24 composite presented the larger in-plane Poisson's ratio both along the warp and weft directions;
- ultimate stress values registered for the three composites were analogous, with higher values for 3D-96 composite, especially when tested along the weft direction;
- ultimate strains values were generally higher for both 3D composites compared to the 2D-24, with higher values for weft than for warp directions.

**Table 1.2 Properties resulted from the tests for the three material 3D-96, 3D-78 and 2D-24 tested into the two principal directions warp and weft**

	Vf%	Direction	E [GPa]	$\nu$	$\sigma_{ult}$ [MPa]	$\epsilon_{ult}$ [%]
<b>3D-96</b>	48.9	Warp	24.3±1.2	0.143±0.159	429±34	2.74±0.29
		Weft	25.1±2.3	0.128±0.081	486±5	3.33±0.27
<b>3D-78</b>	47.5	Warp	23.0±2.5	0.115±0.031	423±29	2.96±0.51
		Weft	23.0±2.5	0.149±0.057	427±8	3.14±0.44
<b>2D-4</b>	52.4	Warp / weft	26.0±1.5	0.207±0.091	413±4	2.38±0.02

As it can be seen, the largest difference in ultimate stress is observed between 3D-96 and 2D-24 composites under fill directional loading (17.6 %) while in the warp-directional loading the difference lowers to 3.9%. The differences existing between the ultimate stresses for 3D-78 as 2D-24 are smaller, respectively 2.4% in warp and 3.4% in fill directions. Both 3D weave composites have higher ultimate stress and strains values, lower in warp than in in fill direction. The reasons of the difference between 2D and 3D woven composite are essentially two:

1. the presence of crimp in 2D woven composite brings to a tendency of out-of-plane deformation when they are loaded in tension both in warp or weft directions. Due to a constraint from adjacent layers, this results in additional shear stresses in the planes xz and yz (z=normal to sample and loading direction), in matrix and in yarns, which adds to the transverse normal stresses and facilitates the multi-axial stress state to reach the damage initiation envelope;
2. the different amount of damage introduced during preform manufacturing, which penalizes the 2D composite reducing their initial strength.

Another study was conducted by Carvelli et al. (2010). They confronted the tension-tension fatigue behavior of a single-ply 3D orthogonal weave composite with a multi-layer 2D plain weave E-glass reinforced composites, assumed equivalent each other since they were characterized by a nearly equal total thickness, a similar fiber volume fraction and they were fabricated with the same method using unchanged constituents. At first, they compared the mechanical properties of the two materials; the outcomes are summarised in the Table 1.3.

**Table 1.3** *Properties of 3D and PW composite*

	<b>E(GPa)</b>	<b><math>\sigma_{ult}</math>(MPa)</b>	<b><math>\epsilon_{ult}</math>(%)</b>
<b>3D-fill</b>	26.34±0.63	540±20	2.92±0.05
<b>3D-warp</b>	26.39±0.76	441±26	2.41±0.13
<b>PW</b>	24.68±1.51	427±23	2.45±0.18

As it can be observed from Table 1.3, the absence of crimps permits to the 3D woven composite to reach higher values of in-plane Young's moduli both in warp and weft directions. For what concerns the ultimate stress, the higher average values reached are of 3D woven composite, with a substantial difference between the in-plane directions tested: the material tested in the weft directions showed an average ultimate stress 22% higher and an average ultimate strain 21% higher than the respective values of the same material tested along the warp direction. Making a comparison with the counterpart 2D composites, the 3D exhibited furthermore higher in-plane strength and failure strain in the fill direction, while in the warp direction the difference of the values was less evident, taking into account the scatter of the data.

After having studied the mechanical properties, the study investigated the differences of fatigue life of 3D composite and 2S composite. S-N curves obtained for the different materials are represented in Figure 1.9, while Table 1.4 shows the number of cycles to failure recorded for different stress levels.

**Table 1.4** *Average number of cycles to failure at different stress levels for 3D orthogonal woven composites tested in fill and warp direction and for 2D plane weave composite*

<b>Stress Level [MPa]</b>	<b>Number of cycles to failure</b>		
	<b>3D Fill</b>	<b>3D-Warp</b>	<b>PW</b>
60	5 000 000	2 393 181	5 000 000
70	2 263 028	666 110	1 731 774
80	771 452	153 056	433 181
95	192 313	55 018	105 785
150	13 595	9083	9883
200	3372	2506	2723
300	344	256	299
350	118	84	78

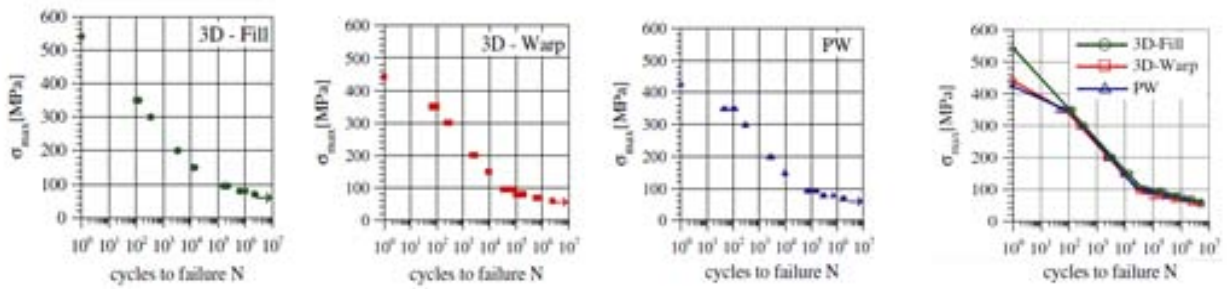


**Figure 1.9** Maximum stress vs number of cycles to failure for a) 3D composite loaded in fill and b) warp direction and for 2D c)PW laminate

The differences observed between the fatigue behavior shown by the two materials, depended principally on the level of stress imposed.

The 3D composite fatigued in warp direction exhibited lower fatigue performance for lower stress levels in comparison to the plain weave counterpart, while for intermediate stress levels, both 3D composites tested in warp and weft direction showed comparable performance to the plain weave ones. When subjected to high stress levels, instead, 3D composite showed longer fatigue lifetimes in the weft direction.

The main reasons of the difference existing between warp and weft directions can be resumed as follows:

1. More fibre damage imparted to the warp yarns than to the fill ones during weaving;
2. Local pockets of pure matrix created by the presence of Z yarns, which increased local stress concentration and reduced resistance to initial damage formation;
3. Cyclic frictional contact between warp and z-yarns due to the Poisson effect during the application of tensile stress. Their mutual friction effect may reduce overall fatigue life of the sample.

The study dealt also the development of damage. Comparing 3D and 2D composites tested at an equal number of cycles, they observed that 3D were less prone to transverse and longitudinal cracking. The inherent crimp of the plain weave fabric and irregularities of the fabric ply nesting, in fact, were thought to cause stress concentrations, facilitating the damage development. and determining general worse fatigue performance.

## 1.8 Comparison between elastic modulus and fatigue performance of 3D woven, stitched and pinned composite

A study conducted Mouritz et al. (2008) regarded the comparison between the three different categories of 3D reinforcement actually commercially available, i.e. 3D woven, stitched and pinned composites. In particular, the research dealt with the effect of the type of reinforcement exerted onto fatigue life. The influence of the type and volume content of the z-reinforcement on the tensile modulus was thus reported, together with the influence exerted onto strength and fatigue properties for each class, taking into considerations only composites made of fiberglass/vinyl ester. The 3D woven presented 13 ply layers: six of warp yarns and seven of weft yarns. According to the results reported, the tensile modulus did not show any relationship with the amount of z-reinforcement. This was an innovative outcome, since previous studies had reported a loss in modulus caused by increased fibre waviness forced to bend around the z-reinforcement.

In Figure 1.10, the values of modulus are shown, represented normalized to the values of their control composite material without z-reinforcement. In the graph reported always in Figure 1.10 on the right hand the values of the strength normalized to the value of their control material considered without z-reinforcement are reported. In the case of the strength, the decrease for the z-pinned composite is evident, registering a rate of approximately 7.5% for every 1% of z-pins. The reason of the reduction was attributed to the microstructural damage caused during the manufacturing process: when z-pin were inserted into the composite, in fact, fibres were crimped, distorted and broken, as already mentioned in §2.4. In the case of 3D woven composites, despite the scatter of the data, it can be affirmed that the average strength values are slightly higher and lower than their control material. The volume content in these materials was relatively low (<1%) and this may account for the constant strength values. In these cases, unlike the previous one, the z-reinforcements were inserted into dry fabric, minimizing the amount of damage and breakage and therefore their tensile strengths did not decrease rapidly with increasing z-reinforcement content.

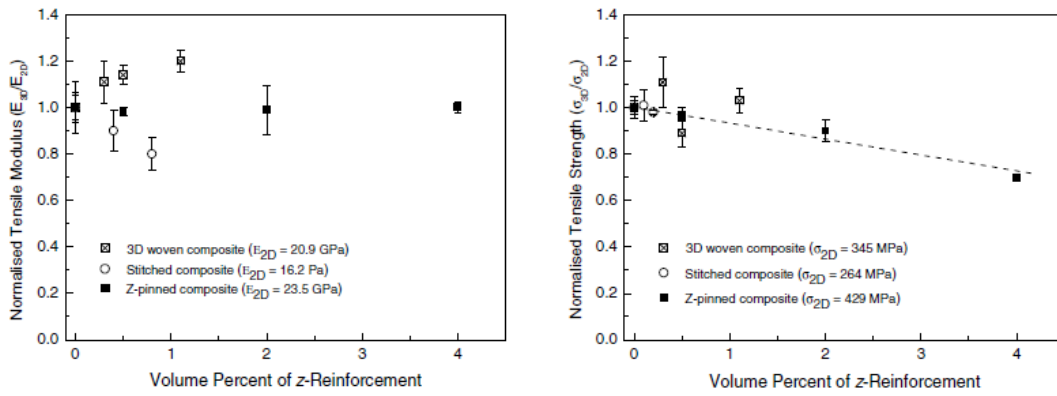


**Figure 1.10** Plot of volume content of z-reinforcement vs normalised tensile modulus and normalised tensile strength for the 3D woven, stitched and z-pinned composite.

Mouritz et al. also analyzed the effect of the amount of z-reinforcement on the fatigue life, subjecting the specimens of the three composite to tension-tension loading over a range of peak stress levels from 2% to 90% of the ultimate tension strength with a  $R=0.6$ . The result was a lowering of the S-N curve compared to the control material's one, with a large loss in fatigue performance caused by a relatively small amount of through-thickness reinforcement, more accentuated as the volume content of z-reinforcement increased. For example, as it can be seen from Figure 1.11, the fatigue life was reduced by one order of magnitude at content of z-reinforcement of about 1% for 3D woven, of 0.8% for stitched and of 2-4% for z-pinned composite. The large reduction to the fatigue performance was attributed to the changes to the composite microstructure caused by z-binders, which promoted the early formation of fatigue-induced damage.

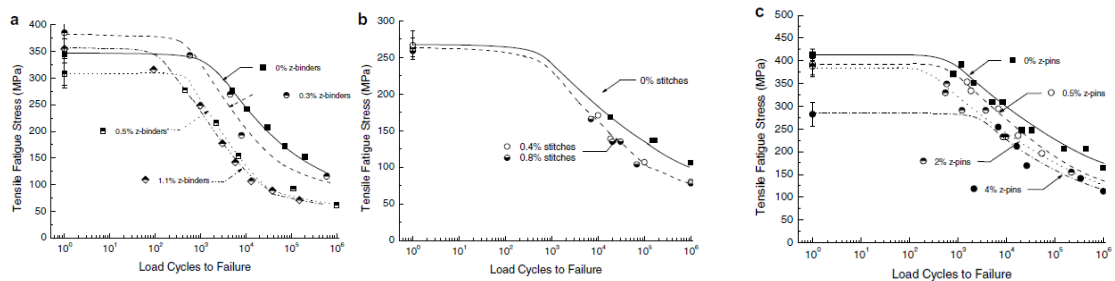


**Figure 1.11** S-N curves for a) 3D woven b) stitched c) z-pinned composites



Damage development will be examined in more details for 3D-96 woven composites in §2.9, material that will be the object of this study. However, before describing it, the microstructure of the 3D-96 composite will be presented in §2.8 in a detailed fashion, including the description of the nature of different pre-existing defects, since their presence can be correlated with the variability of the mechanical properties and the development of the damage.

### 1.9 Microstructure of 3D woven composite specimen

As illustrated in Figure 1.12, the 3D-96 preform consisted of three yarn systems: in-plane warp and weft, orthogonal to each other and through thickness (z) yarns, binding the fabric together. Notwithstanding the non-crimp 3D orthogonal weaving process and machines used by 3TEX Inc. guaranteed high consistency and low waviness of the in-plane fibers, still defects could be detected at microscope analysis.

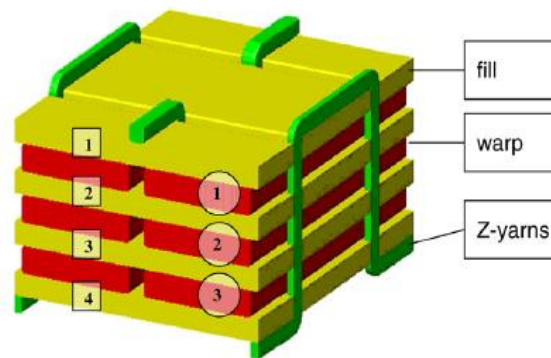


**Figure 1.12** Unit cell model of the non crimp woven fabric, where fill and warp yarns numbered.

The principals defects detected into the micro-structure could be summarized as follows:

*Z-binder waviness*: the load applied to the z-binders to ensure they are taut enough when woven into the fabric obliges the z-binder to follow a sinusoidal-shaped rather than a straight profile with angles of 90°;

*Microcracking and breakage of z-binders:* z-binders suffered of fibre damage when woven into the fabric, which caused a small reduction to the Young's modulus (5%) but a large drop to the tensile stress (50%). The formation of micro-cracks in the glass fibres were due to the bending in a very tight radius and to the abrasion which occurred as they rubbed and slid against the loom machinery during weaving.

*Fibre crimp:* relatively small undulations of the fill yarns of the surface fabric layers could be observed in the vicinity of their overlays with so called z-crowns, which is the name with which regions where z-binders cross underlying weft tows are indicated. In fact, when the z-yarns passed over the weft yarns at the surfaces, pressing them over the warp yarns, a local indentation of Z-crown into the underlying surface fill yarns formed. Crimping could not be avoided, as a tension must be applied to the z- binders to be sure that they are taut enough into the fabric.

*Polymer-rich regions:* polymer rich-regions formed in the warp direction along each row of the z-binders. The warp yarns were pushed sideways during the weaving to make space for the z-binders, and this formed gaps between neighboring yarns, which were then filled with the matrix during the infusion.

*Voids:* voids were observed in the polymer rich regions, most of all located in the polymer matrix near z-binders. Porosity was caused by the anisotropic permeability of the 3D woven fabric.

## **1.10 Development of damage in 3D woven composite**

In a recent paper, Mouritz (2008) attempted to describe the phases that characterized damage development into 3D orthogonal woven composite material in the case of tensile fatigue loading. The damage started from the debonding of the z-reinforcement, due to the generation of shear stress along the interface with the surrounding material. The applied fatigue stresses caused plastic shear flow of the polymer matrix near the z- binders. The plastic shear deformation caused, in turn, the crack growth between the z-binders and the surrounding material. The presence of voids was believed to facilitate the propagation of cracks. Cracks initiated and spread along the interface, changing the stress transfer mechanism in the composite material since higher loads were exerted onto the undamaged regions. The number

of debonding cracks increased with the amount of z-reinforcements, explaining the correspondant reduction of fatigue life, already presented in §2.8.

Matrix cracks were also observed forming in the polymer-rich channels between the warp fibre yarns. These cracks developed normally along the load direction and extended across the width of the channels. Transverse matrix cracking caused a small degree of softening under cyclic tensile loading and therefore might contribute to the loss in fatigue performance.

The fatigue damage observed by Mouritz included longitudinal splitting and delamination cracks too.

A recent work conducted by Baiocchi et al. (2013) has investigated the damage development within the later stages of the fatigue life of a specimen of 3D-78 orthogonal woven composite. Stiffness reduction and energy dissipation per cycle, represented by the stress/strain hysteresis loops during fatigue tests, have been measured and recognized as valid parameters for following the damage evolution within the material. By monitoring their trend, three stages could be distinguished. In particular, damage characterizing the third stage was investigated, focusing the interest in the individuation of tow fractures, supposed to lead the specimen fatigue tested to final failure, forming in specific locations within the fibre architecture, identified thanks to the combination of X-ray micro computed tomography and optical microscopy. As it can be observed in Figure 1.13 and in Figure 1.14 taken from this work, fibre fractures developed in the warp tow closest to the z-tow, as the possible consequence of stress concentration due to matrix cracks extended fully across the composite between the surface weft tows and into the resin pockets between the warp tows.

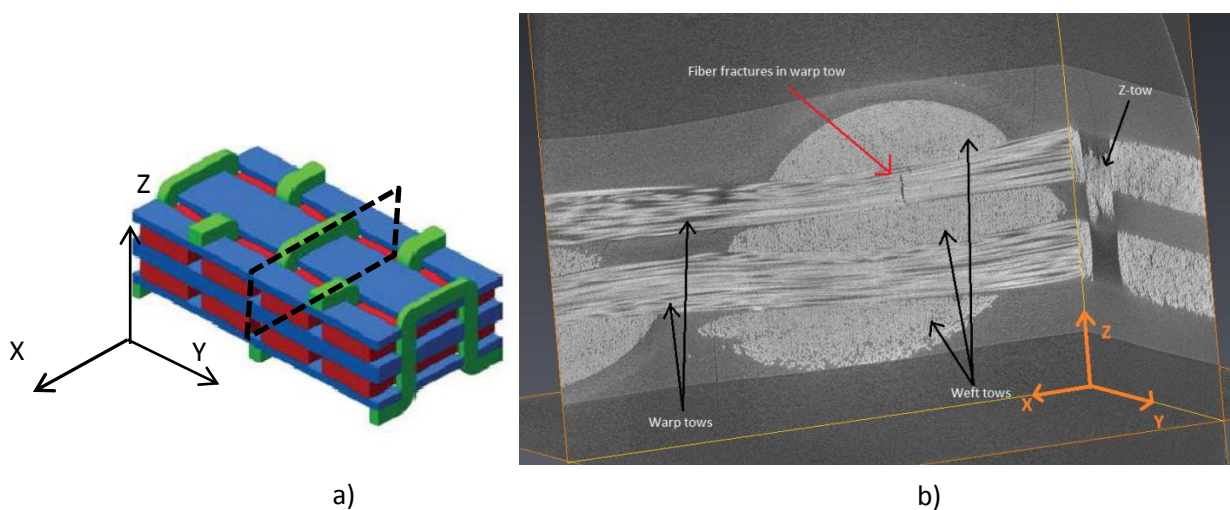


**Figure 1.13** a) Schematic of the 3D-78 architecture and b) CT section showing extensive fiber fracture towards the edge of a warp tow. Courtesy of Baiocchi (2013).

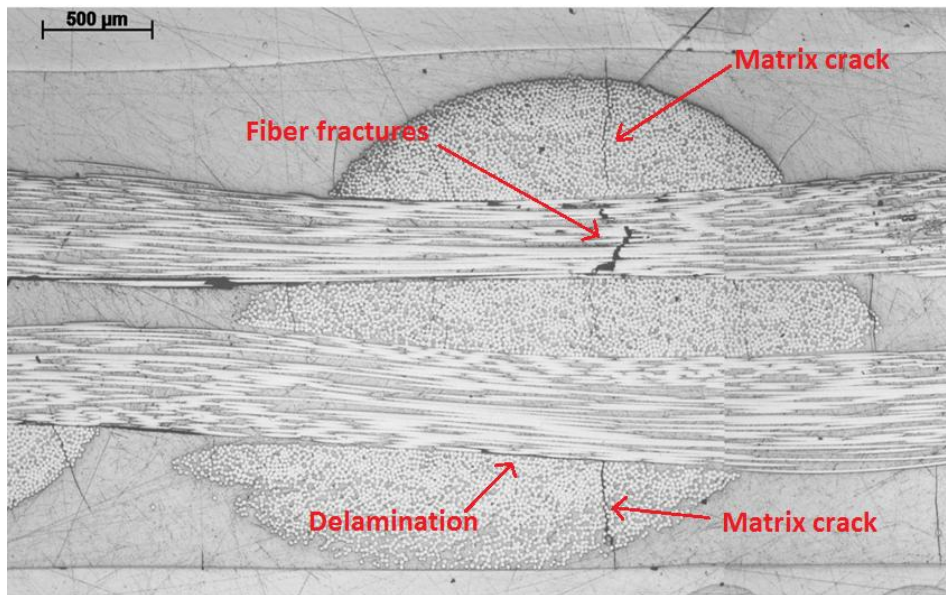


**Figure 1.14** Optical micrograph showing the same tow fracture as seen in Figure 1.13. Courtesy of Baiocchi (2013).

Experimental observations of damage development could be completed attempting to reproduce stress distribution into the material structure.

With the aim of better understanding the micromechanical events occurring inside the material, a finite element model of the 3D-78 composite was developed by Topal (2014). She modelled a representative volume element (REV) of the fabric preform, i.e. the smallest repeating entity of the structure, for then subjecting it to loading oriented along weft and warp directions.

The resulting stress distribution for the warp case, represented in Figure 1.15, showed that stresses in the fill yarns, even if the values of x-stresses were lower than for warp yarns, they exceeded the transverse strength of the material, such that consequently, matrix cracking was to be expected within the fill yarns

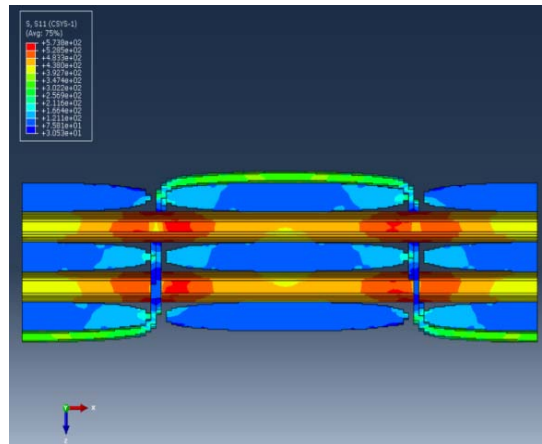


**Figure 1.15** Stress distribution in the fabric material in x direction. Courtesy of Topal (2014)

When the REV was subjected to weft loading, instead, the stress distributions in x direction revealed compressive x–stresses into the warp yarns, due to Poisson’s contraction, while all fill yarns were under tension in y direction

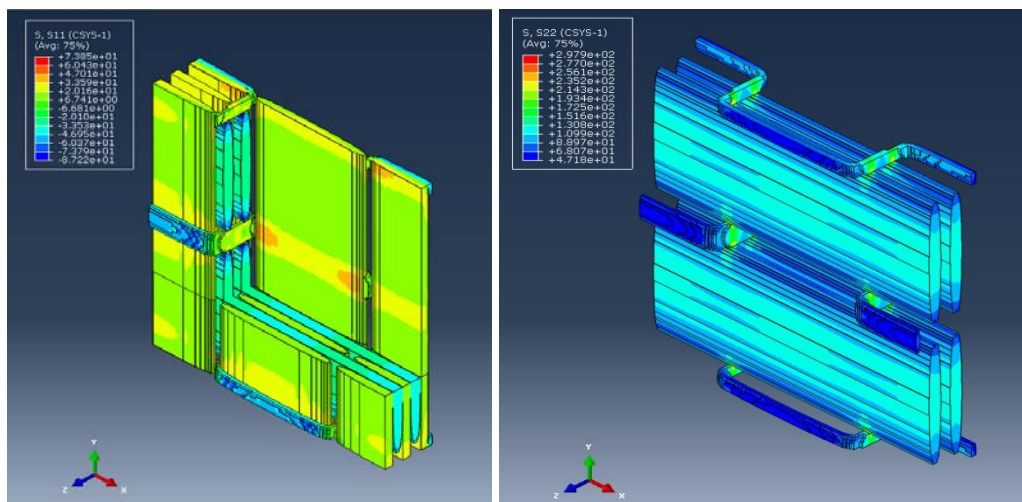


**Figure 1.16** Stress distribution in the fabric material in y direction. Courtesy of Topal (2014)

## 1.11 Thermographic observations on damage evolution

When a repetitive load is applied, the portion of mechanical energy represented by the area enclosed by hysteresis cycles is transferred into the material. This can be either dissipated in the form of heat, resulting into an increase of temperature, (thermal energy), or can change the internal energy of the material. Hysteresis energy per cycle can therefore be represented as the

sum of the volumetric dissipated energy, energy associated with thermal capacity and damage energy. The thermal capacity energy is the amount of energy that is responsible for the increase of the temperature of the specimen, while the damage energy is responsible for the formation of cracks. A first approach to characterize energy dissipation is given by Naderi and Khonsari (2012), who studied the fatigue degradation of a glass/epoxy unbalanced woven fabric composites with plain weave. They developed a theoretical model based on the energy balance, using the second law of thermodynamics for the formulation of dissipative processes associated. They showed that degradation was characterized by three stages:

1. initial increase related to matrix cracking;
2. slow and steady increase with debonding and additional matrix cracking;
3. soaring increase connected to fibre breakage.

A further study involving the role of temperature evolution on tension-tension fatigue life-time was conducted by Zangenberg (2013). He considered thermography in order to quantify the differences in fatigue life-time for various test geometries, proving that life-time scatter in composites fatigue tests is correlated to different heat developments observed during fatigue experiments. Moreover, another noticeable outcome was constituted by the fact that the temperature profile evolution could be represented as a function of stiffness reduction.

# Chapter 2

## Materials and experimental methods

### 2.1 Introduction

The present section illustrates the experimental techniques involved in this project. After a brief description of the material, the manufacturing process of the laminate is explained in detail, followed by the fiber volume fraction measurement and the cutting and preparation of the tests-specimens. The second part of the chapter is dedicated to the description of the setting-up for quasi-static and fatigue tests as well as the methods of studying the damage development, i.e. optical and scanning electron microscopy, X-ray micro computed tomography and thermography. For the latter two techniques, it has been considered appropriate to delineate initially the basic principles of operation.

### 2.2 Materials and experimental methods

The material investigated was a single ply 3D woven composite embedded in a tri-component epoxy matrix. The no-crimp 3D orthogonal E-glass fabric preform, commercialized under trademark 3WEAVE® by 3TEX Inc. with the label of 3D-96, was characterized by an areal density of  $3255\text{g/m}^2$  (equivalent to  $96,6\text{ oz/yd}^2$ , from which derives its commercial name), and a thickness of 2.54 mm, as declared by the product data of the company.

The fiber architecture was constituted by three warp layers and four weft layers interlaced by through – thickness z-tows. All the tows are made of PPG Hybon 2022 E-glass fiber rovings silane seized, compatible with polyester, vinyl ester, epoxy and phenolic resin systems. This type of roving is designed to produce good wet-out and wet-out consistency, good abrasion resistance and processing characteristics.

The amount of fiber is distributed between warp, weft and the through thickness reinforcements, respectively with the percentages by weight of 47.6%, 48.5% and 3.9%. The principal properties of the preform are summarized in Table 2.1, where the linear mass density of fibers is expressed in tex unit, defined as the mass in grams per 1 km.

**Table 2.1** Properties of the 3D-96 non-crimp woven preform

Fabric plies		1
Areal density		3255g/m <sup>2</sup>
<b>Warp</b>	Insertion density	2.76 ends/cm
	Top and bottom layer yarns	2275 tex
	Middle layer yarns	1100 tex
<b>Weft</b>	Insertion density	2.64 picks/cm
	Yarns	1470 tex
<b>Z-yarns</b>	Insertion density	2.76 ends/cm
	Yarns	1800 tex

The method adopted for manufacturing of the material was an in-house wet impregnation technique, which produced a good transparency of the material, so as to permit the monitoring of the damage development of the material during the phases of testing.

The manufacturing procedure divides into different steps. The first consisted of the decrystallization of the resin Shell Epikote 828 (Bisphenol-A). Although within the appropriate shelf life, the storage length of the resin resulted in a level of crystallinity which did not permit a proper mixing of the resin with the curing agent and the accelerator. 190 grams of resin were therefore weighed and put into an oven at a temperature of 60°C for 1 hour to restore the required low viscosity of the resin. After that, the preparation of the compound was carried out: expressed in terms of weight, 100 parts of epoxy resin Shell Epikote 828 (Bisphenol-A) were mixed with 60 parts of Shell epicure nadic methyl (MNA) curing agent and 4 parts of accelerator Ancamine K61B. Table 2.2 reports the exact amounts of grams used for each constituent, which allowed a suitable wet-out of the fabric.



**Table 2.2** Weight expressed in grams of epoxy resin, curing agent and accelerator

	<b>Epoxy resin</b>	<b>Curing agent</b>	<b>Accelerator</b>
	<b>Shell Epikote 828</b>	<b>MNA</b>	<b>Ancamine K61B</b>
<b>Weight [grams]</b>	190	114	7.6

The mixture was then slowly stirred for 10 minutes within a fume cupboard, to avoid the inhalation of unsafe fumes. It was recommended that the process of mixing was conducted slowly for limiting the incorporation of air bubbles. When the compound was at a visual inspection, sufficiently homogeneous, the compound was degassed a first time. The resin was therefore put into a vacuum oven at a temperature of 60°C and a pressure of -1 bar for a time variable between 10 and 15 minutes. Then, for ensuring the complete homogeneity of the compound, resin was removed from the oven and mixed, always slowly, for another 15 minutes. Once the mixture appeared thoroughly mixed, it was put again into the vacuum oven for the second part of degassing. Values of temperature and pressure were kept unaltered. It was important to continue controlling periodically the resin during this phase, to be sure that the resin did not overflow for the raising of the bubble towards the surface. If this were to happen, the overflow could be suppressed, by turning off the vacuum pump and allowing the entrance of the air in the oven. When the level of height of the resin lowered sufficiently, the vacuum was re-established. These procedures were repeated, if necessary.

The subsequent steps regard the preparation of the fabric. After having cut it in a square shape of 300x300 mm, the structure which would sustain the fabric was prepared. First of all, a sealant vacuum tape had to be applied all around a wood frame, used to prevent the overabundant resin spillage during the following wetting and the curing processes, then a silicon coated release film was attached to the frame.

The fabric was at this point positioned on the film, and the next step consisted of the preparation of the vacuum chamber. For improving the wetting of resin into fabric, on the bottom of the chamber was positioned a steel plate, previously heated at a temperature of 120°C, upon which a glass plate was stacked, covered with a layer of wax to avoid the adhesion of the plastic film to the bottom of the frame. After that, the frame itself was positioned over the glass plate, and the resin could be poured over the fabric, taking care to pursue an homogeneous distribution. The material was thus ready to be vacuumed at -1bar for 1 hour at least, to permit the resin to wet properly the fabric. Once the wetting process was

finished, the frame was extracted from the vacuum chamber, and another silicon release film was put onto the surface of the cloth. The extra resin was then pushed out of the laminate and the air inclusions were eliminated with the use of a flat piece of plastic. The laminate was thus ready for the final step, i.e. the curing cycle. The frame was placed in an oven where was present a specially designed rig, in which was applied a pressure of 7.80 KPa through the use of 4 weights of 40 lbs each. The curing cycles consisted of three separate steps, as shown in Figure 2.1:

1. Heating until the temperature reached the value of 100°C, with a rate of 2.5°C/min
2. Holding the temperature of 100°C for 3 hours
3. Cooling down to room temperature with the same rate as the first step.

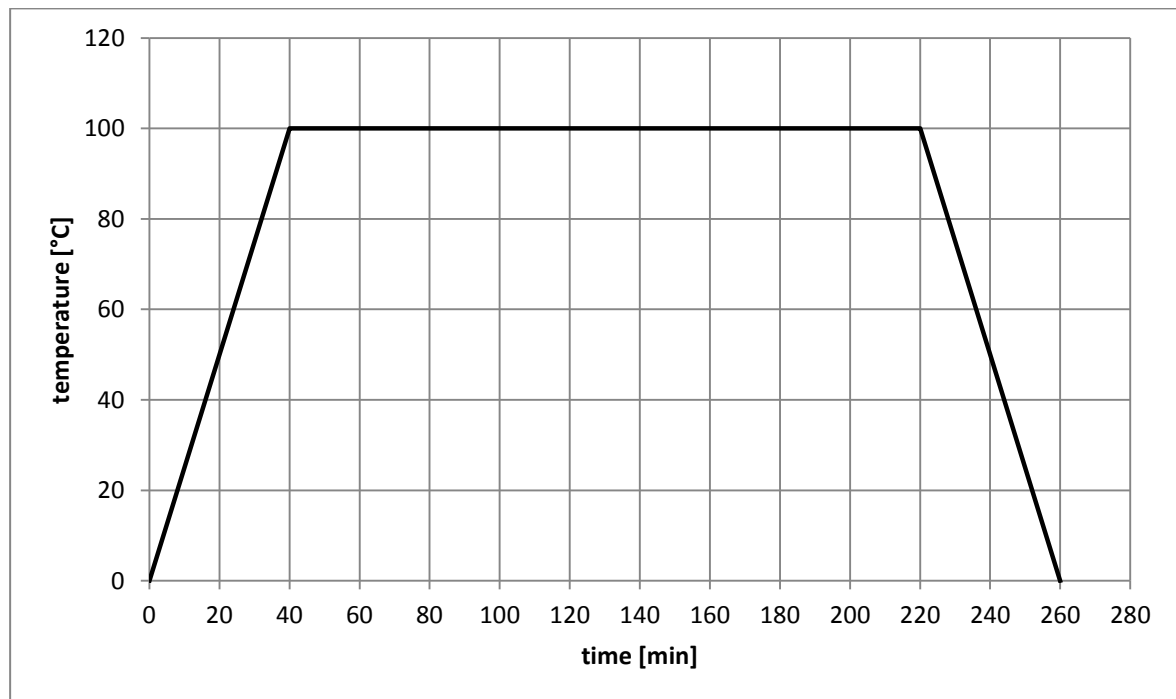


**Figure 2.1** Curing cycle for the laminate

### 2.3 Fiber volume fraction measurement

The total fiber volume fraction has been determined through the use of the matrix burn-off test. This method is designated to determine the resin and fibre volume fraction by removal of the resin from the reinforcement using a burn-off step.

Six specimens of dimensions approximately of 20 mm x 20 mm have been taken from different locations of each laminate considered. Subsequently every specimen has been put in a crucible suitable to hold it previously weighed. The whole of crucible and specimen has been weighed again and placed in a muffle furnace where the temperature of 600° has been reached and maintained for 5 minutes minimum. In this fashion the resin has been completely removed. After the cooling to room temperature, every crucible has been removed from the muffle furnace and weighed with its content. The fiber volume fraction has been calculated through the following equation 2.1.

$$V_f = \frac{\text{Volume fibre}}{\text{Volume fibre} + \text{Volume matrix}} = \quad (2.1)$$

$$= \frac{\text{mass fibre} / \text{density fibre}}{\text{mass fibre} / \text{density fibre} + \text{mass matrix} / \text{density matrix}}$$

Density of the fibre has been considered equal to 2560 kg/m<sup>3</sup>, value characteristic for E-glass present in literature, while the density of the matrix equal to 1812 kg/m<sup>3</sup> has been calculated taking into account the single densities of resin, curing agent and accelerator and the parts per hundred parts of resin (PPHR) in which they are present in the final compound.

## 2.4 Preparation of test-specimens

When the laminate was ready, the external frame has been removed and specimens of length equal to 230 mm have been cut from it with a water-cooled saw, in the attempt to limit damages to the edges. The dimensions chosen for the width of samples varied, depending on the direction of loading. For samples cut along the warp direction, the width was about 12.5 mm, while for samples cut along the weft, the width was about 9.5 mm. The aim was to obtain for specimens cut a similar configuration, i.e. with three visible z-tows for specimens cut along the warp and three weft tows for specimens cut along fill direction, as illustrated schematically in Figure 2.2. In fill direction, in fact, the minor breadth has been considered representative of the unit cell of the material slightly enlarged, while in the warp direction, for avoiding the cutting of the z-tows, which delimit the borders of the unit cell, it has considered more prudent adding to the width half warp tow for each side.

Both ends of the samples were ground with sand paper and tabs of length of 50 mm were glued, to provide a smoother load transfer from the grips to the specimens. The gauge length was therefore reduced to the value of 130 mm.

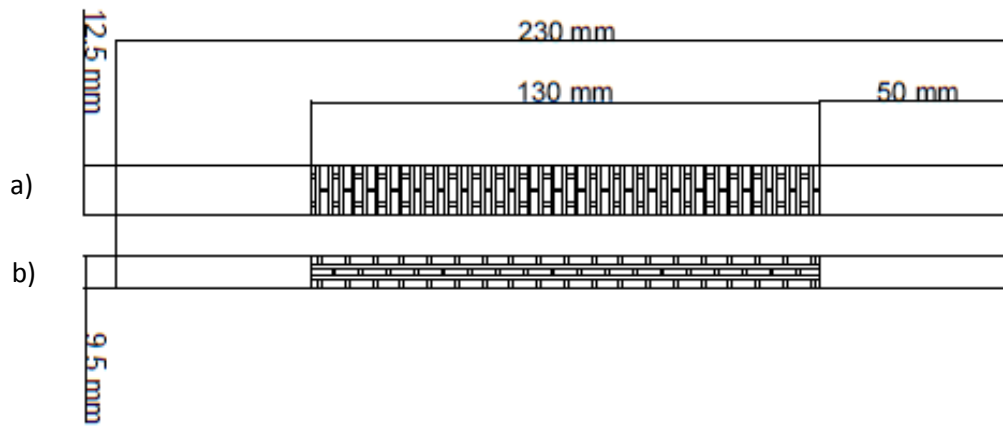


**Figure 2.2** Geometry and configuration of the fabric for specimens cut a) along the warp direction and b) along the weft direction.

## 2.5 Quasi-static and tensile fatigue tests

Quasi-static and tensile fatigue tests have been carried out using a servo-hydraulic machine Instron Series 1341 equipped with a 100 kN load cell. Before the tests, for each specimen width and thickness have been measured three times in different sites along the gauge length, to calculate the average cross – sectional area.

The strain that samples underwent during the tests has been measured through the use of a dynamic strain gauge extensometer Instron 2620 (full scale  $\pm 2.5$  mm), applied centrally onto the specimens with the help of elastic bands. Wrong reading of results due to possible movements during the tests have been prevented applying some drops of glue to the edge of the blades of the extensometer. The gauge length of the extensometer for tensile tests was 12.5 mm, while for the fatigue tests it was 96 mm. The problem was not present in fatigue tests because the machine was configured to stop the test before the extensometer reached and overcame its limits of strain. Tensile tests have been performed setting the rate of the extension equal to 1 mm/min. The data acquisition was set to retrieve one set of data every 0.1 s. The software used for test monitoring and data acquisition was Instron's Bluehill. The Young's modulus and the ultimate tensile strength have been calculated for each experiment.

During some of the tests, images of the specimen have been collected with a frequency of 0.2 Hz, taken with a professional digital camera Canon EOS 550D mounted on a tripod. The photo camera has been connected to the computer and the software utilized, EOS Utility, has permitted the collection of the photo automatically; in this way the analysis and the reconstruction of damage development into the material were performed.

The whole testing setting-up is shown in Figure 2.3, where single components have been indicated for facilitating understanding.

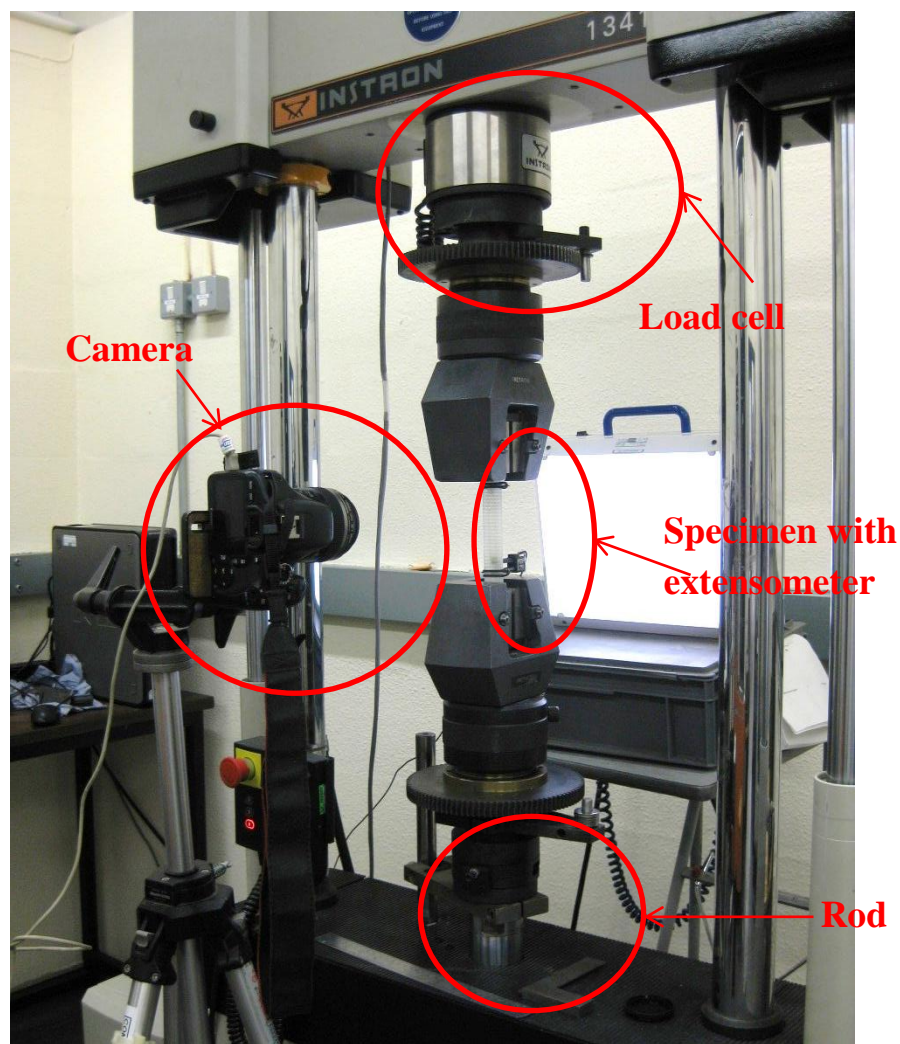


Figure 2.3 Quasi static and fatigue setup

---

The performed fatigue tests can be divided into two series, identified by the names of *low* and *high* stress level, the transition corresponds to the initiation of the cracking in quasi-static tests.

Fatigue tests have been carried out using an R-ratio equal to 0.1 and a frequency of 5 Hz. To describe with a considerable number of points each loop (200 points), the acquisition data rate has been set at 0.001s. However, after having carried out fatigue tests belonging to the series of *low stress level*, a problem of insufficient resolution of the description of the area of the hysteresis cycles with 200 points recorded for each has emerged. Then the acquisition data has been changed from 0.001s to 0.00067 s, permitting to record a major number of points and therefore to describe with more accuracy the trend for energy dissipated, as will be described in details in the next chapters.

## 2.6 Optical and scanning electron microscopy

The observations at the optical microscope required the preparation of samples of adapted dimensions. Specimens were therefore firstly cut to rough dimensions required with a saw equipped with a SiC cut-off wheel. Then the use of a precision cut off machine permitted to reach the exact location from where starting the process of grinding and polishing. After that, the samples were mounted into cylinder spacers, filled with epoxy resin constituted by 15 volume parts of epoxy resin and 2 parts of hardener from the Strueurs EpoFix Kit. After the curing of the resin, which takes long about 12 hours, the samples were ground and polished following as indicated in Table 2.3 and Table 2.4.

**Table 2.3** Grinding procedure

<b>Equipment</b>	PLANAPOL			
<b>Specimen holder</b>	PEDEMAX 6 SPECIMEN HOLDER			
<b>Disc/Cloth</b>				
<b>Grinding media</b>	SiC	SiC	SiC	SiC
<b>Grit/Grain size</b>	400	600	1200	4000
<b>Lubricant</b>	WATER			
<b>Speed [rpm]</b>	300	300	300	300
<b>Pressure [N]</b>	210	210	210	210
<b>Time [min]</b>	Until flat	2	2	1

**Table 2.4** Polishing procedure

<b>POLISHING</b>	<b>I</b>	<b>II</b>	<b>III</b>	<b>IV</b>
<b>Equipment</b>	PLANAPOL			
<b>Specimen holder</b>	PEDEMAX 6 SPECIMEN HOLDER			
<b>Disc/Cloth</b>	DP-DUR	DP-DUR	DP-DUR	OP-CHEM
<b>Grinding media</b>	Diamond suspension	Diamond suspension	Diamond suspension	OP-S/water
<b>Grit/Grain size</b>	6 $\mu\text{m}$	3 $\mu\text{m}$	1 $\mu\text{m}$	0,1 $\mu\text{m}$
<b>Lubricant</b>	BLUE			
<b>Speed [rpm]</b>	150	150	150	150
<b>Pressure [N]</b>	210	210	210	210
<b>Time [min]</b>	5	5	5	30s with OP-S 10s water and OP-S 10s water

The polishing and grinding have been carried out on a Streuers Pedemax-2, in groups of six specimens, to allow the balance of the specimens during the spinning involved in the process. The preparation of samples is common to both optical and scanning electron microscopy, conducted respectively on a Zeiss axiophot transmitting light microscope and on a Hitachi S 4000 SEM. Before continuing with the description of the other techniques involved, the principles of operation of the scanning electron microscope are presented followed by an overview of how micro computed tomography operates.

## 2.7 Scanning Electron Microscope

The resolving power of modern optical microscopes are limited not only by the number and quality of the lenses, but above all by the wavelength of light used for illumination. Taking into account that the average wavelength of visible light is around 550 nm, resolution doesn't go beyond the limit of 250 nm. These problems are overcome with the use of Scanning Electron Microscopy, which exploits the shorter wavelength of electrons for obtaining better resolutions typically comprised in the range of 1-20 nm. Figure 2.4 shows schematically the components of a common SEM, which permit the generation and the focusing of an electron beam over the sample surface, following a vertical path.

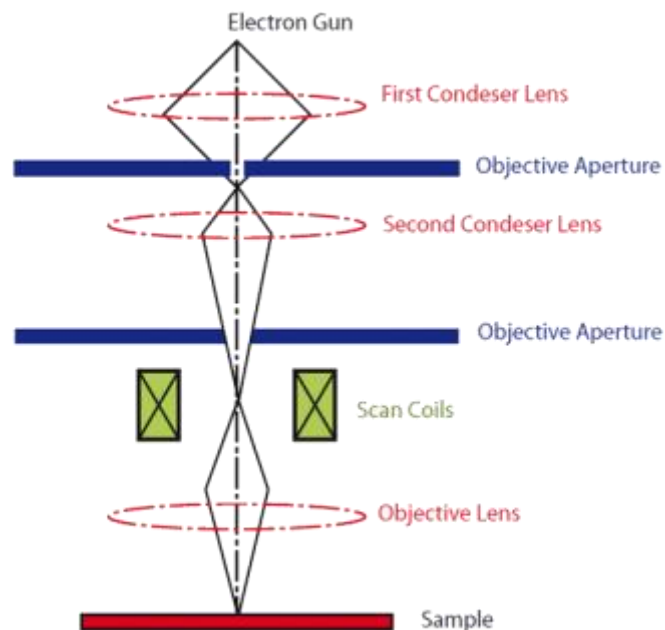


**Figure 2.4** Schematic diagram of a scanning electron microscope

Initially, an electron gun, constituted by a tungsten filament, a cathode and anode plates, produces the beam, formed by a number of electrons controlled through a system of condenser lenses. The objective lens focuses the beam into a spot on the sample, while the scan coils controls the position of the electron beam, permitting its deflection over the surface of the specimen. SEM requires two conditions which distinguish it from the optical microscope: the whole apparatus, sample included, needs to be under a vacuum environment, for avoiding the absorption of the electron beam from molecules present in air and sample



needs to be conductive enough to dissipate the charge of electrons. Once that the electrons interact with sample, they penetrate into its depth for few microns. As a result of this interaction, different signals are produced, like secondary electrons, backscattered electrons and X-rays. Signals are then collected by different types of detectors, typically a secondary electron detector and a backscattered detector, providing different images which give the idea of the difference in density.

## 2.8 X-ray Micro Computed Tomography

X-ray Micro Computed Tomography is one of the most effective non-destructive techniques for imaging the internal structure of the material. The resolution of collected images achievable is sufficient to permit the detection of features of few  $\mu\text{m}$  size order, thus the method is useful to investigate the link between microstructure and damage evolution. The principles of operation are briefly described. A cone of X-rays is emitted from a target, passes through the specimen and is captured by a panel detector put opposite to the gun. The specimen is continuously rotated around its axes during the scan, while projections (X ray radiographs) are recorded for each orientation. The set of projections are then reconstructed into a 3D volume, using a filtered back projection algorithm. A schematic diagram of the micro CT setup is shown in Figure 2.5.

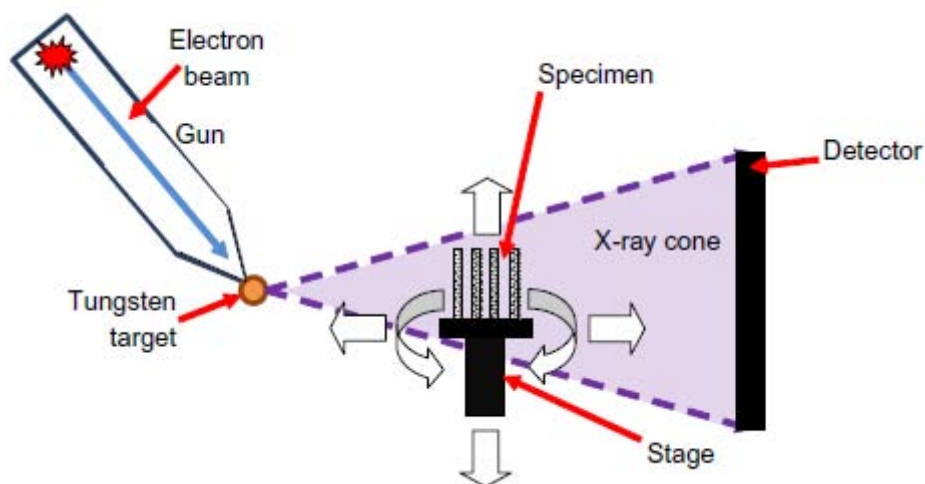


**Figure 2.5** Principles of operation of micro computed tomography. Courtesy of McCombe (2011)

The machine used for the Micro CT analysis was a Nikon Metrology 225/320kV Custom Bay, present at the Manchester X-ray Imaging facility (MXIF) shown in Figure 2.6.



**Figure 2.6** Internal view of the Nikon Metrology 225/320 kV Custom Bay. X ray source, specimen stage and detector are highlighted with red circles

The machine was constituted principally by a X-ray source, a sample manipulator, which permitted the rotation of the specimen around its axes, a specimen stage and a detector, located opposite to the source respect to the sample. The Custom Bay allowed to analyse specimen with a cross section variable from 3-230 mm. Each scan took a time variable from 5 to 120 mm and image resolution was approximately  $1/2000^{\text{th}}$  of the sample diameter so voxel sizes ranged from 5 to 100  $\mu\text{m}$ . With the term voxel, it is indicated the basic unit of computed tomography reconstruction, i.e. the smallest distinguishable box-shaped part of a three-dimensional space. The name is due to the combination of the terms pixel and volume.

The source chosen for the analysis of the current project was a 225 kV with a tungsten target.

Specimens were firstly mounted on a base, and then the whole of sample and base were mounted in the manipulator stage, taking care that the center of the sample was close to the center of rotation. The sample was then positioned for the scanning. The positioning was a crucial step in the preparation for the analysis, since the resolution depended prevalently on

the distance of specimen to source. Getting closer the specimen to source meant to improve the resolution. The next step was the definition of flux of X-rays energy, through the setting of values of accelerating voltage and current. The accelerating voltage determined the velocity of electrons; as it was increased the energy of x-rays augmented. The current, instead, influenced the directly the number of x-rays emitted. These two parameters were correlated with the brightness of the image, since higher value of current and voltage allowed the passage of more x-rays through the specimen and the achievement of the detector. Accelerating voltage value adopted was equal to 60 kV, while current was 200  $\mu$ A.

Two specimens were scanned singularly, one representative for warp direction loading, and the other for weft direction loading. The samples were fatigue tested to respectively a peak stress of 200 MPa (correspondent to an initial peak strain of 0.89%) and to 175 MPa (correspondent to an initial peak strain of 0.7%). The tests were stopped before the final failure was thought to occur, so that the shock wave, which took place with the failure, did not add further damage not directly connected with fatigue cycles.

The difference between the width of the two specimens (breadth equal to 8.33 mm for weft specimen and 13.19 for warp specimen), allowed to reach a higher resolution for the weft sample (5.3  $\mu$ m) respect that the warp one (6.9 $\mu$ m). The values of resolution were given by the program Metris CT pro 3D used for the reconstruction of raw files.

## 2.9 Thermographic observations

Investigations on the temperature evolvment experienced by specimens during fatigue tests have been conducted with two different infrared cameras. In the first experiments the IR camera used was a Flir E4, which features were a temperature range between  $-20^{\circ}$  and  $250^{\circ}$ C, resolution of 80 x 60 pixels, accuracy of  $\pm 2\%$  of reading, thermal sensitivity  $<0.15^{\circ}$ C and image update rate of 9 Hz. The lack of sufficient resolution of images collected with this camera suggested the use of the second type of IR camera, a Flir A320. The characteristics of the latter were a temperature range between  $-20^{\circ}$  and  $120^{\circ}$ C, resolution of 320 x 240 pixel, accuracy of  $\pm 2\%$  of reading, thermal sensitivity of  $0.05^{\circ}$ C at  $30^{\circ}$ C and image update rate interchangeable from 9 Hz to 30 Hz. The availability of the two cameras allowed the execution of two different types of tests. In the first one, while specimens were fatigue tested – with a frequency of 5Hz and a R=0.1 as described in the previous sections – thermal images

---

were collected every 100 cycles for the first 1000 cycles, and then every 1000 cycles until the final failure happened. These series of tests were carried out only for the warp direction loading, for peak stress values of 200 MPa and 250 MPa. These levels of stress were chosen so that the failure was expected to be observable in a reasonable length of time and the risk that failure took place near the grips was limited. This event, in fact, was observed to occur more frequently for higher peak stress (e.g. equal to 300 MPa and 350 MPa). The second type of test, instead, consisted in a 60 Hz video recording of the first 600 cycles of a fatigue test with a peak stress of 200 MPa, a frequency of 5 Hz and a  $R=0.1$ . The aim of the test, as will be explained in details in Chapter 7, was the detection of the initiation of matrix cracking into the sample and its effect on temperature changing. However it has to be taken into account that only development of the specimen surface temperature could be detected, such that only the effect of cracks coming to the surface was seen, while influence of inner cracks was hidden.

## 2.10 Summary

In this chapter manufacturing details of the specimens were given. The specimens consisted in a single ply of 3D woven composite fabric of E glass fibres embedded in an epoxy resin. Fibre volume fraction was measured with burn.off tests.

The second part regarded the description of quasi-static and fatigue testing setup and of techniques used to observe damage development into tested specimens. In particular optical and scanning electron microscopy are presented X-ray micro computed tomography and thermography. For the former, specimen sectioning and preparation were described, while for SEM and micro-CT a brief overview of the principles of operation was provided.

The next chapter will describe the characterization of the material in terms of architecture and fiber volume fraction.

# Chapter 3

## Characterization of the microstructure

### 3.1 Introduction

In this chapter the structure of the material is analysed and discussed. Untested specimens are sectioned and examined through optical microscopy. Images show not only the architecture, but also characteristic defects of the fabricated composite, such as voids and micro delaminations. Possible explanations of their presence will be discussed. In the second part results of the burn off tests are presented, in a fashion to determine the fiber volume fraction of specimens.

### 3.2 Architecture of the fabricated composite

The architecture of the fabric is represented schematically in Figure 3.1. Tows colored in red represent warp tows, in blue weft tows are denoted while in green z-tows. As it can be seen, although the configuration is similar to that of a  $[90/0/90/0]_s$  cross-ply, fibers are organized in distinct tows rather than constituting an interrupted layer of fibers. This permits an easier weaving of z-binder through the thickness. In the figure 3.1 the axis, set to ease the distinction between different tows and schematize the material, follow the cartesian convention.

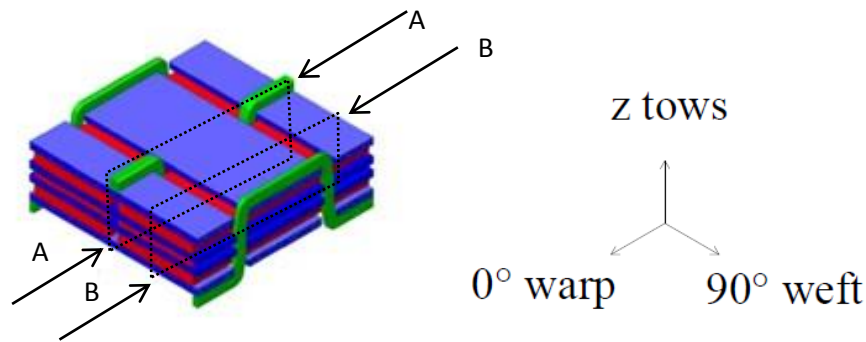


**Figure 3.1** Schematization of 3D-96 fabric. Axis convention and section planes are indicated.

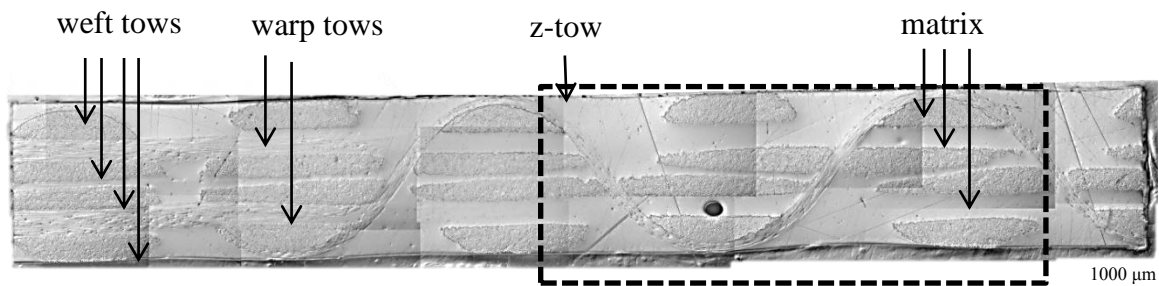


**Figure 3.2** Microscope image of section A-A

Figure 3.2 represents a panoramic view of a specimen sectioned along the plane A-A indicated in Figure 3.1. In the left hand-side of the image, weft tows are still visible, as the direction of cutting doesn't follow perfectly the direction of z-tow. As it can be observed, z-tows described a pattern which is not orthogonal as schematized in Figure 3.1, but rather describable as sinusoidal. This affected the disposition of weft fibers tows, distancing one from another, and creating resin gaps between adjacent weft tows. These gaps, as it will be described in detail in next chapter, constituted locations subjected to possible matrix cracking in fatigue loading. An explanation of the wavy pattern of z-reinforcement was given by Mouritz et al (2008). They found that the tensile load applied to weave the z-binders through the thickness of the fabric and to ensure they are sufficiently taut, obliged the z-reinforcements to follow a sinusoidal-shaped rather than a square-shaped orthogonal profile. Another important remark is the absence of warp tows in correspondence of sections occupied by z-tows. The presence of through-thickness reinforcements, in fact, creates resin-rich regions between adjacent warp yarns. The warp are thus pushed sideways during the weaving

to make space for the z-binders, forming gaps between neighboring yarns, then filled with polymer during the infusion.

The section indicated in Figure 3.2 with dashed lines can be considered representative of a unit cell and is reported magnified in Figure 3.3. The principal dimensions are there indicated.

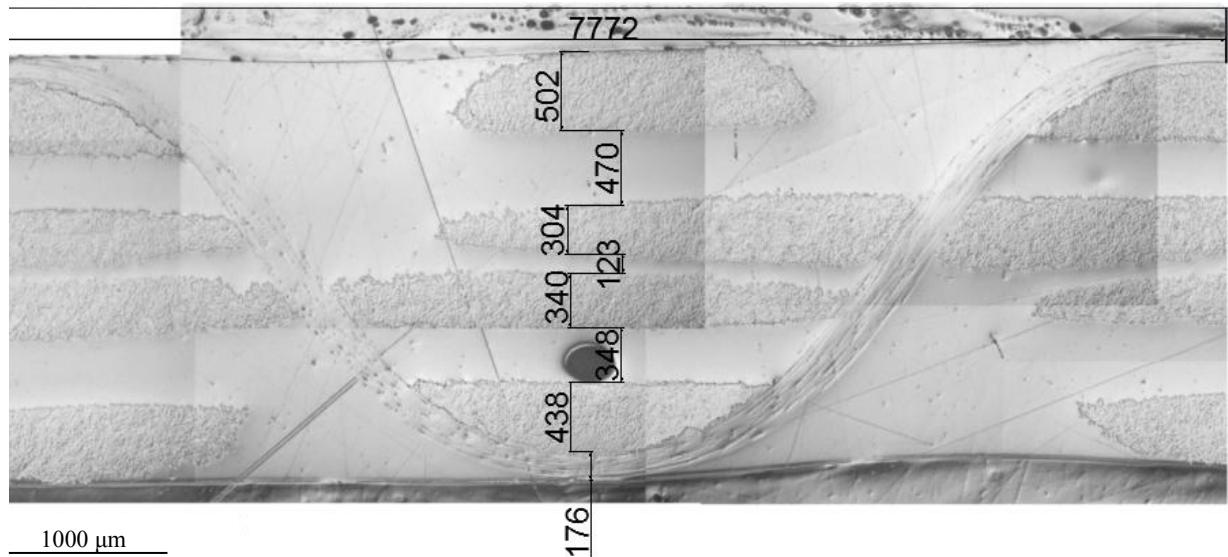


**Figure 3.3** Magnification of microscope image of section A-A reported in Figure 3.2, where considered section is indicated with dashed lines. Note: the units are  $\mu\text{m}$ .

As it can be seen, inner weft tows have average thickness smaller than external tows and, consequently, larger width having the same weight per unit length. Their profile is not as regular as the bottom and top tows. A possible reason may be found in the influence played by z-reinforcements. These, in fact, are thought to act as constraints for external weft yarns, limiting the movements of the latter and preserving the regularity of their shape.

The width of the unit cell, i.e. the distance between adjacent crossovers of the z-tow with top weft yarns (called z-crowns), is about 7,7 mm, a value near to the declared 7,6 mm of 3TEX. This value of 7.6 mm was calculated by inverting the density insertion of weft yarns as shown in equation 3.1.

$$\text{Width unit cell} = \frac{2}{\text{weft insertion density}} = \frac{2}{2.64 \left[ \frac{\text{picks}}{\text{cm}} \right]} = 0.76 \text{ cm} \quad (3.1)$$

Even the top and bottom weft yarns, when compared one another, showed different height in correspondence of sections where z-crowns are visible. This suggested that the crossover of the z-tow with the underlying weft tow caused a crimp of the latter, which determined a reduction of height and a consequent increase in breadth.

For completeness, in Figure 3.3 is reported the microscope image obtained sectioning the specimen in correspondence of the plane B-B, indicated in Figure 3.1. In this case warp yarns are visible in regions before occupied by resin. The pattern of z tow, just overcome, is still recognizable because of the ordered disposition of those external weft tows crossed-over by the reinforcement and the distinguishable sinusoidal shape described by adjacent matrix pockets.

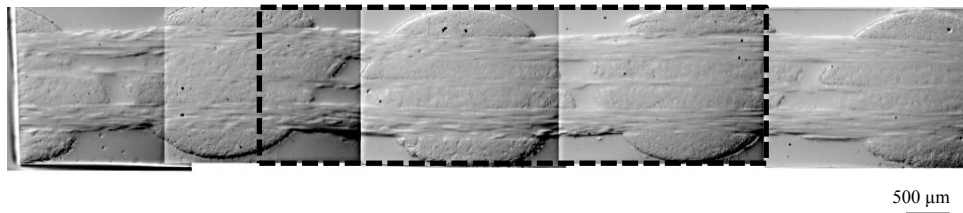


**Figure 3.4** *Microscope image of section B-B*

As it was expected, inner warp yarns appear thinner than external ones, being characterized by a lower weight per length (1100 tex for middle and 2275 tex for top and bottom layer yarns).

In a similar way to that done for section A-A, a section representative of the unit cell is enclosed by dashed lines and shown magnified in Figure 3.5.



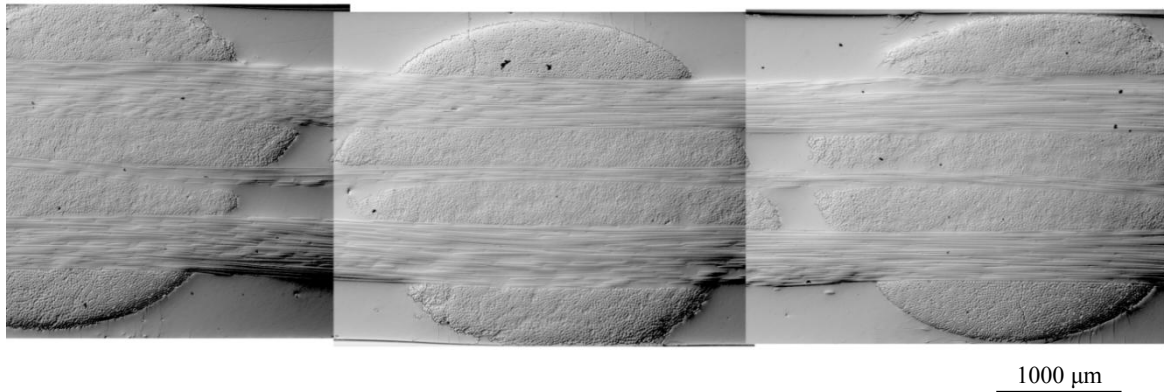


**Figure 3.5** Magnification of microscope image of section B-B shown in Figure 3.4, where the considered section is enclosed by dashed lines.

It is interesting to note how z-tow influences not only the shape of external weft tows, but also the inner tows profile, the contours of which follow the sinusoidal geometry.

### 3.3 Fiber volume fraction determination

As described in Chapter 2, fibre volume fraction was measured using the burn-off technique. Table 3.1 reports the counts made to calculate the density of the resin, taking into account the three components.

**Table 3.1** Density resin for selected resin

	Density of single components [kg/l]	PPHR	%	Final density [kg/l]
Shell Epikote 828	1,16	100	60,98	1,182
MNA	1,232	60	36,59	
Ancamine K61B	0,97	4	2,44	

After having calculated the density of the resin (equal to 1182 kg/m<sup>3</sup>), it has been possible to calculate the average volume fibre fraction of laminates produced. Table 3.2 reports in the first three columns the weights of crucibles and specimens expressed in grams, measured before and after burn-off test. In the fourth column, the weight of fibers is calculated

subtracting the weight of crucibles to the sum of weight of crucible and specimen measured after the test. The weight of matrix reported in the fifth column is obtained, instead, as the difference between the weight of specimens measured before the burn-off test and the weight of fibres before calculated. The percentage of fibres can be calculated with equation 2.1.

The results of six different measurements taken each for three different laminates are reported.

**Table 3.2** Burn-off tests measurements for three different laminates and resulting average fibre volume fraction.

<b>Before test</b>		<b>After test</b>				
<i>weigh</i> <i>crucible [g]</i>	<i>weigh</i> <i>specimen [g]</i>	<i>weigh</i> <i>crucible+specimen [g]</i>	<i>Specimen</i> <i>(Fiber)</i>	<i>Specimen</i> <i>(Matrix)</i>	<i>Vf</i>	<i>Average</i>
49,424	1,897	50,67	1,246	0,651	0,469	0,475
50,616	1,898	51,859	1,243	0,655	0,467	Dev Std
50,743	1,786	51,907	1,164	0,622	0,464	0,0099
51,621	1,781	52,812	1,191	0,59	0,482	
39,921	1,774	41,123	1,202	0,572	0,492	
46,054	1,781	47,233	1,179	0,602	0,475	
<b>Before test</b>		<b>After test</b>				
<i>weigh</i> <i>crucible [g]</i>	<i>weigh</i> <i>specimen [g]</i>	<i>weigh</i> <i>crucible+specimen [g]</i>	<i>Specimen</i> <i>(Fiber)</i>	<i>Specimen</i> <i>(Matrix)</i>	<i>Vf</i>	<i>Average</i> <i>Vf</i>
42,28	1,476	43,756	0,980	0,496	0,477	0,492
51,497	1,464	52,961	0,981	0,483	0,484	Dev st
48,41	1,244	49,654	0,823	0,421	0,474	0,02
49,397	1,257	50,654	0,883	0,374	0,522	
47,421	1,524	48,945	1,027	0,497	0,488	
51,594	1,269	52,863	0,874	0,395	0,505	
<b>Before test</b>		<b>After test</b>				
<i>weigh</i> <i>crucible</i> <i>[g]</i>	<i>weigh specimen</i> <i>[g]</i>	<i>weigh</i> <i>crucible+specimen</i> <i>[g]</i>	<i>Specimen</i> <i>(Fiber)</i>	<i>Specimen</i> <i>(Matrix)</i>	<i>Vf</i>	<i>Average</i> <i>Vf</i>
46,053	1,709	47,201	1,148	0,561	0,486	0,484
48,328	1,748	49,513	1,185	0,563	0,493	Dev st
39,92	1,754	41,075	1,155	0,599	0,471	0,008
50,322	1,712	51,484	1,162	0,55	0,494	
52,774	1,75	53,938	1,164	0,586	0,478	
50,603	1,743	51,767	1,164	0,579	0,481	

The average fiber volume fraction, calculated as the arithmetic average of the three different results, can be therefore assumed equal to  $0.489 \pm 0.007$ . This result can be compared with values of fibre volume fraction present in literature for 3D composite materials made up of the same woven fabric. Lomov et al (2009), for example, have studied and characterized a 3D composite material made up of the 3D-96 fabric embedded with epoxy-vinyl ester resin and fabricated with Vacuum Assisted Resin Transfer Moulding (VARTM) technique. Though the method of fabrication and the resin used are different, the fibre volume fraction that they determined is exactly the same: 48.9%. It can be concluded that the in-house wet impregnation technique, used for the current project, permits to produce composites characterized by fibre volume fraction in a way similar to more established and widely used wetting techniques such as VARTM.

### **3.4 Defects of the fabricated material: voids and micro delamination**

Microscope images of untested specimens have permitted not only the characterization of the structure from the point of view of the architecture, but also the detection of defects present in the fabricated material before any kind of test would be carried out. It is important, indeed, to establish the presence of these before quasi-static or fatigue tests are carried out, as they can act as potential sites of initiation of cracks. The visible defects that can be distinguished are of different nature. The first kind is represented by the presence of air bubbles trapped within the material, while the second one is represented by micro-delamination running near the interface of z tows and weft tows. In Figure 3.6 both types of defects are shown.

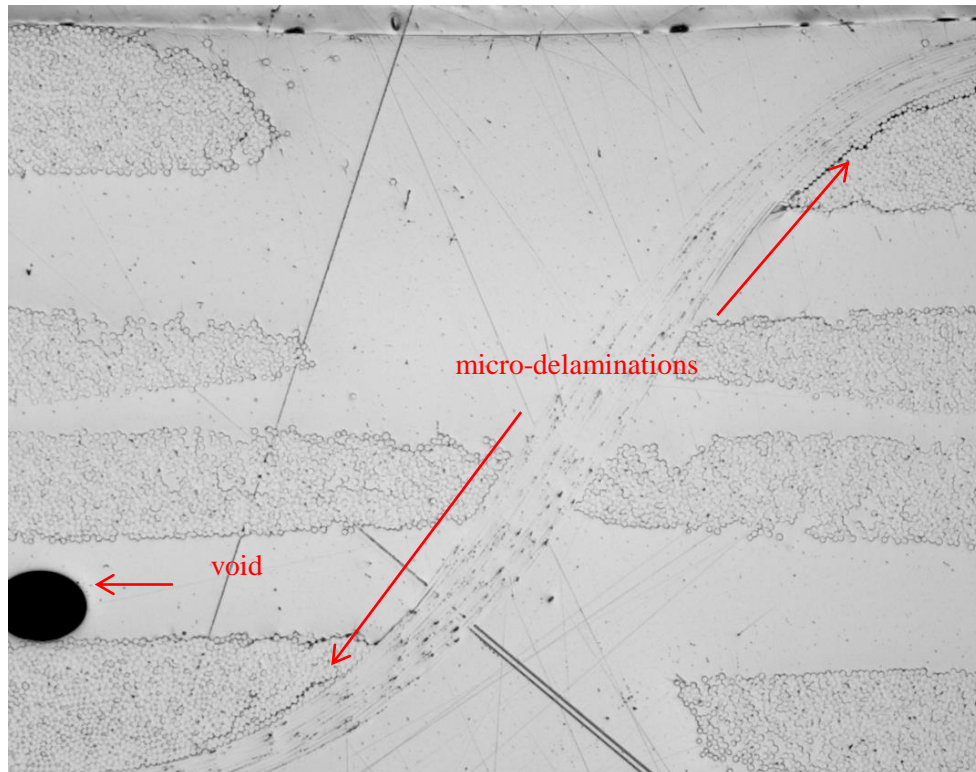


**Figure 3.6** Representation of defects of the fabricated composite present into untested specimen: air bubbles trapped into the specimen and micro-delamination at the z-tow and weft tows interface.

The cause of the presence of air bubbles is a consequence of the manufacturing process of the laminates. The fabrication procedure above described, was the result of slight adjustments and modifications to the original in-house wet impregnation technique, used and optimized for the production of laminates made up with a 3D-78 fabric. This type of fabric presented a structure similar to the one of the fabric object of study of this project. The difference consisted in the smaller number of warp and weft, respectively equal to 3 and 2. Details can be found into Baiocchi's dissertation (2013). Alterations to the manufacturing method were introduced to take into account the major complexity of structure of 3-D 96 fabric. The aim was to reduce the amount of air inclusions, already visible at a visual inspection once that the laminate was ready. Modifications included:

- repetition of mixing - degassing process to ensure to reach the best homogeneity of the compound and to reduce the presence of air inclusions;
- presence of two steel plates pre- heated at 100°C placed at the bottom of the vacuum chamber, to improve the wetting of fabric. The temperature of 100 °C has not to be overcome more than 40°C. The use of two steel plates preheated at 140°C, in fact, resulted in a laminate

in which the resin was spread and accumulated towards the borders, leaving the center of the fabric deprived of a sufficient amount of it.

Although the alterations permitted to obtain laminates with a minor amount of air inclusions, the presence of these in correspondence of sections occupied by z-tows could not be avoided. From microscope and micro CT images, they have been established to be in correspondence of resin-channels comprised between two adjacent warp tows, under weft tows crossed over by z-binders. Figure 3.7 shows a typical image taken through computed tomography. Their presence, as will be described in Chapter 6, was assumed not to affect fatigue damage development into the material, as the initial cracks were observed to start forming from different sites.

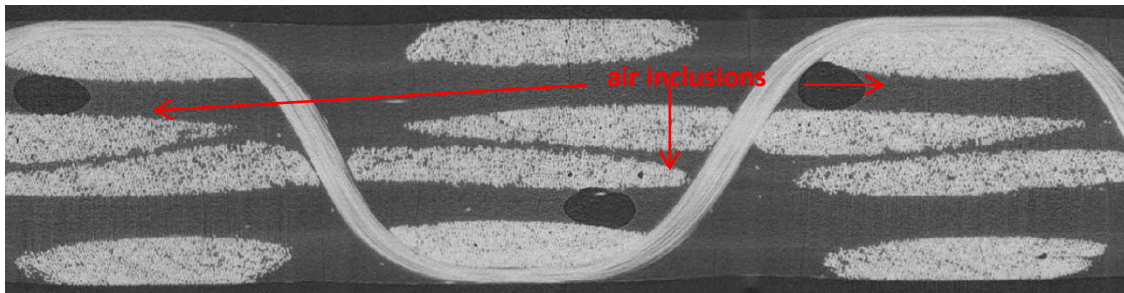
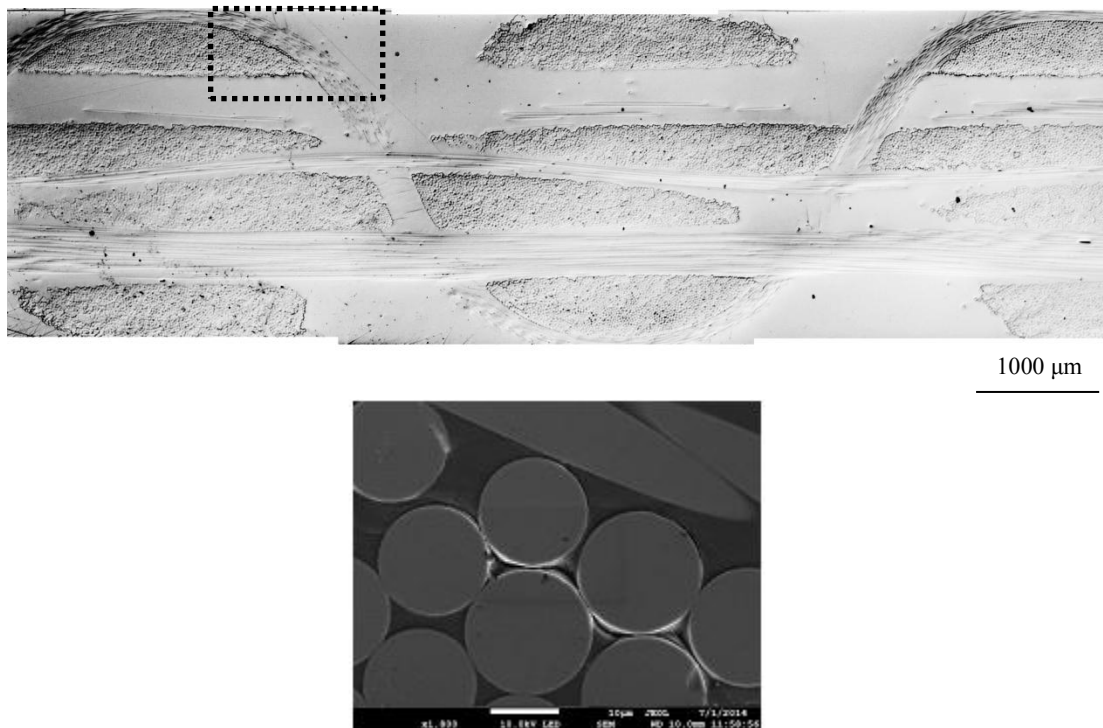


**Figure 3.7** Micro CT image taken in correspondence of a plane parallel to warp direction where a z-tow is visible. Air bubbles are indicated with arrows.

The second type of defect detected in untested specimens was constituted by micro-delaminations developed near the regions where z-binders initiated the crossing-over of adjacent weft tows. Figure 3.7 shows a microscope image of this damage. Cracks run along the direction parallel to the z-reinforcement, developing along the interface of fibre-matrix. The term micro-delamination is used here although this is theoretically incorrect. The site of damage, in fact, was near the interface of z and weft tow, but the crack developed between fibres belonging to the weft tow. They run only for a limited length in the plane parallel to the z-tows, not going over the centre of z-crowns. Another direction of growth followed the direction parallel to warp tows, along the interface of weft tow and subjacent resin gap. Even in this case, the micro-delaminations were limited in length. Interestingly, cracks did not develop at the interface shared between weft and z-tows. Micro delaminations were observable only in correspondence of the sections parallel to warp tows, where z

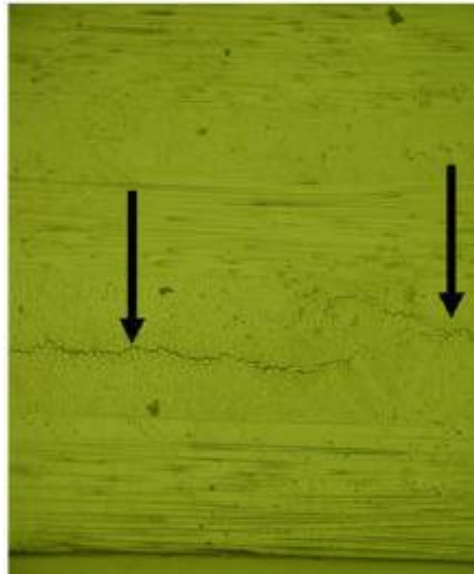
reinforcement was visible. A possible explanation of their formation could be the thermal shrinkage which the composite material is subjected to, during the last step of curing of manufacturing process. The differences in free contractions between fibers and matrix, in fact, would provoke the appearance of thermal stresses that might cause the formation of these defects during the cooling. The thermal shrinkage is not the only type that can occur, as the resin is subjected to shrinkage of chemical nature when it cures.

Figure 3.8 shows another optical image taken from an untested specimen where micro-delaminations were visible. The area enclosed by dashed lines is then magnified and observed by means of scanning electron microscope image, where it could be noticed that micro-delaminations grew along the interfaces of matrix-fibers of weft tows closest to the z-tow.



**Figure 3.8** Optical and SE micrograph images taken from composite 3D -96 untested specimen

An inspection of virgin specimens made up of similar 3D composite material, was conducted also by Lomov et alii (2009). Through the use of optical microscopy, they found occasional and rare residual micro cracks, caused by thermal/curing shrinkage. The principal difference with what observed in this work, is the different location. Micro-cracks were in fact set inside the yarns and oriented along the plate faces. Figure 3.9 shows a micrograph with residual cracks taken from their work.



**Figure 3.9** Micrograph of 3D-96 composite material of virgin specimens. Residual cracks are indicated by arrows. Lomov et alii (2009).

### 3.5 Summary

In this chapter, the architecture details of the fabricated composite material were described, with the aid of microscope images taken from untested specimens. Sectioning the specimen along the warp direction, it was observed that z- tows followed a wavy weaving pattern through the thickness of the material, explaining that it could be originated from the tensile loading applied during the weaving process of the fabric. Also the presence of resin rich areas was detected, due to the necessity of z-binders to interlace warp and weft tows together. Furthermore principal dimension of different warp and weft tows were measured and compared, as different layers resulted into different values of thickness. The calculated average values of fibre volume fraction volume equal to  $48.9 \pm 0.7\%$ . This result was in excellent agreement with fibre volume fraction reported in literature for 3D composite material made up with the same fabric.

In conclusion, the chapter presented the defects of the fabricated composite. Microscopy observations conducted on untested specimens revealed the presence of air inclusions and micro-delaminations. The formers were situated into the matrix pockets underneath the weft tows crossed by z-binders while the latters were settled in correspondence of the interfaces of weft tows and z- reinforcements. In the next chapter the results of quasi-static tensile test are presented





# Chapter 4

## Quasi-static tensile test results

### 4.1 Introduction

In this chapter quasi-static tensile tests results are reported and discussed. Since specimens have been tested in warp and weft directions, the chapter will be divided into three sections: in the first two, mechanical properties and damage development of each will be discussed and in a third and final section a comparison of both will be given. Outcomes will be related to observations present in literature.

### 4.2 Response of the material tested in the warp direction

Figure 4.1 shows a typical stress- strain curve obtained testing specimens along the warp direction.

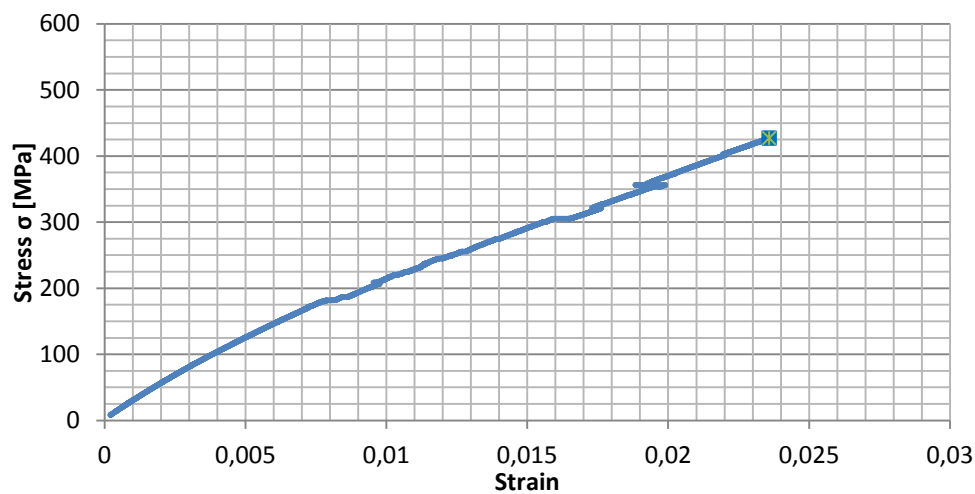


**Figure 4.1** Typical stress-strain curve of a specimen tested along warp direction.

As can be observed, the stress strain curve shows an irregular trend. Firstly it is linear until a value of strain equal to 0.3%. Then, it registers a knee and the slope decreases until the value of strain of about 0.75% is reached. At that point (corresponding to a stress level of 175 MPa), the curve assumes an irregular pattern, showing a decrease followed by a what appears to be a constant slope with irregularities. This trend is repeated as the loading continues. Finally, at the strain level of about 2.64%, the final failure occurs.

The abovementioned deviations can be explained as the effect that damage development exerts on stiffness. The stiffness, in fact, reduces progressively as the matrix cracking initiates and accumulates into the specimen. Cracks affect the distribution of load, diminishing the effective amount of material that can bear the load and therefore reducing the stiffness.

Young's modulus (E), ultimate tensile strength (UTS) and measured strain to failure are reported in Table 4.1. The Young's modulus values were calculated using the strain range of 0.05 % - 0.2%

**Table 4.1** Test results: mechanical properties.

Specimen	Ultimate Tensile Strength [MPa]	Ultimate Tensile Strain	Young's Modulus E [GPa]
1	460,8	0,0234	27,2
2	426,8	0,0223	26,9
3	501,3	0,0263	26,3
4	495,0	0,0296	24,4
<b>Average values</b>			
	470,9	0,0254	26,2
<b>Standard Deviation</b>			
	34	0,003	1

In Table 4.2 mechanical properties obtained from the quasi-static tensile tests are compared with the ones obtained from Lomov et al (2009). They found lower values for UTS and Young's Modulus, while the strain to failure measured was higher. These differences are believed to be caused by the dissimilar Epoxy-Vinyl Ester resin used by Lomov et al and the fabrication of the composite materials (VARTM).

**Table 4.2** Comparison between test results and mechanical properties present in literature.

Ultimate Tensile Strength [MPa]		Strain to failure [%]		Young's Modulus E [GPa]	
Lomov et al	This work	Lomov et alii	This work	Lomov et alii	This work
429±34	470±34	2.74±0.29	2.54±0.33	24.3±1.2	26.2±1.3

Visual (photographic) observations showed that the first cracks started to form in the resin rich regions at a level of strain equal to above 0.6% (see Figure 4.2). They are sited between two contiguous weft tows and oriented orthogonal to the direction of the loading of the material. The length of these cracks grows rapidly along the whole width of the specimen with increasing strain, connecting micro-cracks initiated near so called Z-crowns (i.e. short surface segments of Z yarns oriented in warp direction and laying on the weft yarns beneath them). Cracks seem to occur between the Z tows and the underlying wefts. This kind of damage can be seen in Figure 4.2, which shows transmitted light photos of the surface of the specimen taken during the tests.

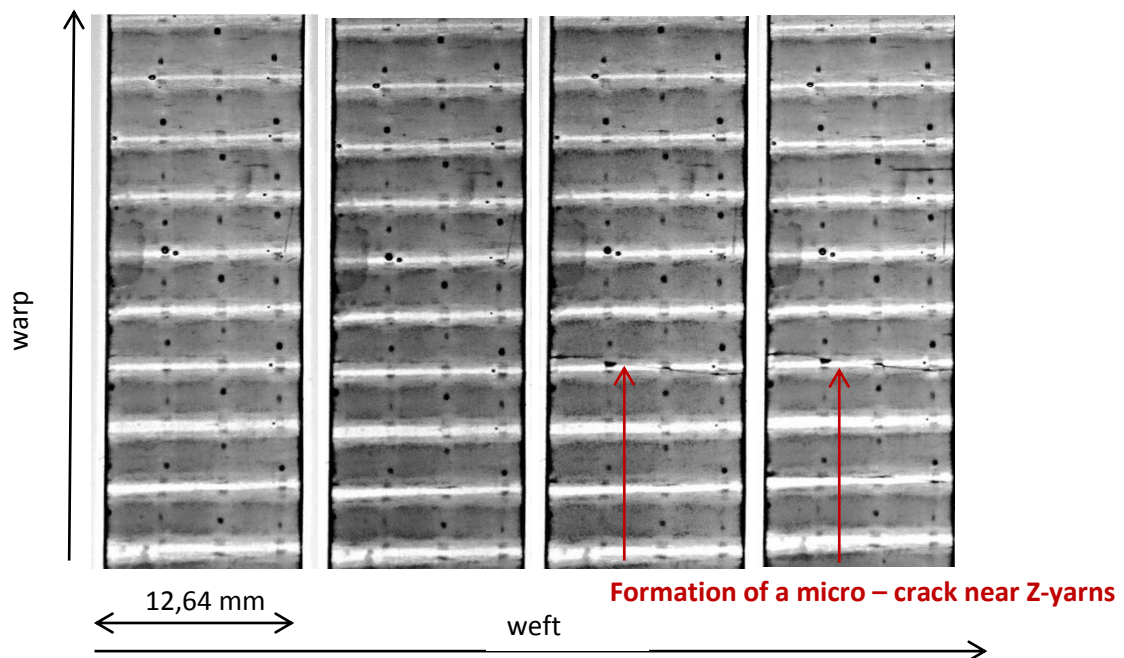


**Figure 4.2** Damage development in 3D- 96 composite loaded in warp direction. Formation of a micro crack near Z-yarns(indicated by arrows) is reported in photos. taken respectively in correspondence of 0.64%, 0.68% ,0.72% and 0.76% strain levels.

When the strain reaches the value of 1.4%, the whole gauge length of the specimen appears saturated with cracks in resin rich regions, whose length extends along the entire width of the sample.

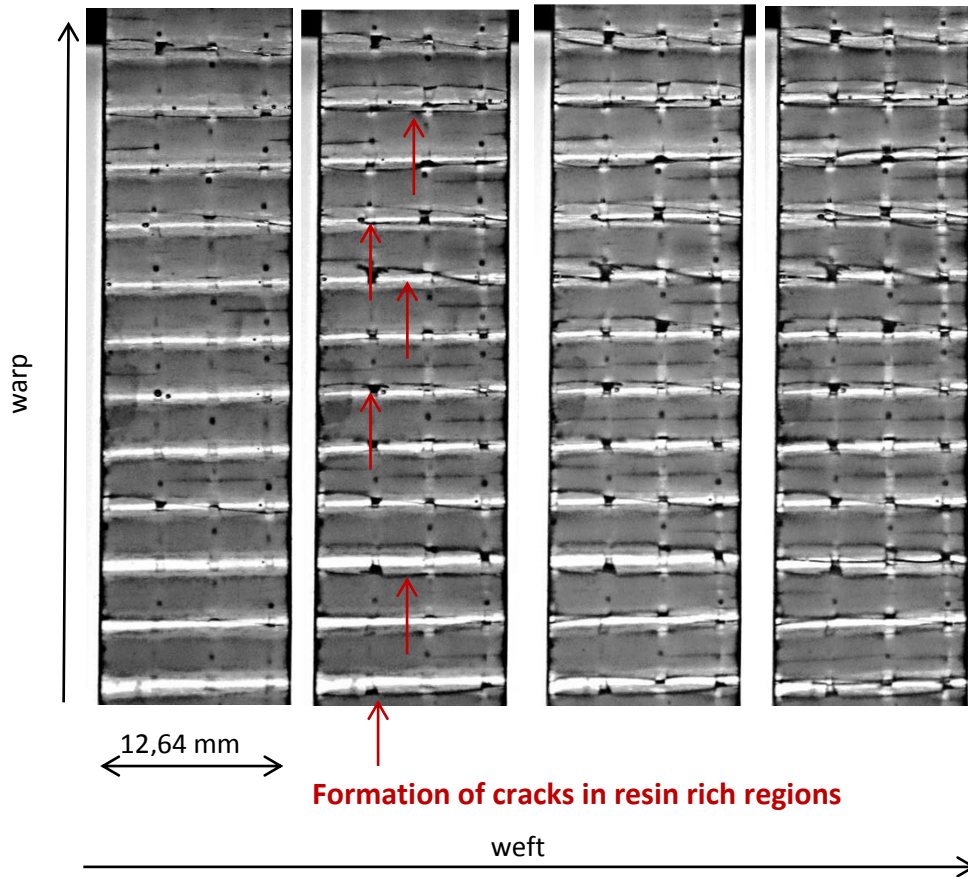


**Figure 4.3** Damage development in 3D- 96 composite loaded in warp direction. Accumulation of cracks until the achievement of saturation of Z-bundle-boundary crack (indicated by arrows) is seen. Corresponding strain levels are respectively 1.0%, 1.2% ,1.4% and 1.6%.

These cracks are not the only ones visible: further cracks propagate from the edges of the sample, lying within the matrix regions of the weft tows, at right angles to the loading direction. Preferential development of edge cracking has been widely discussed in literature and is known as the 'free-edge effects'.

The development of the final failure of the specimen is not currently understood. At some point, the fibers of the warp tows adjacent to the damaged weft tows start to fail catastrophically splitting the specimen into two parts.

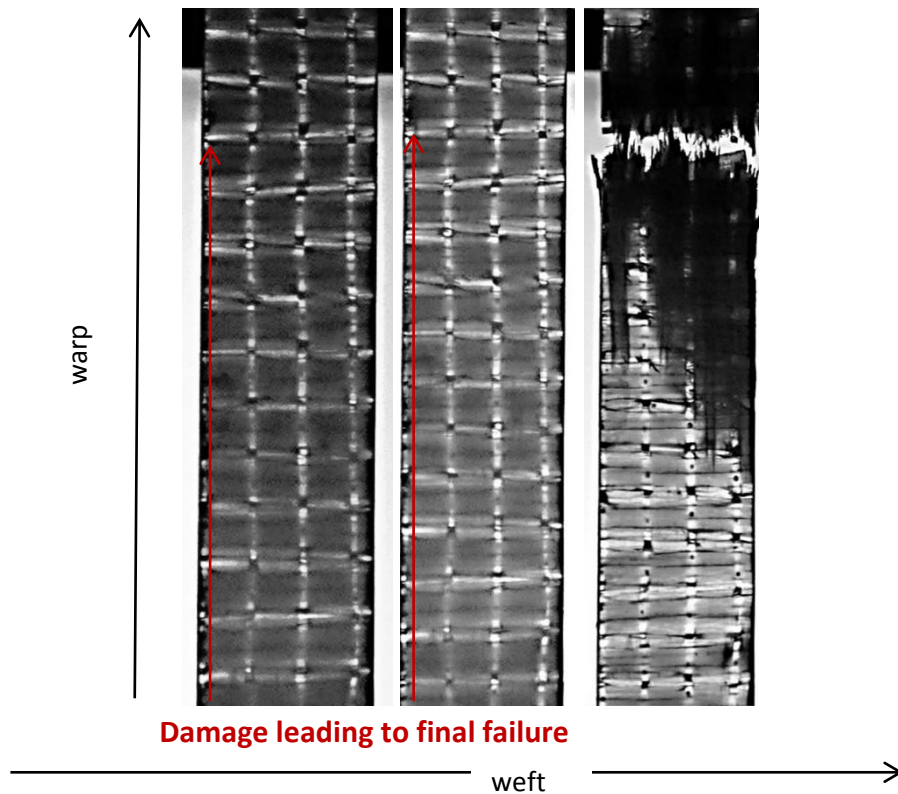


**Figure 4.4** Damage development in 3D-96 composite loaded in warp direction. Damage formation that brings to final failure has been captured into these transmitting light photos. Correspondent strain level is 2.64%.

It should be pointed out that final failure often occurred, as in this case, at a distance from the top grip less than than the width of the specimen. This region can therefore be considered influenced by the proximity with the grips, and the concentration of stress present might have caused premature failure.

Apparently, two types of cracks can be observed in the specimens. Vadlamani et al. (2011) distinguished between straight cracks and wavier cracks. The apparently wavy nature of the latter is due to the fact that cracks can grow in different through-thickness layers of the specimen at roughly the same location.

### 4.3 Response of the material tested in the weft direction

The following Figure 4.5 represents a typical stress-strain curve obtained testing the specimen into the weft direction.

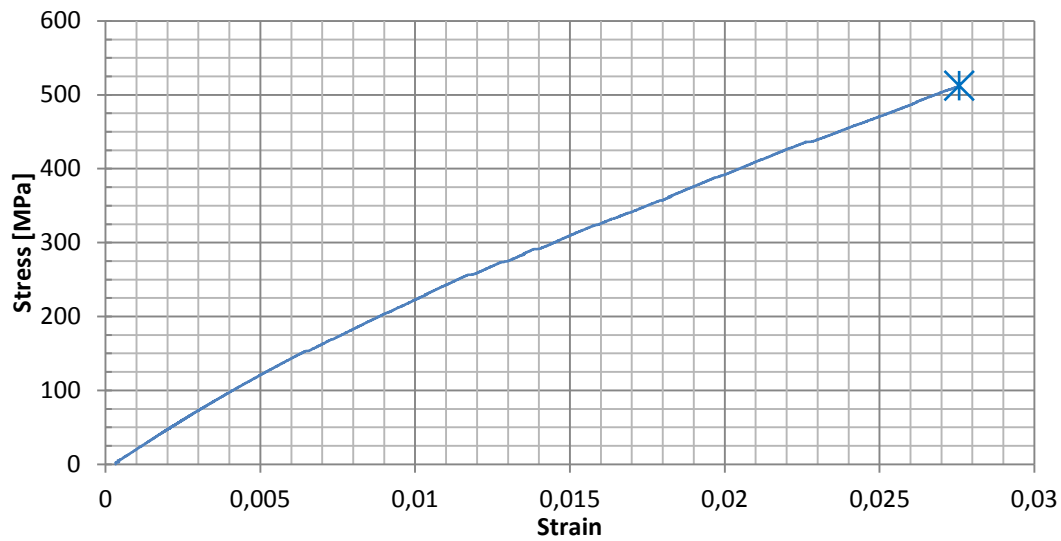


**Figure 4.5** Stress-strain curve of a specimen tested in weft direction

The pattern shown by the curve is similar to the one observed for specimen tested in the warp direction. Initially the curve is linear, until a strain level of about 0.25% is reached. After that, the curve is linear, but with a lower slope. At a strain level of about 0.6% the curve registers a first irregularity in the trend, corresponding to a value of stress equal to 160 MPa. After that, the curve continues in a continuous repeat of changes of slopes as a consequence of the damage development in the specimen. As the strain of 2.75% was reached, the specimen finally failed at a stress of 512 MPa.

Young's modulus ( $E$ ), ultimate tensile strength (UTS) and measured strain to failure are reported in Table 4.3. The Young's modulus values are calculated as abovementioned, considering the strain range of 0.05 % -0.2%.

**Table 4.3** Test results: mechanical properties

Specimen	Ultimate Tensile Strength [MPa]	Ultimate Tensile Strain	Young's Modulus E [GPa]
1	509,2	0,0253	30,1
2	512,1	0,0275	26,8
3	478,5	0,025	27,1
4	469,8	0,0251	27,5
<b>Average values</b>			
	492,4	0,025	27,8
<b>Standard Deviation</b>			
	21	0,001	1,5

In the following table 4.4, the results obtained are compared with the ones present in literature reported by Lomov et al. (2009)

**Table 4.4** Comparison between test results and mechanical properties present in literature.

Ultimate Tensile Strength [MPa]		Strain to failure [%]		Young's Modulus E [GPa]	
Lomov et alii		Lomov et alii		Lomov et alii	
486±5	492±21	3.33±0.27	2.57±0.12	25.1±2.3	27.9±1.5

In the case of specimen tested in the weft direction, again some differences are present. Average UTS measured is similar to the value of Lomov et al, but average Young's modulus value is 11% higher, with a 23% lower strain to failure.

Cracks began to form in correspondence of the z reinforcements, in proximity to the Z-crowns, growing in length along the warp direction. Similar initial damage has been observed and described also by Lomov. Through the use of the micrographs, he has localized these kind of cracks being inside the warp yarn or a the warp yarn/matrix interface.

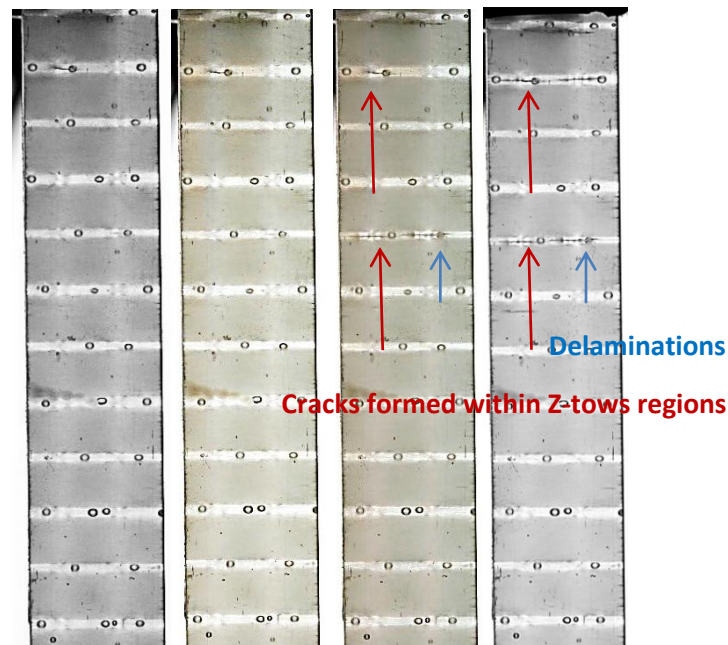


**Figure 4.6** Damage development in 3D- 96 composite loaded in weft direction. Formation of cracks in correspondence of a Z-tows (indicated by arrows) is reported in transmitted light photos. These are taken respectively in correspondence of 0.84%, 0.88%, 0.97% and 1.01% strain levels.



Where cracks are already formed, in the zones near the crossover between Z reinforcements and underlying weft tows, micro-delaminations seem to occur. They are recognizable in Figure 4.6 as little dark triangles developed from the cracks before formed. These cracks are not the only ones to form, as other smaller cracks start to form both from the edges and in the central zone of the specimen, as depicted in Figure 4.8. The latter form in the areas occupied by warp tows, in a plane orthogonal to the loading direction. Initially they multiply in number but not in length, developing across the entire breadth of the warp tows.

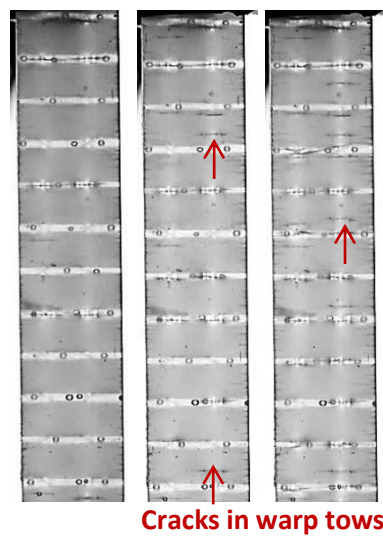


**Figure 4.7** Damage development in 3D- 96 composite loaded in weft direction. Formation of cracks in correspondence of warp tows (indicated by arrows) is reported in transmitted light photos. These are taken respectively in correspondence of 1.13%, 1.27% and 1.45% strain levels.

In addition to the cracks in the Z-tows, the cracks which also formed in the zones occupied by warp tows increased rapidly in number and length. Before final failure occurs, the specimen appears completely saturated by cracks.



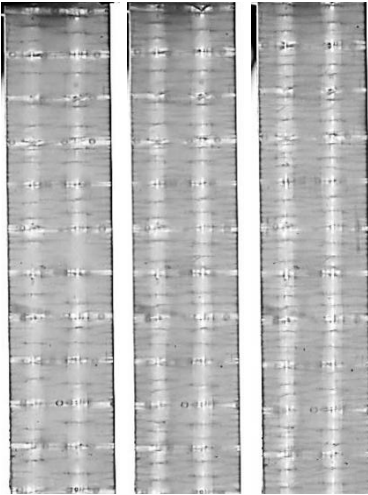


**Figure 4.8** Damage development in 3D- 96 composite loaded in weft direction. Accumulation of matrix cracks in correspondence of warp tows before final failure is reported in transmitted light photos. These are taken respectively in correspondence of 1.86%, 2.26% and 2.72% strain levels.

### 4.4 Comparison between warp and weft direction

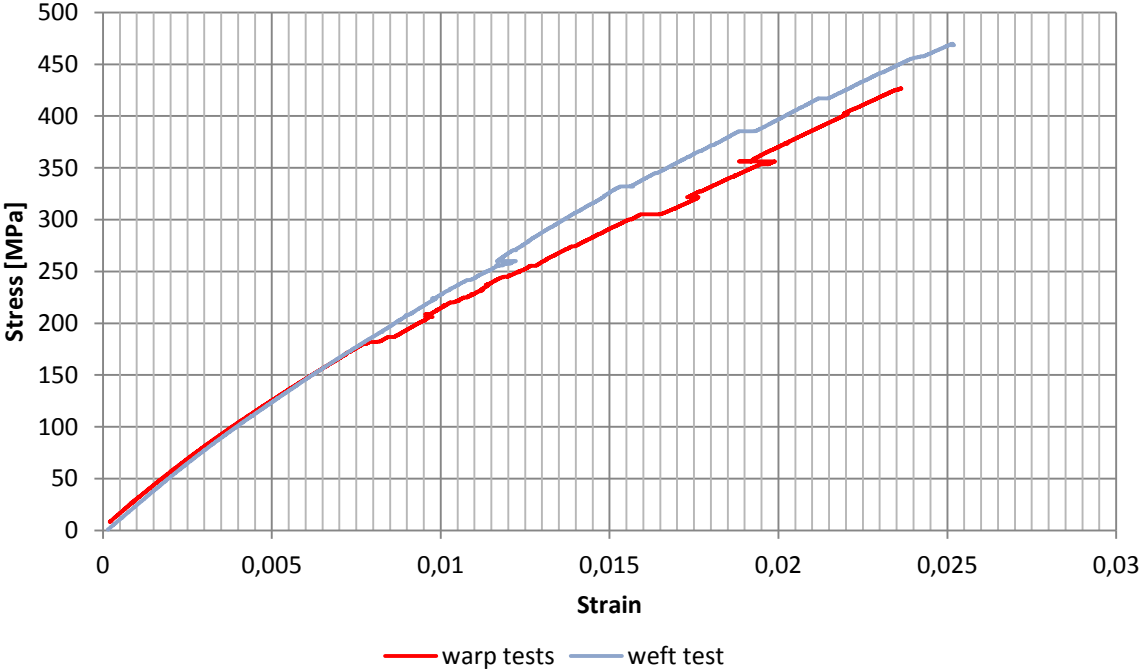


**Figure 4.9.** Typical stress strain curves obtained for warp test and weft test

The simultaneous representation of two typical stress- strain curves for the warp and weft directions is shown in Figure 4.9. This permits to compare easily the behaviour of the material

tested in both direction. Even if the pattern described by the two curves is similar, showing firstly a linear trend followed by repeated irregularities, a first difference to be noticed is represented by the slope of the first linear part. As it is note, it represents the Young's modulus. Specimen tested in weft direction have a higher modulus, characterized by a steeper slope. Another difference which has been encountered is the presence of the first knee in the curves that characterizes the onset of damage. Irregularities in the stress-strain curves are recently have been proved by Ashton, Poole and Ogin (2014) to be caused as a consequence of cracks forming asymmetrically with respect to the location of the extensometer – i.e. when more cracks form near the face where the extensometer is located, this gives an irregularity in the stress-strain response.

For the specimens tested in warp direction it was located between strain values of about 0.15-0.2, while for specimens tested in weft direction was between 0.0020-0.0025. In addition it can be seen that the final failure occurs that the final failure occurs at a higher strain value for specimen tested in fill direction (in the two cases shown in the figure, the strains are for weft and warp respectively, 2.76% and 2.64%).

**Table 4.5** Comparison of mechanical properties resulting from tests carried out in warp and weft directions.

Ultimate Tensile Strength [MPa]		Strain to failure [%]		Young's Modulus E [GPa]	
warp	weft	warp	weft	warp	weft
470±34	492±21	2.54±0.33	2.57±0.12	26.2±1.3	27.9±1.5

Table 4.5 shows the summary of the results obtained from the quasi static tensile tests in both directions. The average value of UTS obtained in the weft direction is ~5% higher than the UTS in the warp direction. Also, the average strain to failure is higher for the weft direction, but the difference is limited to ~1%. As was mentioned before, the specimens exhibited a higher stiffness when tested in the weft direction. The evident lower strength and stiffness values which characterize the warp direction has been explained from Lomov et al. as the consequence of the fact that warp tows are more damaged during the weaving process of fabric production. The amount of defects/damage imparted to fibers oriented in the warp direction would accelerate the final failure of specimens.

## **4.5 Concluding remarks**

In this chapter the results obtained from quasi-static tensile tests performed in warp and weft directions have been presented. Firstly each direction has been treated separately, describing the trend of a typical stress-strain curve, the mechanical properties measured (Young's modulus, ultimate tensile strength and strain to failure) and the damage development taken over transmitted light images taken during the tests. The mechanical properties measured have furthermore been compared with values in the literature, underlining the differences present and the reason of their presence. Then, the properties and the patterns of the curves obtained for warp and weft tests have been compared, revealing higher values of Young's modulus, ultimate tensile strength and strain to failure for specimens tested in the weft direction. The causes of the difference of behaviour has been suggested to be due to the introduction of defects/damage in the warp tows during the weaving process.

The next chapter will consider the response of the material to tensile fatigue tests. In particular, it will focus on the behaviour exhibited when tested at low stress levels.



# Chapter 5

## Tensile-tensile fatigue tests-low stress results

### 5.1 Introduction

From the stress-strain curves obtained with quasi-static tensile tests it is possible to divide the fatigue tests into two categories, distinguishing between tests carried out at low and high stress. These categories are based on the threshold stress for the initiation of matrix cracks, corresponding to the first irregularities recorded in the curve.

In this chapter, the results obtained from fatigue tests performed on warp direction specimens are presented for specimens cycled at different peak stress levels for 100'000 cycles at 5 Hz with an R-value of 0.1. After the mechanical investigation, the damage development was investigated through the use of images taken with optical and scanning electron microscopy. The aim of these tests was to investigate the relationship between the mechanical properties measured and the damage accumulation.

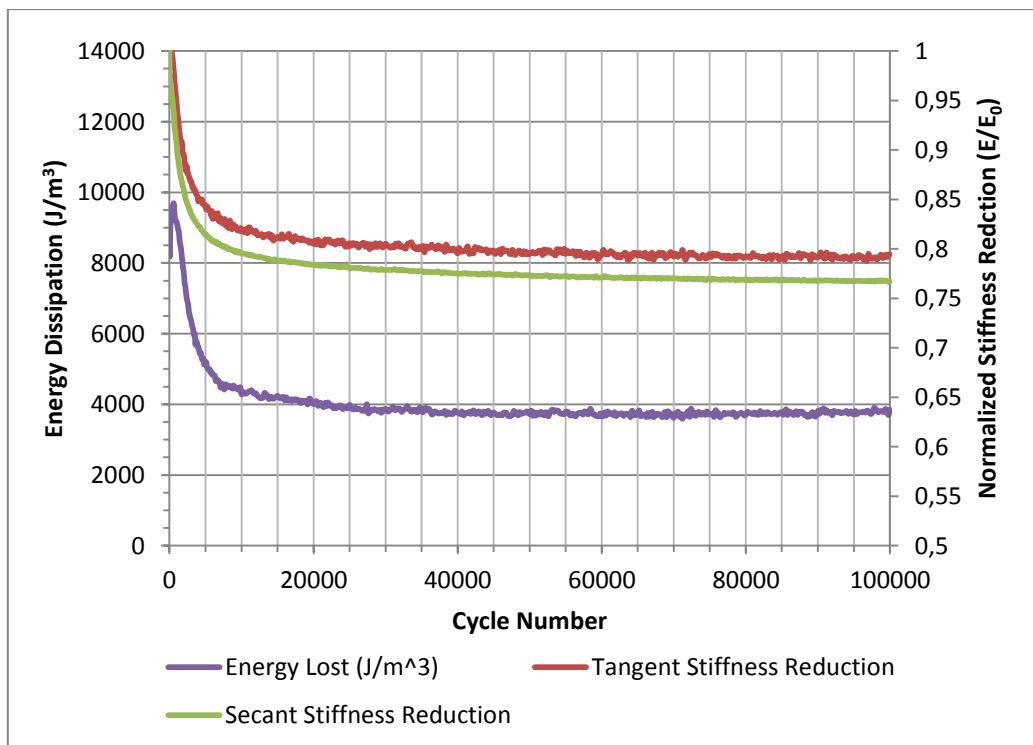
### 5.2 Mechanical investigation: energy dissipation and stiffness reduction

The results reported below show fatigue tests performed with peak stresses of 150 MPa, 100 MPa, 75 MPa and 50 MPa, which are all below the stress for onset of macroscopic damage in quasi-static test. In each graph, energy dissipated per cycle and stiffness reduction are reported. Energy has been calculated as the area enclosed by hysteresis loop drawn considering each cycle of loading and unloading. As the unloading curve in fact deviates from the loading one, the difference existing between the areas present under the two curves represent the energy that is lost through the loading/unloading cycle. Stiffness reduction has

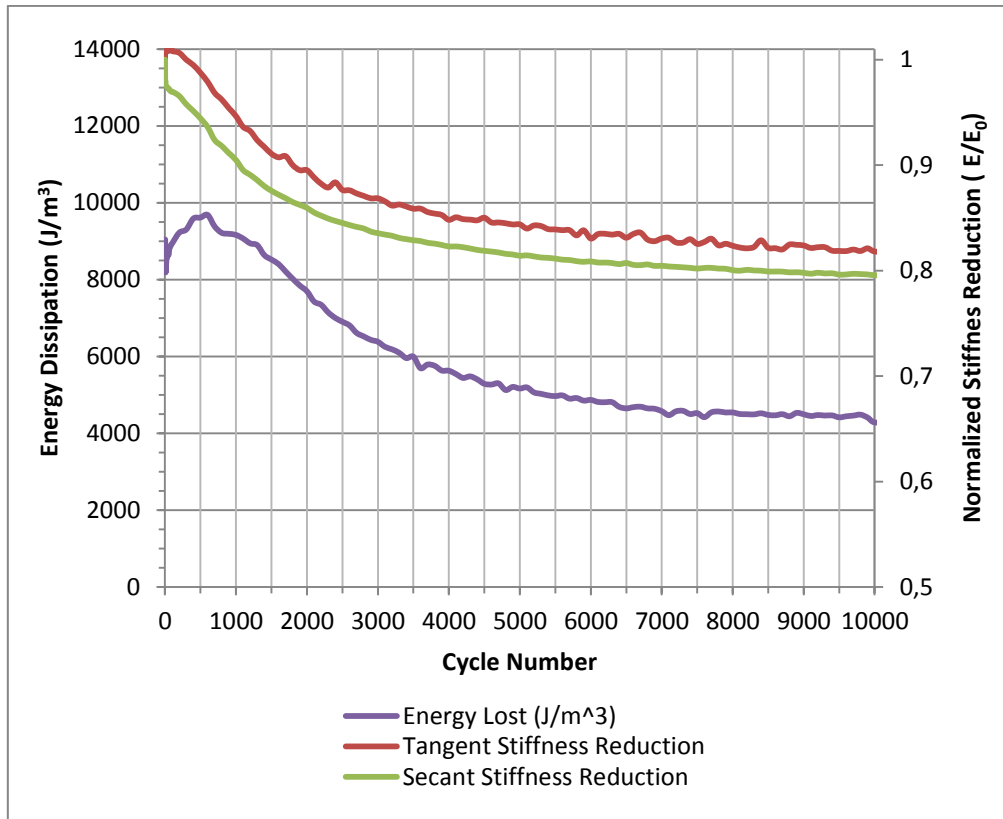
been calculated in two different methods. The first is referred to as *secant*. Stiffness is measured as the slope of the line passing through the minimum and maximum values of strain and stress recorded for every hysteresis cycle. The second is called *tangent* as only the first increasing part of the loading curve for each hysteresis loop is considered

Firstly each stress level is considered separately where stiffness reduction and energy dissipation are represented in the same graph. Then the curves of energy and of stiffness reduction for all the peak stresses are collected into two distinct figures, for comparison

### 5.2.1 Fatigue at a peak stress of 150 MPa



a)



b)

**Figure 5.1** Energy dissipation and stiffness reduction (both secant and tangent moduli are shown for it). The peak stress is 150 MPa. a) Cycles zero to 100'000; b) cycles zero to 10'000.

Energy dissipated, as can be seen in Figures 5.1 a) and 5.1 b), showed an interesting pattern. High values were recorded in the first half thousand cycles, reaching a peak of about  $9600 \frac{J}{m^3}$  after 400 cycles. Successively in the next 6000 cycles, the energy dissipated per cycle decreased with a steep gradient for the first few hundred cycles, which then gradually reached a plateau value after about 7000 cycles at a constant level of around  $4500 \frac{J}{m^3}$ .

The stiffness reduction, measured by both the secant and tangent methods, showed some similarities. It should be noted, however, that the tangent curve assumed a noisier pattern, disturbing the reading of results and making the secant curve more useful to represent the stiffness reduction trend. Both curves recorded a continuous decrease present from the beginning. After a slight fall in the first 50 cycles, the slope of the curves sharply drop in the next 2000 cycles for then attenuating with the elapsing of the subsequent 5000 cycles. Finally,

at about 7000 cycles, the curves reached a value around 0.8 which was maintained stable for the remaining part of the test.

By observing the trend of energy dissipated and stiffness reduction, therefore, two different phases could be distinguished:

1. Firstly the energy dissipated per cycle rose rapidly to a maximum, after which it dropped at a similar rate to the stiffness;
2. The final step is the achieving and maintaining of a stable value for the energy dissipated per cycle at about the same number of cycles as the stiffness reduction curves.

### 5.2.2 Fatigue at a peak stress of 100 MPa

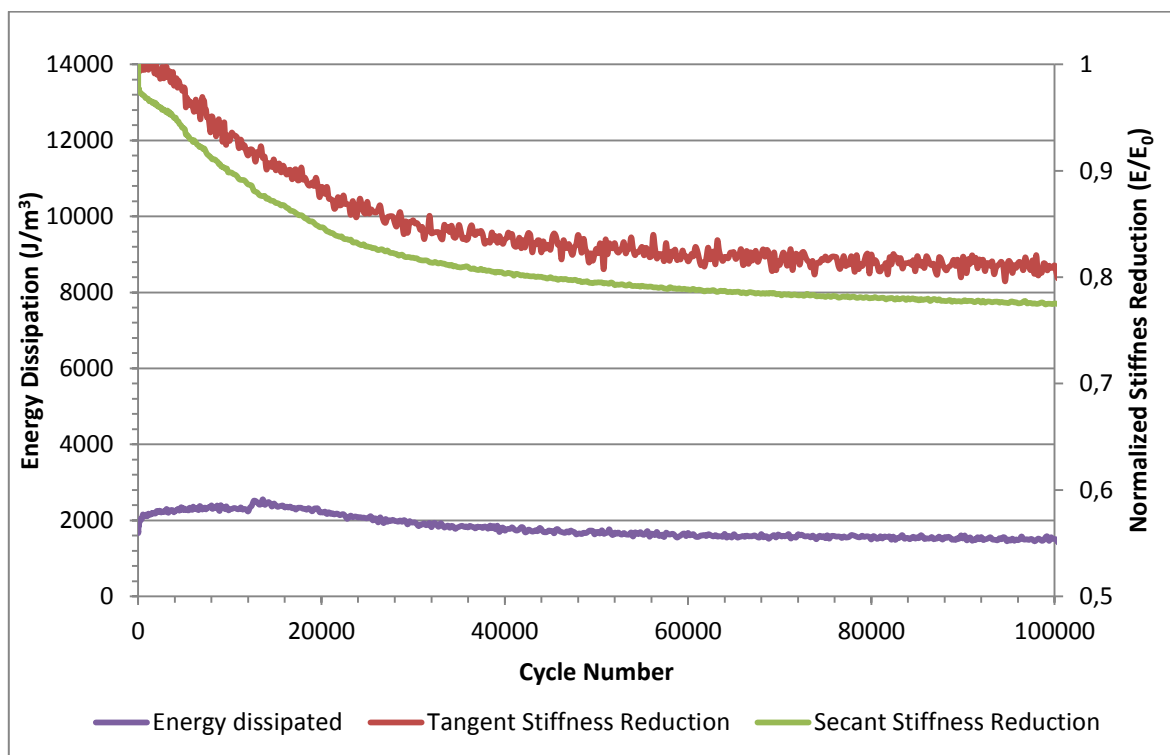


**Figure 5.2** Energy dissipation and stiffness reduction calculated considering either the secant or the tangent to hysteresis cycle. The peak stress imposed to the loading cycles is equal to 100MPa.



The recorded trend of energy dissipated and stiffness reduction is quite similar to the one observed for the test conducted with a peak stress of 150 MPa. The two different phases of increase, decrease and achievement of a constant level, in fact, are still present, with the difference that the lower stresses delay the entire process. The maximum energy dissipated per cycle reached after 10000 cycles, was about  $2500 \frac{J}{m^3}$ , while the constant level reached after 70000 cycles was around  $1500 \frac{J}{m^3}$ . For the normalized stiffness reduction, the first 1000 cycles were characterized by an insignificant loss of stiffness, followed by a rapid decrease amounting at 20%, that then attenuated until to reach a very small reduction rate at about 70000 cycles.

### 5.2.3 Fatigue at a peak stresses of 75 MPa and 50 MPa

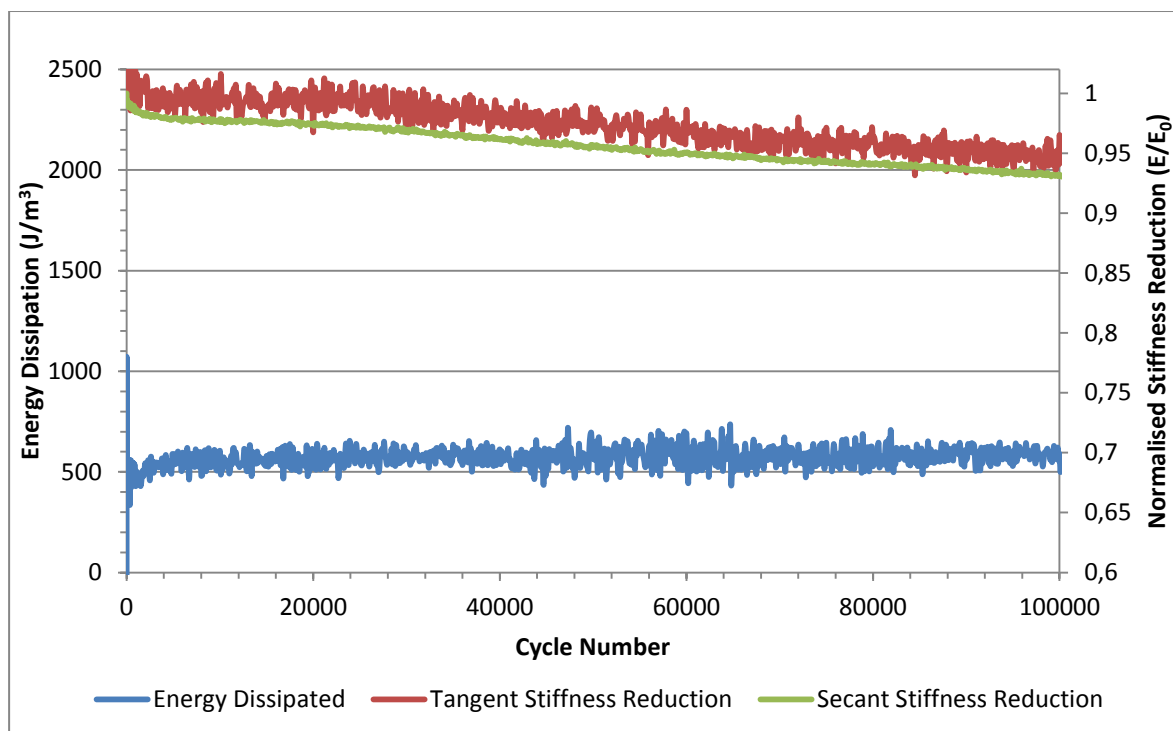


**Figure 5.3** Energy dissipation and stiffness reduction calculated considering either the secant or the tangent to hysteresis cycle. The peak stress imposed to the loading cycles is equal to 75MPa.

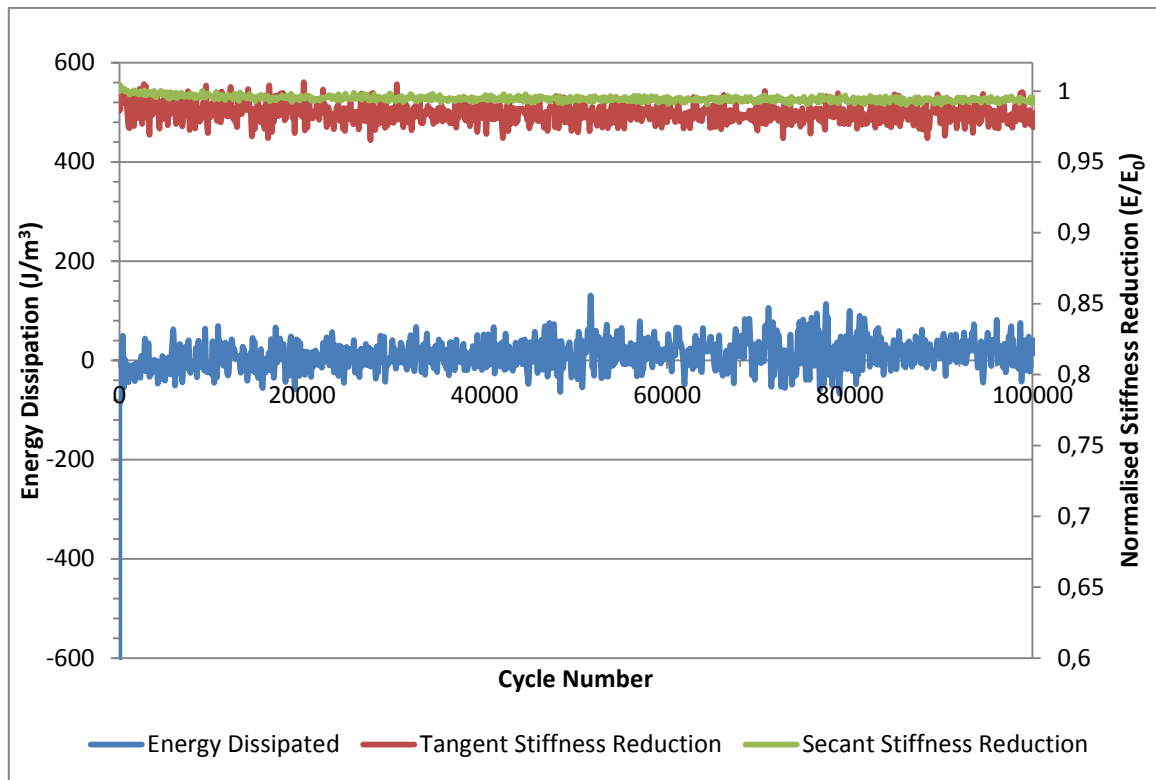


**Figure 5.4** Energy dissipation and stiffness reduction calculated considering either the secant or the tangent to hysteresis cycle. The peak stress imposed to the loading cycles is equal to 50MPa.

As Figure 5.3 shows, at 75 MPa the stiffness remained roughly constant around values of 1 and only started decreasing slowly after 20000 cycles, continuing until the test was stopped after 100'000 cycles. The result for the energy dissipated per cycle suggests that after an initial rapid increase, the energy dissipation increased very slowly up until about 10'000 cycles, and then maintained a constant value of about  $500 \frac{J}{m^3}$ .

The behaviour for 75 MPa can be compared with the one of both the stiffness reduction and energy dissipation at 50 MPa (Figure 5.4). The energy dissipated per cycle is almost zero, and there is also no stiffness reduction.

### 5.2.4 Comparison of fatigue behaviour for the warp direction at different peak stresses

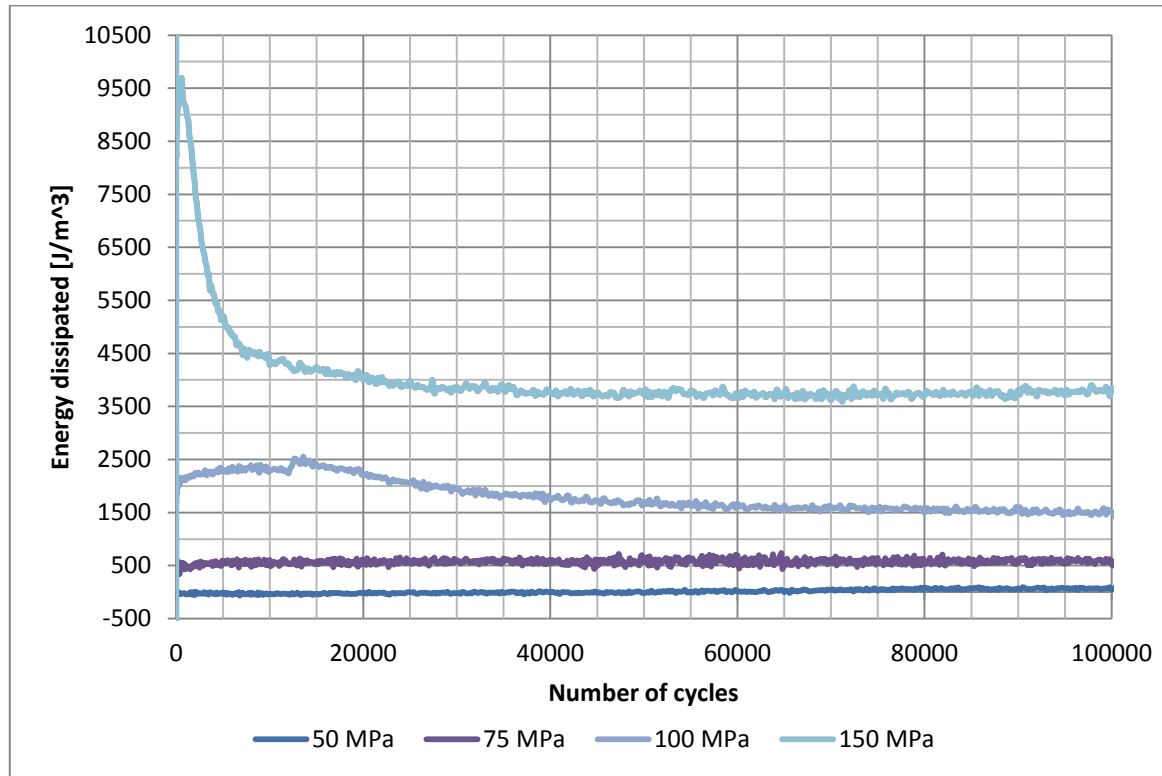


**Figure 5.5** Comparison of energy dissipated curves at peak stress levels of 50, 75, 100, 150 MPa

Figure 5.5 represents the gathering of the energy dissipated curves per cycle for the four different peak stress values. The behaviour falls into three groups: at 150 MPa and 100 MPa, a rise and a fall in the energy dissipated per cycle is clearly seen, at 75 MPa the energy dissipated per cycle is essentially constant at around  $500 \frac{J}{m^3}$  and at 50 MPa the energy dissipated is constant, but zero.

The stiffness reduction results also falls into the same three distinct groups. For 150 MPa and 100 MPa, the stiffness reduction shows two distinct phases, with a rapid loss in stiffness initially and a low, or even zero, stiffness reduction for the second phase. For the 75 MPa test, the stiffness falls at a constant rate, and at 50 MPa the stiffness does not fall at all.

The source of the stiffness reduction and energy dissipation is likely to be related to damage in the material and in the next section microscopy images will clarify the damage mechanisms detected in case of low stress fatigue tensile loading for the warp direction.

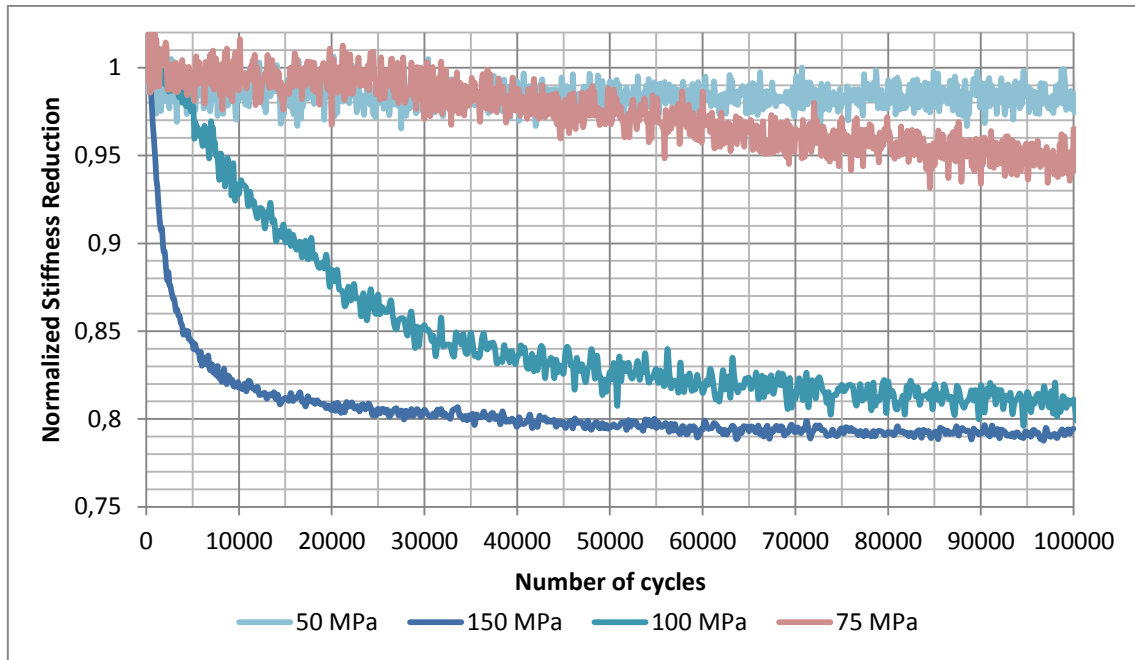


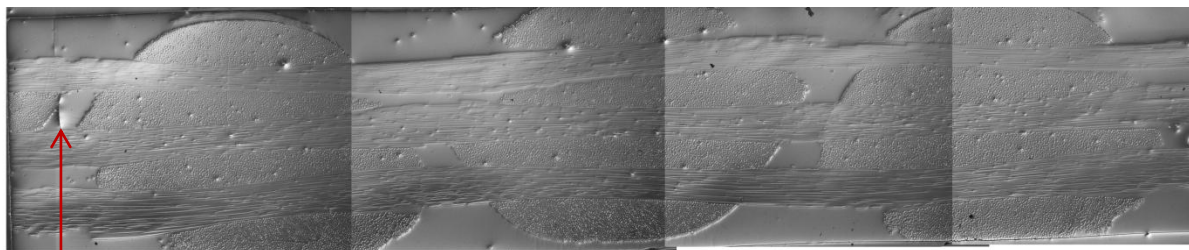
**Figure 5.6** Comparison of stiffness reduction curves at peak stress levels of 50, 75, 100, 150 MPa

### 5.3 Optical and scan electron microscopy investigation

Microscopy investigations were conducted on specimens tested at low stress with the aim of studying and understanding mechanisms involved in damage development.

The first specimen to be sectioned and examined had been tested to a peak stress of 50 MPa up to a number of cycles equal to 100000. The curves representing energy dissipation and stiffness reduction of the test have been already presented in the §5.2.

As it can be seen in figure 5.7, only occasional resin cracks were observable in the section under examination. This absence of damage could explain why there was no stiffness reduction or energy dissipation at this stress level.



**Resin crack**

1000  $\mu\text{m}$

**Figure 5.7** Optical micrograph images of specimen fatigue tested at a peak stress of 50 MPa.

For revealing further mechanisms of damage visible only at higher magnification, images have been taken from the same sample exploiting the advantages offered by scanning electron microscopy.

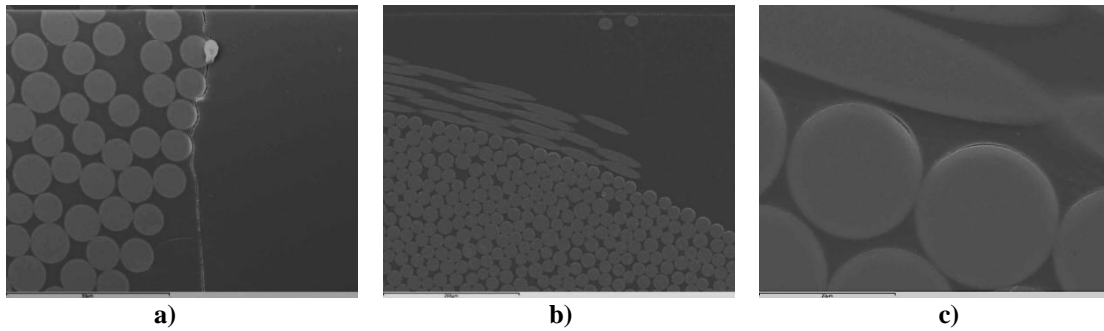


**Figure 5.8** SEM images of specimen fatigue tested at a peak stress of 50MPa.

The most significant outcomes are shown in Figure 5.8. The matrix crack already noticed in Figure 5.7 is shown in the first of the three images reported (Figure 5.8 a)). The crack seems to form starting from the joining up of the debonding of adjacent fibers. Aside from this damage, debonding between fibers and the surrounding matrix is the only other damage detected, occurring prevalently at the interface between z-tows and underlying weft tows (Figure 5.8 b) and c)). As similar damage was detected for untested specimens (see §3.4), it is not possible to determine if this damage was present from the beginning, or if it was formed during the loading cycles.

The second specimen sectioned and observed was from a fatigue test carried out with a peak stress of 75 MPa, again stopped after 100000 cycles.

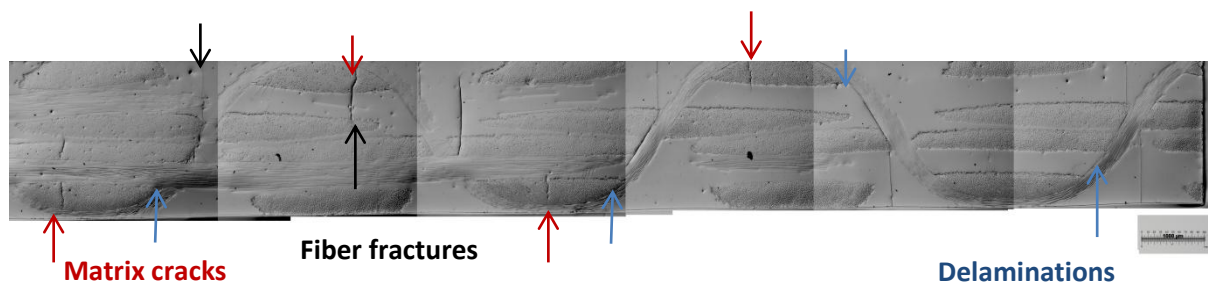


**Figure 5.9** Optical micrograph images of specimen fatigue tested at a peak stress of 75 MPa.

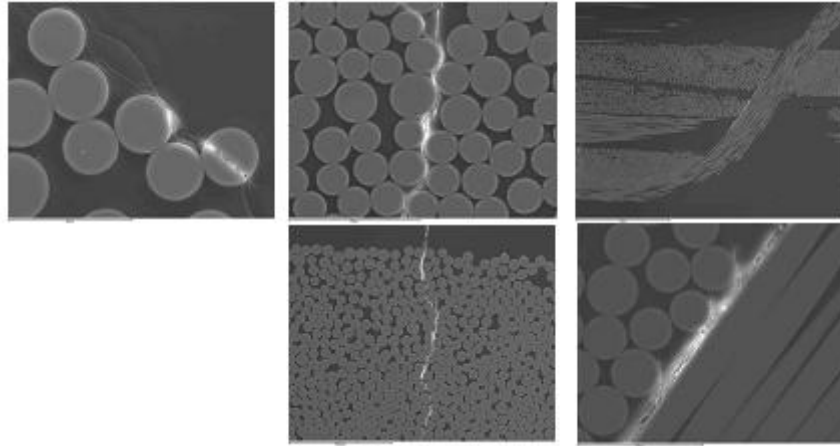


**Figure 5.10** SEM images of specimen fatigue tested at a peak stress of 75MPa.

By observing micrograph images shown in Figure 5.9 and Figure 5.10, it is possible to distinguish the following types of damage:

- Matrix cracks located close to the middle of surface weft tow, indicated with red arrows in Figure 5.9. It seems that they originate from the surface weft tow and then extend in the adjacent resin pockets that fill the gap between adjacent fill tows.
- Delaminations at the interface of Z tows and weft tows, indicated with blue arrows in Figure 5.9. Their length extends interesting the interface between the z reinforcement and resin pocket, for then deviating and giving birth to resin cracks. These develop along the direction orthogonal to the loading and their length grow until to reach the surface of the specimen.
- Occasional clusters of fiber fractures, indicated with black arrows in Figure 5.9, developed into external warp tows away from z-crowns as a consequence of the growth of the cracks present into resin pockets above mentioned.

The third specimen sectioned and observed was cycled with a maximum stress of 100 MPa, again for 100000 cycles. Optical micrograph images are shown in Figure 5.11. The plane of section was located next to a Z-tow and the Z-reinforcement did not appear in the micrograph, while were clearly visible the three warp tows. Despite the fact that Z reinforcement is not visible, the pattern of the nearest one (which is just out of this plane) is still discernible since it influences the position and the shape of weft tows.

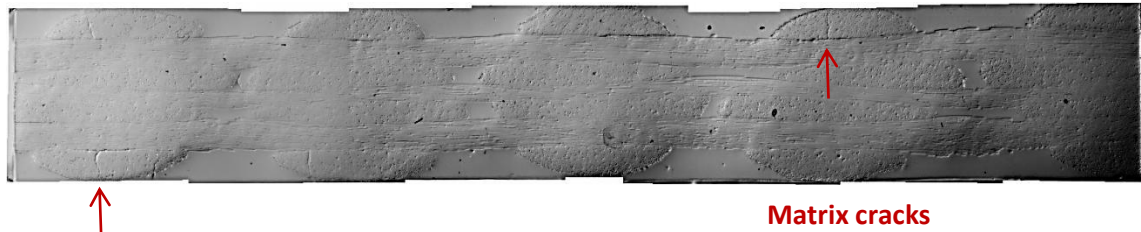


**Figure 5.11** Optical micrograph images of specimen fatigue tested at a peak stress of 100 MPa

In this micrograph, matrix cracks can be seen extending into external weft tows, which formed into micro-delaminations between the same weft tow and the underlying warp tow.

In an attempt to understand better the evolution of damage during a test, a new set of mechanical tests were performed. The maximum stress was kept at 150 MPa, while tests were stopped after a different number of cycles. The results are reported in the next section.

#### 5.4 Fatigue tests at 150 MPa, interrupted at different number of cycles

For these tests, the maximum stress was kept always equal to 150 MPa, while tests were stopped after a different number of cycles, each believed to be representative of a different phase of evolution damage based on the trend of the energy dissipation curve, reported in Figure 5.12. Then, specimens were sectioned and analysed through optical and scanning electron microscopy.

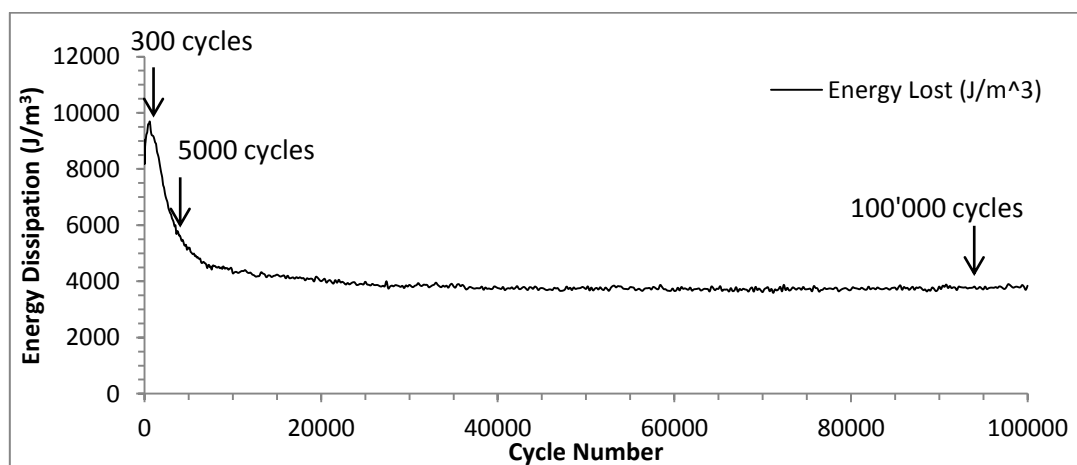
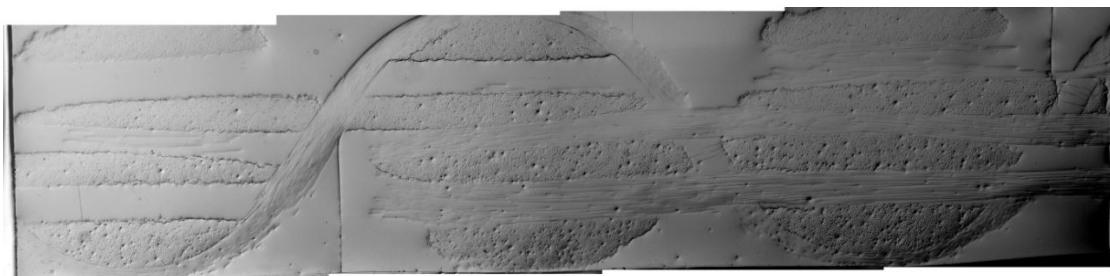


**Figure 5.12** Energy curve recorded for a test carried out with a peak stress of 150 MPa. Arrows indicate the number of cycles considered representative for each phase of increase, decrease and stabilization of energy.

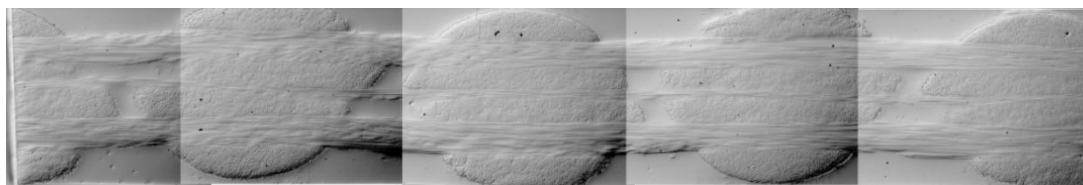
The first test was stopped after 300 cycles, in correspondence of the increasing part of the curve, before the peak of energy dissipation was reached. The second sample was stopped after 5000 cycles, after the maximum in the energy dissipation curve was overcome and the curve was decreasing. The final specimen was cycled for 100000 cycles, after a long period without apparent changes on the recorded energy curve.

#### *5.4.1 Test conducted with peak stress of 150 MPa stopped after 300 cycles*

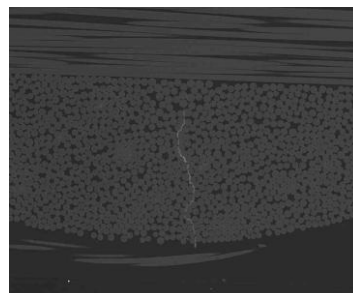
The first fatigue test carried out with a peak stress of 150 MPa was stopped just after 300 cycles, in correspondence of the peak of energy dissipation. Optical micrograph images and corresponding magnifications of areas of interest, taken by means of scanning electron microscopy, are shown in Figure 5.13.



1000 $\mu$ m



1000  $\mu$ m





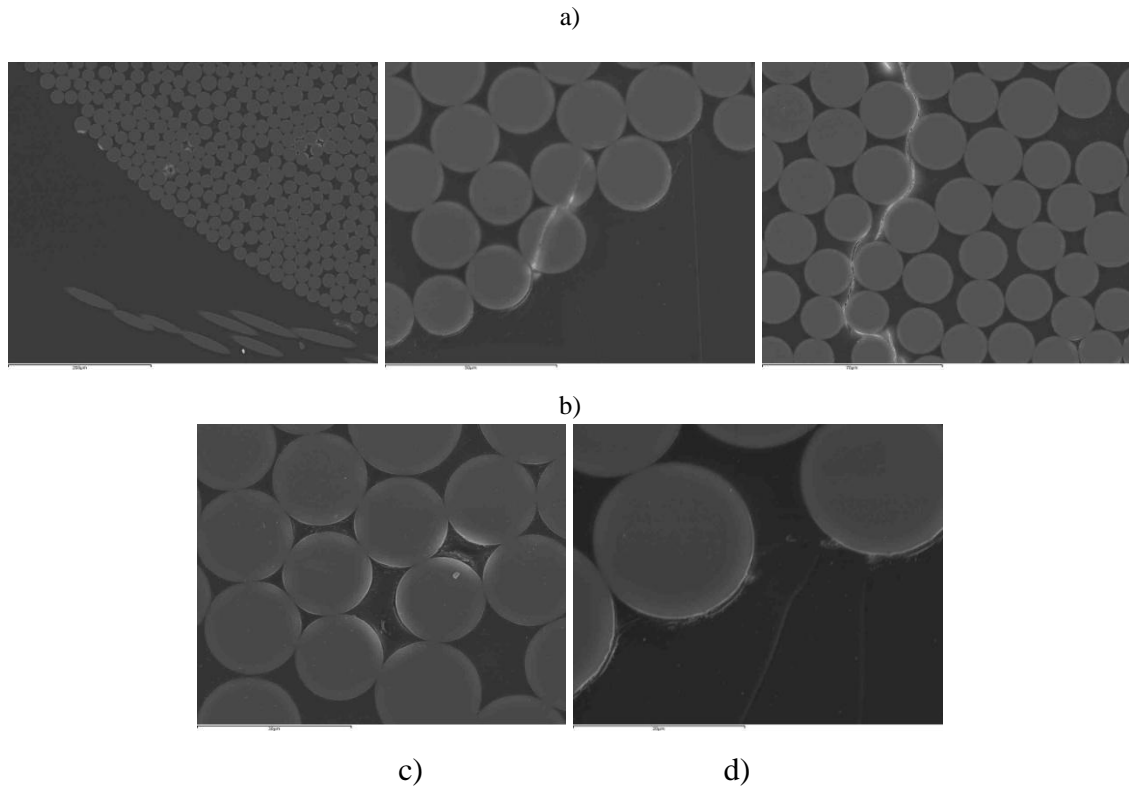


**Figure 5.13** Optical and SEM microscope images of the same specimen tested with a maximum stress of 150 MPa after 300 cycles.

Figure 5.13 a) shows a matrix crack in an external weft tow which extends from the location of the Z-tow through the weft tow towards the warp tow. This crack can be seen in more detail in Figure 5.13 b). Fibre/matrix debonding can also be seen in Figures 5.13 c) and d). It would appear, as is well-known, that the initiation of the first matrix cracks formation already originated from the cohesion of debonding of adjacent fibers; in this case, this appears to occur early in fatigue life, in outer weft tows, starting in the vicinity of the Z-crown and extending towards the underlying warp tow.

#### 5.4.2 Test conducted with peak stress of 150 MPa stopped after 5000 cycles

The second test carried out always at the same peak stress level was stopped after 5000 cycles, in correspondence of the final decreasing part of the energy curve. Optical micrograph images and corresponding magnifications of areas of interest of these, taken always by means of scanning electron microscopy, are shown in Figure 5.14.

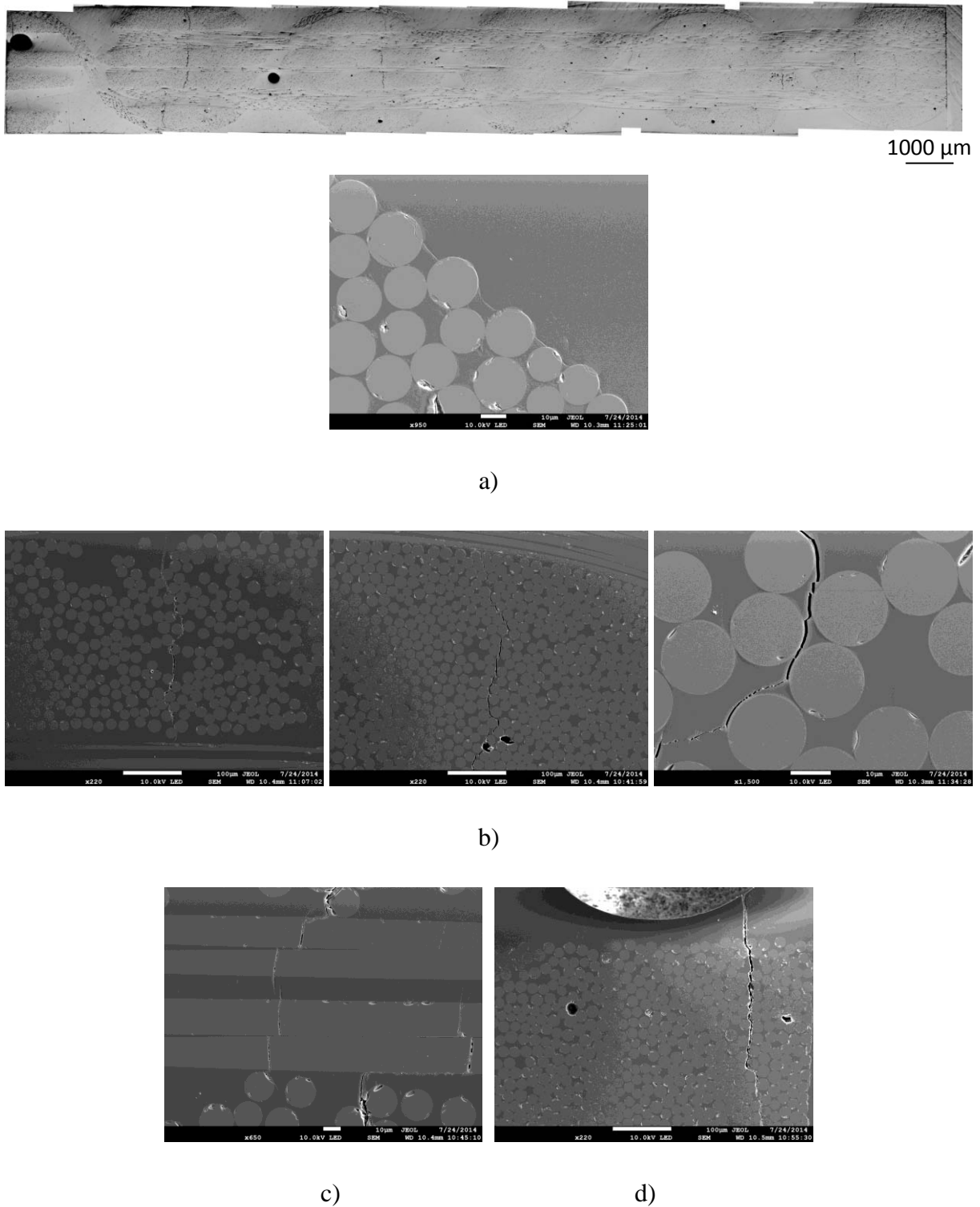


**Figure 5.14** Optical and SEM microscope images of the same specimen tested with a maximum stress of 150 MPa for 5000 cycles.

During the decreasing part of energy curves, microscope images have highlighted the extension of matrix cracks strating from the external weft tow growing across the adjacent

inner weft tow. Figure 5.14 a) shows the particular of a crack grown at the interface of the Z-tow with the weft tow, originated through the joining up of adjacent debonding fibers. Figures 5.14 b), instead, show the particulars of matrix cracks originated from outer weft tows and directed towards the underlying warp tow. The most interesting aspect is shown in Figure 5.14 c): through the use of SEM images, in fact, the presence of eventual clusters of fibers cracks into central warp tow was revealed. Their presence could be attributed to the fact that central tow, formed by a less number of fibers that makes it more prone to undergo damage, is surrounded by weft tows interested by matrix cracks, which may cause a stress concentration such to cause the initiation of isolated clusters of fibers orientated favourably to the loading direction.

Overall then, the images show a much higher degree of damage after 5000 cycles than after 300 cycles. Matrix cracks now appear in both the outer and in the inner weft tows. Furthermore, even at this early stage in the fatigue life of the specimen, there is evidence of warp tow fracture where weft tow matrix cracks meet the warp tows (probably because of the high stress concentrations at these locations).

#### 5.4.3 Test conducted with peak stress of 150 MPa stopped after 100000 cycles

The final test carried out at the same peak stress level was stopped after 100000 cycles; despite the elapse of numerous cycles, the energy dissipation curve had a stable value up to this point. Optical micrograph images and correspondent magnifications of areas of interest of these, taken always by means of scanning electron microscopy, are shown in Figure 5.16.



**Delaminations opposite to the Z-crown**

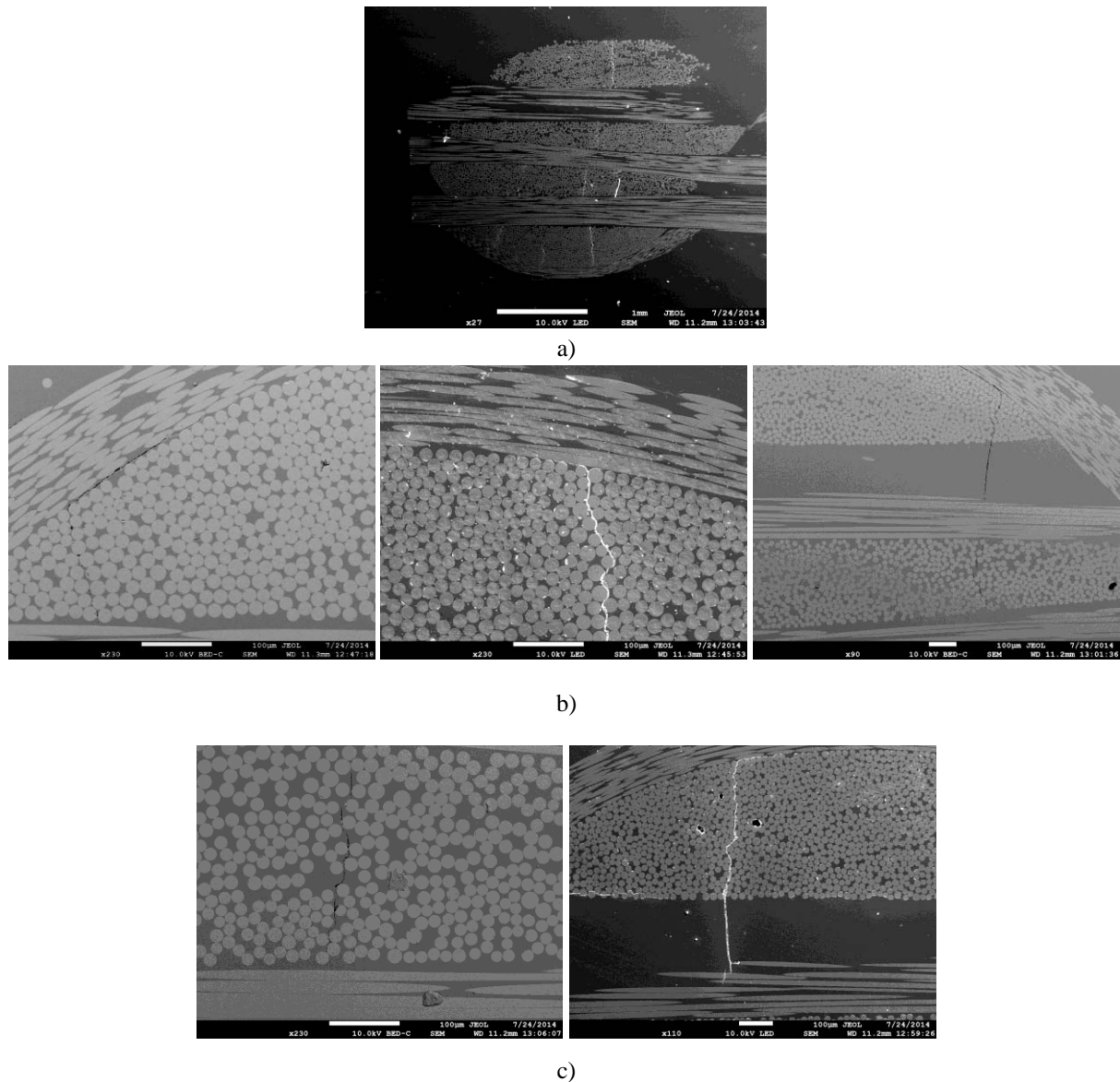


**Figure 5.15** Optical and SEM microscope images of the same specimen tested with a maximum stress of 150 MPa for 100000 cycles.

After the elapsing of 100000 cycles, matrix cracks were observable in all weft tows crossed over by Z-reinforcements, and the cracks usually extended through the entire height of the weft tows, located next to both the sides of the z-crowns, as shown in detail in Figure 5.16 a). These cracks also often extended across inner weft tows and eventually through the opposite external weft tow, developing along the whole thickness of the specimen. Figures 5.16 c), instead, show that the matrix cracks can eventually grow across the adjacent resin rich regions present between two warp tows, and then cause the fracture of the nearest warp tow. Microdelaminations associated with the matrix cracks were also often seen at the interface

shared between the weft and the Z-tows, as shown in Figure 5.16 b). In addition some delaminations were seen extending from matrix cracks at the interface between weft tow cracks and warp tows, as indicated by the arrow in Figure 5.16.

## 5.5 Concluding remarks

In this chapter, results of fatigue tests carried out with maximum stresses lower than threshold for the onset of macroscopic matrix cracking in a quasi-static tensile test have been presented. First, specimens were cycled with peak stress values equal to 50, 75, 100 and 150 MPa for 100000 cycles.

The energy dissipation curve shows a peak after the first cycles for the higher peak stress levels (100 and 150 MPa), then falls to a plateau value. The peak, however, was not present for energy curves obtained for lower peak stress tests (75 and 50 MPa). Stiffness reduction curves showed a continuous decreasing trend, with an accelerated rate at the stresses in the early part of the test and a constant reduction for the test at 75 MPa. Energy dissipation was negligible, as was the stiffness reduction at 50 MPa.

To investigate the connection existing between the trend of curves and damage origin and accumulation, optical microscopy images were taken a) corresponding to the same number of cycles at different peak stresses and b) corresponding to different number of cycles for the same peak stress level; microscopical observations have revealed the existence of different types of damage, including fibre/matrix debonding, microdelaminations at weft tow/Z-tow interfaces, delaminations at weft tow/warp tow interfaces and clusters of fibre fractures where matrix cracks intersect with warp tows.

In the next chapter results will be presented obtained from tensile-tensile fatigue tests performed with higher maximum stress values, while damage investigation will be carried out through the combination of microscopy and micro-computed tomography.



# Chapter 6

## Tensile-tensile fatigue tests – high stress results

### 6.1 Introduction

The present chapter will report and discuss results of fatigue tensile tests conducted on specimens loaded, differently from the previous chapter, with maximum stress values higher than the threshold of initiation of matrix cracking in a quasi-static test. Since specimens were loaded along both warp and weft directions, the structure of the chapter will be divided into two separate sections, dedicated to the results presentation of each direction. S N curve representation will be followed by a mechanical investigation concerning the trend of energy dissipation and stiffness reduction.

### 6.2 Response of the material tested along warp direction

#### 6.2.1 S-N curve

Specimens cut out from different fabricated laminates have been fatigue tested, imposing a peak stress aging equal to 175 MPa, 200 MPa, 250 MPa, 300 MPa and 350 MPa, until final failure occurred. The collection of the number of cycles to failure vs maximum stress applied, made it possible permitted to draw the S-N curve, characteristic of this 3D material tested in the warp direction. Figure 6.1 shows the curve obtained with ordinates of the peak stress or the equivalent initial peak strain values applied (the peak strains have been obtained from the quasi-static tensile test curve of stress against strain). Since a number of quasi static tests were carried out, the values reported for peak strain in Table 6.1 are the arithmetic average, while standard deviations are reported in the next column.

Values of peak stress, peak strain and number of cycles to failure recorded for each fatigue test are instead reported into Table 6.1.

**Table 6.1** Peak strain, peak stress, number of cycles to failure of fatigue tests performed.

Peak Strain	Dev Std	Peak stress (MPa)	Number of cycles	Average	Dev Std
0,01672	0,0006	350	214	266,3	62
0,01672		350	353		
0,01672		350	232		
0,01378	0,0005	300	776	1430,7	544
0,01378		300	2109		
0,01378		300	1407		
0,01105	0,0004	250	4323	5993	4429
0,01105		250	12056		
0,01105		250	1600		
0,01105		250	3794		
0,01105		250	3456		
0,00838	0,0004	200	19089	31534	8928
0,00838		200	35908		
0,00838		200	39605		
0,00838		200	70911		
0,00719	0,0004	175	290420	208828	114809
0,00719		175	289600		
0,00719		175	46464		
0,00719		175	44024		

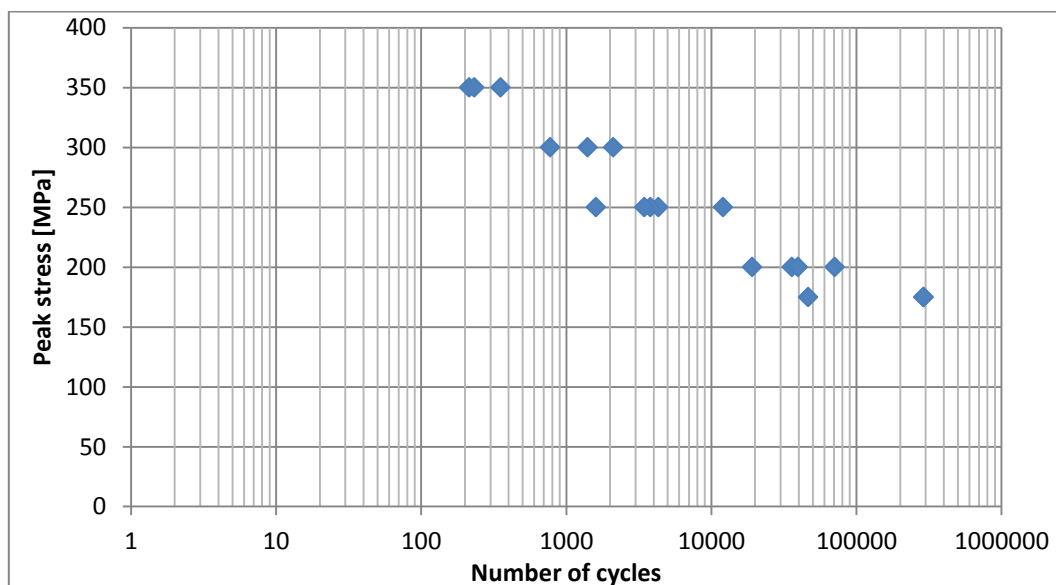


**Figure 6.1** S-N curve for specimens tested along warp direction: number of cycles are reported vs values of peak stress



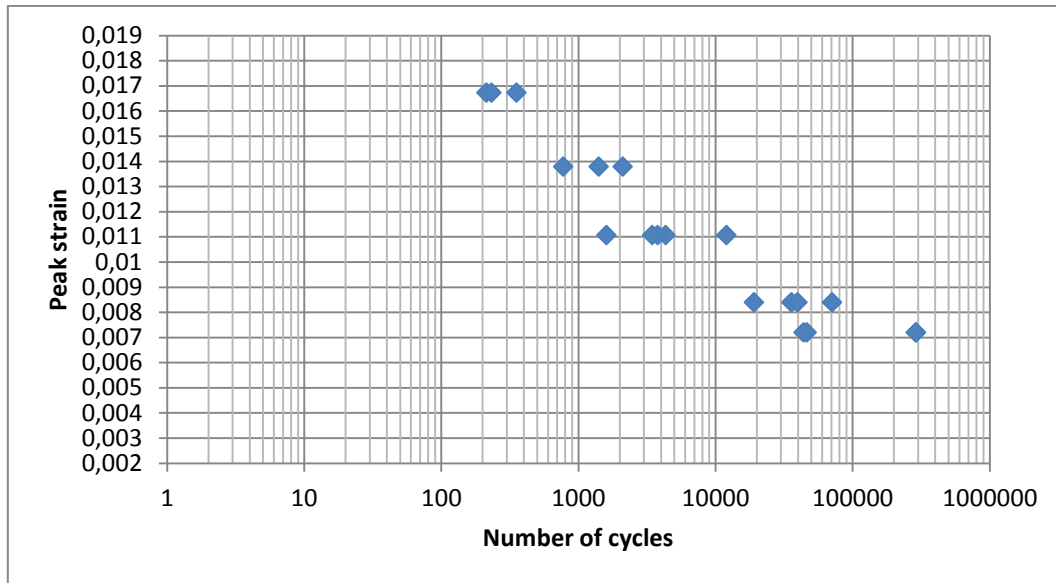


**Figure 6.2** *S-N curve for specimens tested parallel to the warp direction: number of cycles are reported vs values of peak strain*

The curve obtained was compared with S-N data present in literature. Carvelli et al., studied the fatigue behavior of a similar material, made with the same 3D- 96 fabric but embedded in a Dow Derakane 8084 Epoxy-Vinyl Ester resin and fabricated differently (using the VARTM technique). The two curves are illustrated in Figure 6.3.

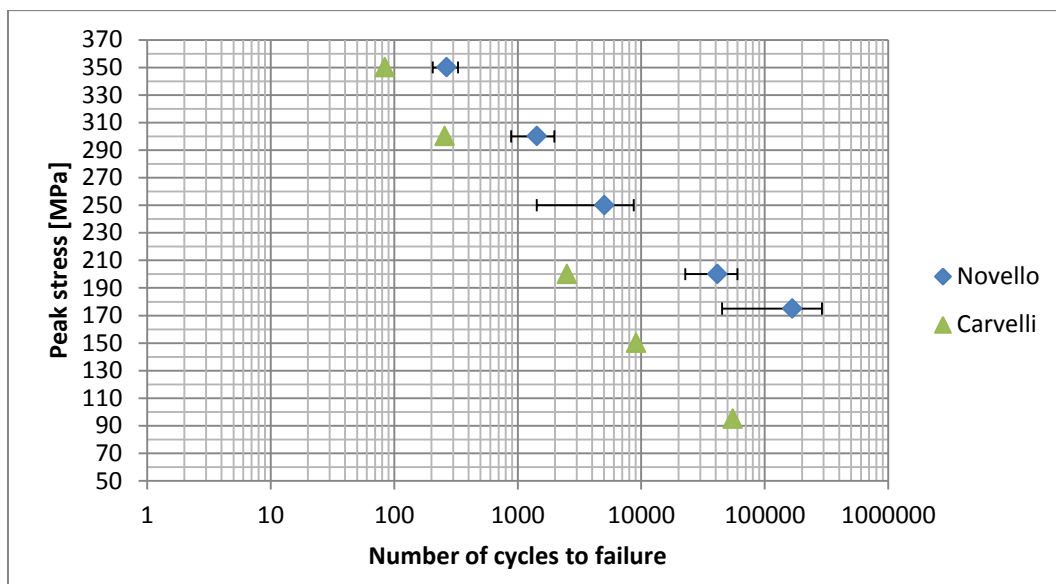


**Figure 6.3** *Comparison between S-N curve obtained from experimental work and S-N curve drawn from literature data (warp direction).*

The S-N curve obtained in this work is shifted towards longer fatigue life-time durations for the same peak stress levels imposed. This dissimilarity might be attributed mainly to the different type of resin used, to the VARTM fabrication method adopted, it is also possible that the larger width of the specimens tested by Carvelli et al. may have a role. An investigation on the influence exerted by the width will be given in §6.2.4.

### 6.2.2 Mechanical investigation: energy dissipation and stiffness reduction

Curves of energy dissipation and stiffness reduction per cycle were acquired for tests carried out with different peak stress values are reported as the following. All specimens have been tested until catastrophic failure occurred, while the use of an extensometer having a 96 mm gauge length permitted the recording of strains for the majority of the gauge length and the possibility of monitoring final failure (if this occurred between the extensometer knife edges). Occasional failure occurred within the gauge length of the extensometer, but most failures occurred near the grips where a stress concentration was present.

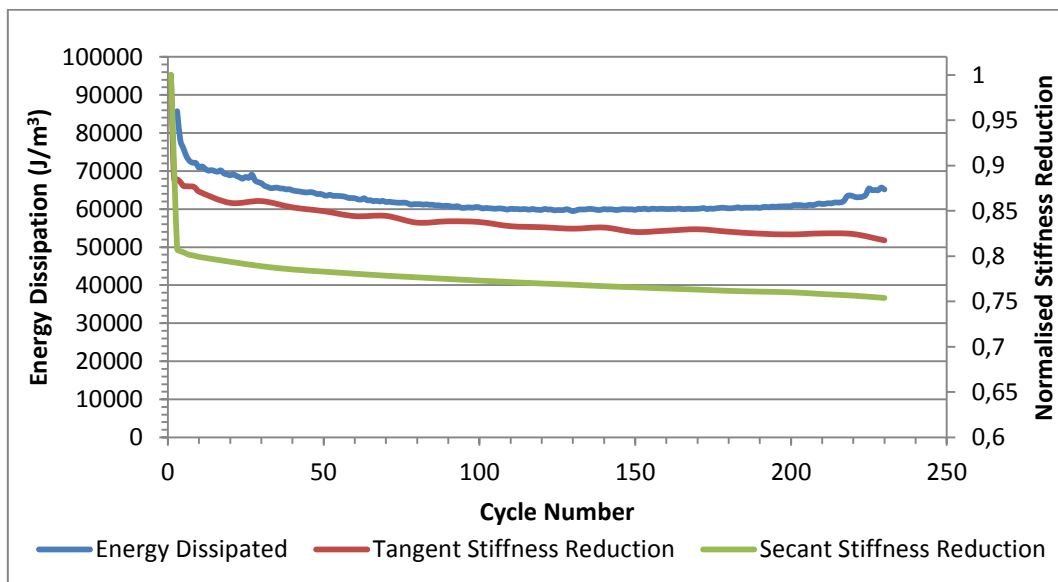


**Figure 6.4** Energy dissipation and stiffness reduction vs elapsed number of cycles for a test performed at a peak stress of 350 MPa. The specimen failed after 232 cycles in a region near the grips.

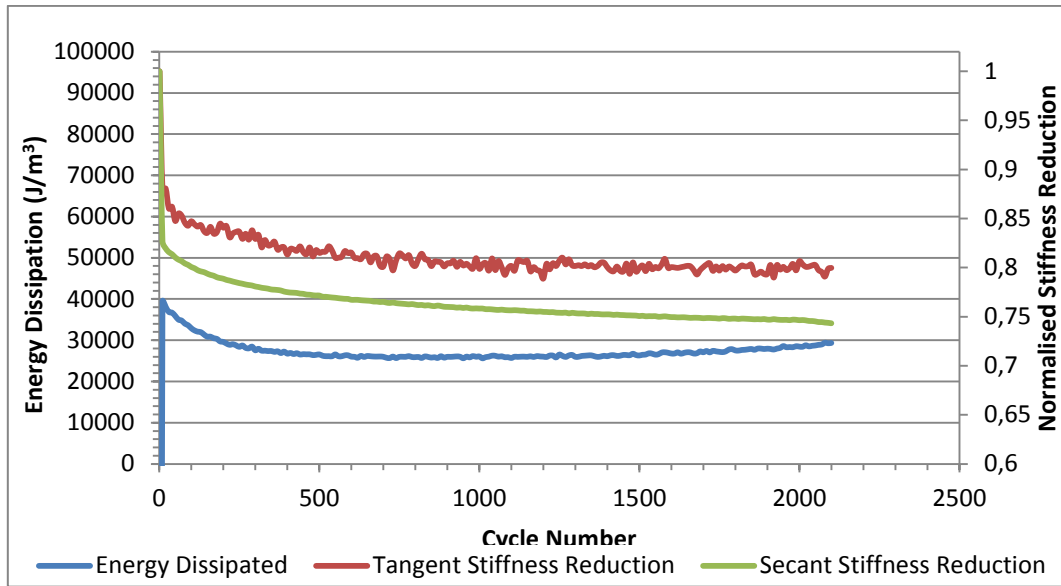


**Figure 6.5** Energy dissipation and stiffness reduction vs elapsed number of cycles for a test performed at a peak stress of 300 MPa. The specimen failed after 2109 cycles in a region near the grips.

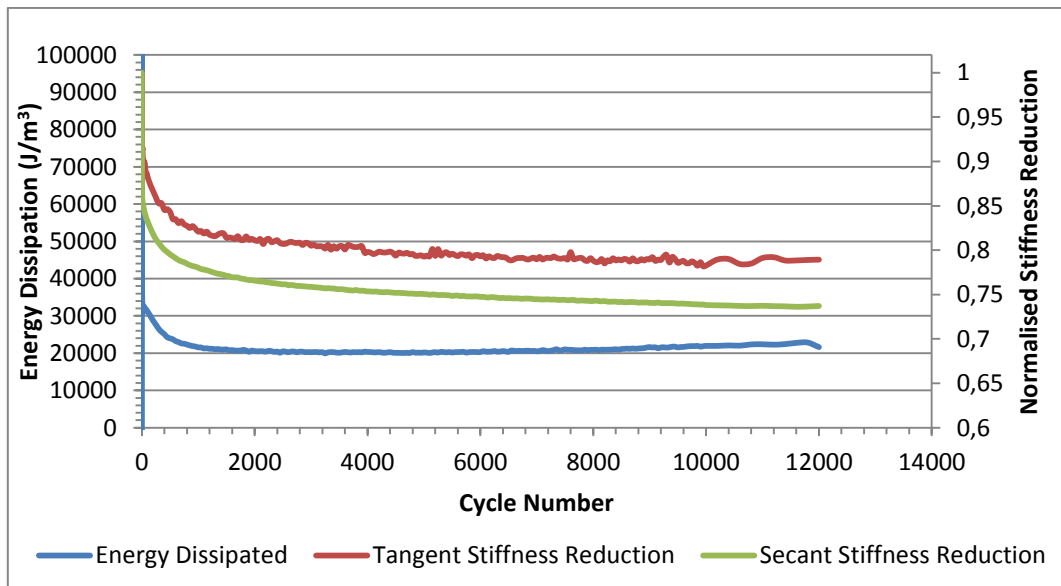


**Figure 6.6** Energy dissipation and stiffness reduction vs elapsed number of cycles for a test performed at a peak stress of 250 MPa. The specimen failed after 12056 cycles in a region near the grips.

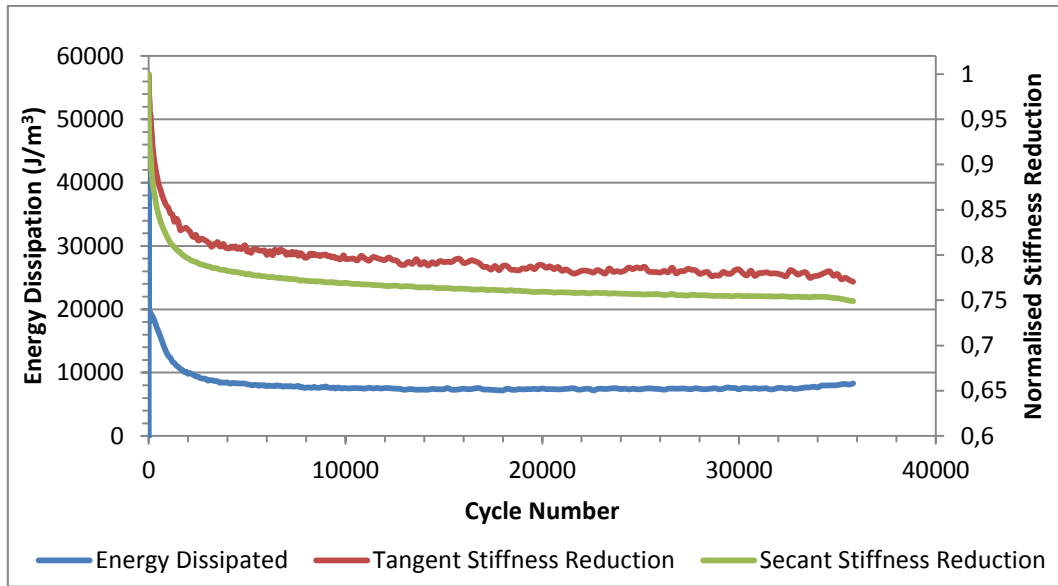


**Figure 6.7** Energy dissipation and stiffness reduction vs elapsed number of cycles for a test performed at a peak stress of 200 MPa. The specimen failed after 35200 cycles in a region near the grips.

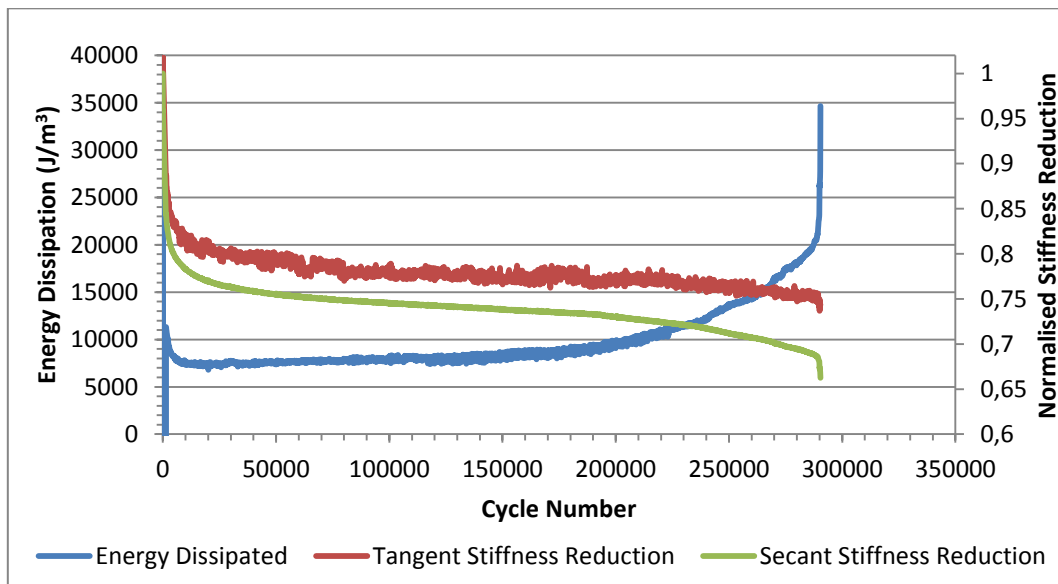


**Figure 6.8** Energy dissipation and stiffness reduction vs elapsed number of cycles for a test performed at a peak stress of 175 MPa. The specimen failed after 290400 cycles into the gauge region.

The comparison of Figures 6.4, 6.5, 6.6 and 6.7 (for peak stress levels of 350 MPa, 300 MPa, 250 MPa, 200 MPa and 175 MPa) permitted to observe the dramatic increase in the number of cycles to failure and decrease in the energy dissipation per cycle. Peak values of 80000 J/m<sup>3</sup> were reached into the first cycles with peak stress of 350 MPa, which then reduced to

stabilize around values of  $60000 \text{ J/m}^3$  reached in the plateau region. Tests carried out with 300 MPa, instead, registered a maximum value of about  $40000 \text{ J/m}^3$ , equal to half of the peak registered for the case of 350 MPa, while the energy dissipation plateau was established around values of  $26000 \text{ J/m}^3$ . The decrease of energy dissipation continued with the diminution of stress level, as the energy peak recorded for 250 MPa, 200 MPa and 175 MPa are respectively around 34000, 20000 and  $11000 \text{ J/m}^3$  while plateau values are of 20000 and  $7000 \text{ J/m}^3$ ; the latter value was common to both 200 and 175 MPa.

With regard to the stiffness, the recorded diminution did not change evidently with the variation of peak stress. Using the secant method, the measured stiffness preceding the ultimate failure was equal to 70-75% of the primary stiffness value, calculated for the first loading cycle, while considering the tangent method, stiffness resulted reduced to 80% compared to the first value.

The comparison of curves representing energy loss and stiffness degradation also highlights how the different possible locations of failure affected the trends.

When the failure occurred inside the extensometer gauge length, as in the case of Figure 6.7, three stages could be distinguished:

- i. First stage was characterized by a rapid stiffness reduction accompanied by a high corresponding energy dissipation per cycle;
- ii. Second stage presented a gradual stiffness degradation while energy dissipation showed a slow increase;
- iii. Third stage, which lead to ultimate failure, was marked by a renewed rapid stiffness reduction together with a large increase in energy dissipation, showing a trend rising in steps.

Audible noises of initial formation and accumulation of matrix cracks were heard in the first phase, while the second phase, thought to be associated with saturation of crack density, was silent. Noises resumed only during the third stage, when it is assumed fiber fractures occurred.

In cases where final failure occurred near end tabs, only two phases could be distinguished:

- i. First stage constituted into a rapid stiffness decrease associated with a high energy dissipation per cycle, similar to what already observed for specimens that were going to fail inside the extensometer gauge length;

- ii. Second stage presented the main differences in comparison with the respective stage abovementioned, since energy dissipation kept stable values, while stiffness reduction recorded a continuous gradual decrease. This stage continued to specimen failure, but this occurred without any evident changes to the trend of the curves.

### 6.2.3 Investigation of damage development

To inspect the late damage phase, preceding the ultimate failure of a specimen, a specific fatigue test was performed. A specimen was cycled until the energy curve started to rise, thus presenting the evidence of being at the beginning of the third stage of damage development, and then the test was stopped when audible fibre fractures were heard.

Figure 6.8 shows the trend of energy and normalized stiffness resulting from this test which was carried out with a maximum stress of 200 MPa and stopped after 14975 cycles had elapsed.

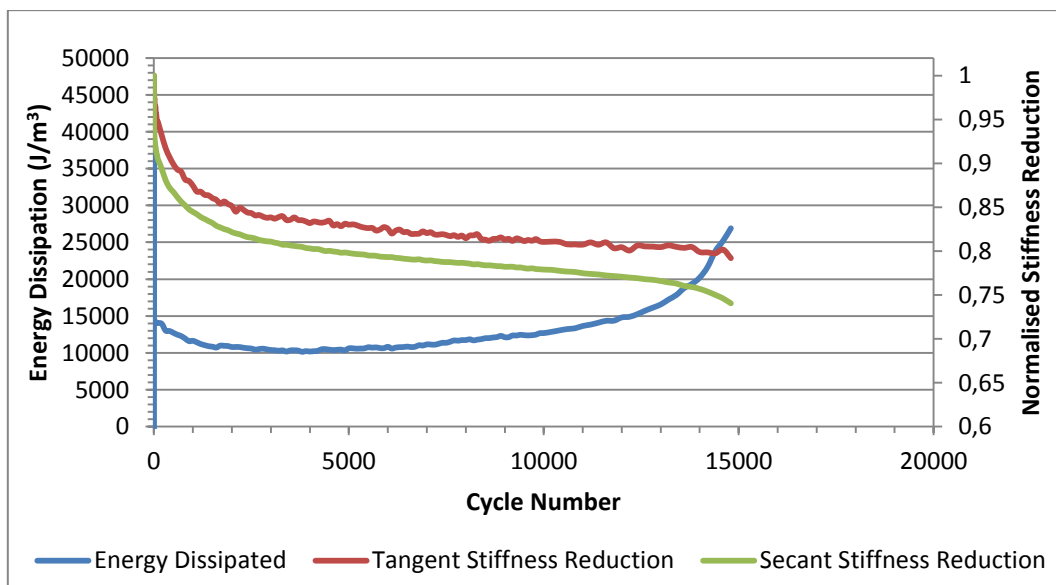


**Figure 6.9** Normalized stiffness reduction and energy dissipation with number of cycles for a specimen cycled with a peak stress of 200 MPa.

Observation of damage evolution in the specimen was then performed through a micro-computed tomography investigation at the Manchester X-ray Imaging Facility (MXIF). This technique required that only a small section of the specimen (corresponding to the size of a

single unit cell) could be observed for each analysis session, as the resolution had to be high enough to detect fibre fractures.

Figure 6.10. shows schematically the location of cross-sections which were investigated. X-ray  $\mu$ CT images are then reported in Figure 6.11.

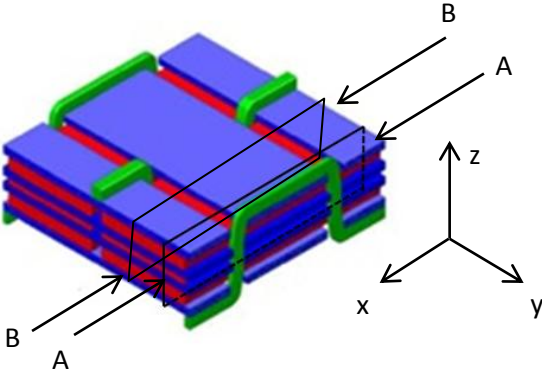


**Figure 6.10** Schematic exemplification of the specimen structure and axis convention used

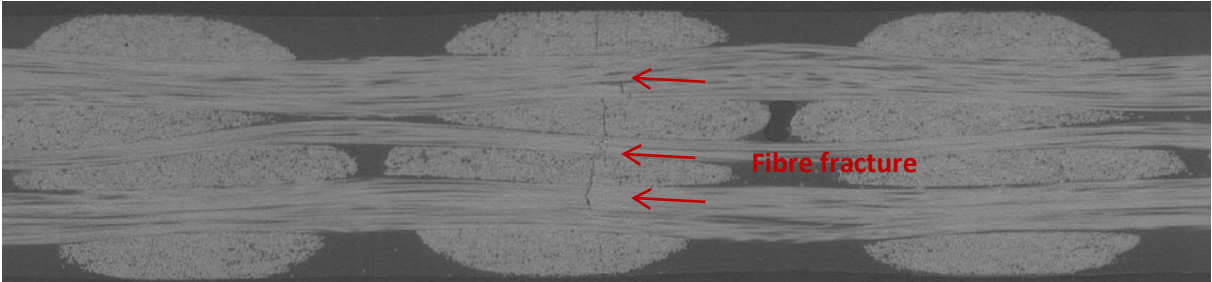


**Figure 6.11** CT section (A-A plane) showing extensive fibre fracture in the middle and low warp yarns

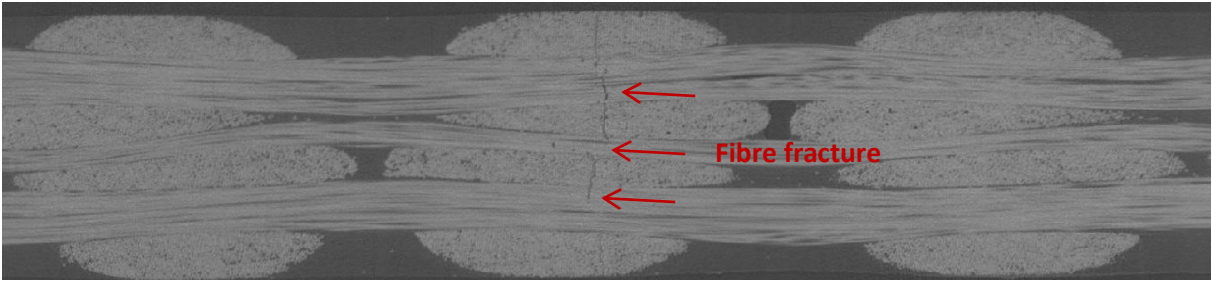


**Figure 6.12** CT section (B-B plane) showing extensive fibre fracture in the middle and low warp yarns

Figure 6.11 shows the A-A plane which is just adjacent to the edge of a Z-tow (as shown schematically in Figure 6.10). The figure shows the formation of fibre fractures in all three

warp tows, which seem to originate from the matrix cracks in the middle weft tows. Figure 6.12 shows the B-B plane, further than the A-A plane towards the centre of the warp tows. The figure shows the presence of fibre fractures in all the thickness of the warp tows, always surrounded by matrix cracks in the weft tows. The combination of matrix cracks and tow fractures extend almost the whole thickness of the specimen in these sections would be consistent with the last phase of fatigue damage preceding the ultimate failure.

Matrix cracks were present in all four weft. As many authors have noted, their presence causes stress concentrations which can cause fibre fractures in adjacent plies. Differently from sporadic clusters of fibre fractures detected and described for low stress levels in §5.3, here the fractured fibers oriented into the loading direction were visible along the whole warp thickness, as testified from the two micro CT images above reported, taken sectioning the specimen with two xz different planes far one each other. However, as the image is the representation of the situation before the final failure could occur, it can't be said with exactitude where the damage origin, i.e. which is the first warp tow to present damage, and how then this will determine the last failure of the entire section. Possibilities of damage late evolution might be two. Clusters of fibre fractures could present at first into the warp tow adjacent to z-crown, as external weft tow crossed over by z-tow constitute a site prone to early formation of matrix crack, as already observed for low stress levels.

These observations are similar to those of Baiocchi, except the observation of fibre fractures in the central warp tow are new (Baiocchi's 3D composite did not have a central warp tow). This may be due to the minor number constituting central warp tow, which makes it more prone to be subjected to early damage. Optical light images taken from the same specimen permitted to confirm the X-ray images, as shown in Figures 6.13 and 6.14.



**Figure 6.13** *Optical micrograph of sectioned and polished specimen showing extensive fibre fracture located into middle and low warp yarns*



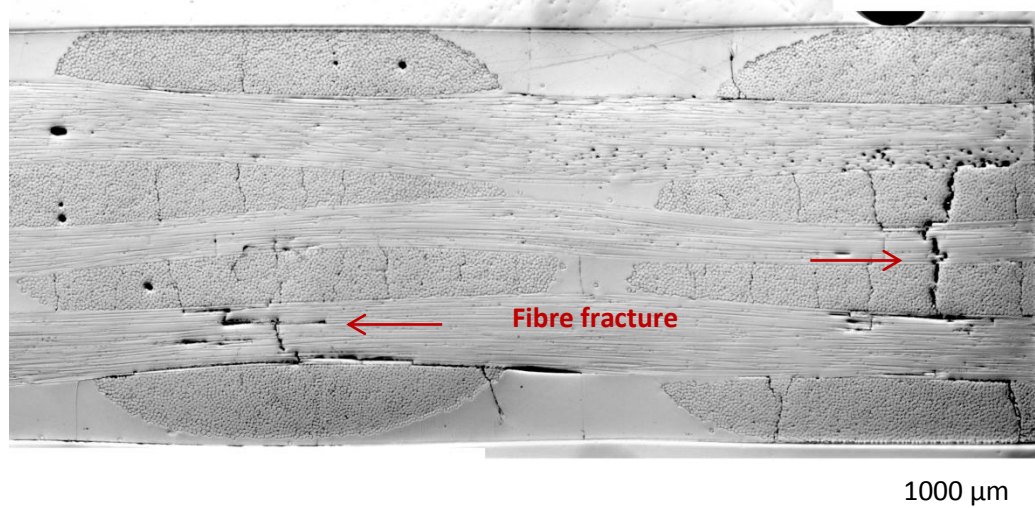


**Figure 6.14** Magnification of the optical micrograph of sectioned and polished specimen showing extensive fibre fracture located into middle and low warp yarns

#### 6.2.4 Width effects in the fatigue of warp samples

In order to understand the influence of the width of samples on fatigue behavior of 3D 96 material, tests have been conducted on specimens characterized by different widths. Such experiments have been considered after the comparison of the results of the present work with researches by other authors, e.g. Carvelli et al.. They, in fact, conducted fatigue investigations on specimens made with a similar composite material but wider specimens. Their S-N curves are shifted towards lower number of cycles to failure, as already presented and discussed into §6.2.1. The aim of this section is to understand the effect of specimen width.

Six warp direction specimens have therefore been cut with an average value of width equal to about 12 mm, while six other specimens have been cut with an average width of 24 mm. These then were divided into two groups, each constituted by three narrow and three wide specimens and undertaken to fatigue tests performed respectively at a peak stress of 200 MPa and 250 MPa. The number of cycles to failure registered for each test performed is reported in Table 6.2, starting from which the arithmetic average has been calculated. Average values obtained from the two sets of wide and narrow specimens have then been compared calculating the ratio between the two resultant values.

**Table 6.2** Results of fatigue tests on sets of samples characterized by different width dimensions. Number of cycles to failure of each test are reported together with the rate of average values calculated for each set

	Peak stress 200 MPa						
	Width = 24 mm			Width = 12mm			
	Number of cycles to failure	19181	23310	27751	19089	35908	39605
Average	23414			41378			
Deviation Std	3500			18722			
Ratio	1,77						

	Peak stress 250 MPa							
	Width = 24 mm			Width = 12mm				
	Number of cycles to failure	8033	3932	8043	4323	12056	1600	3794
Average	6670			5046				
Deviation Std	1936			3952				
Ratio	0,76							

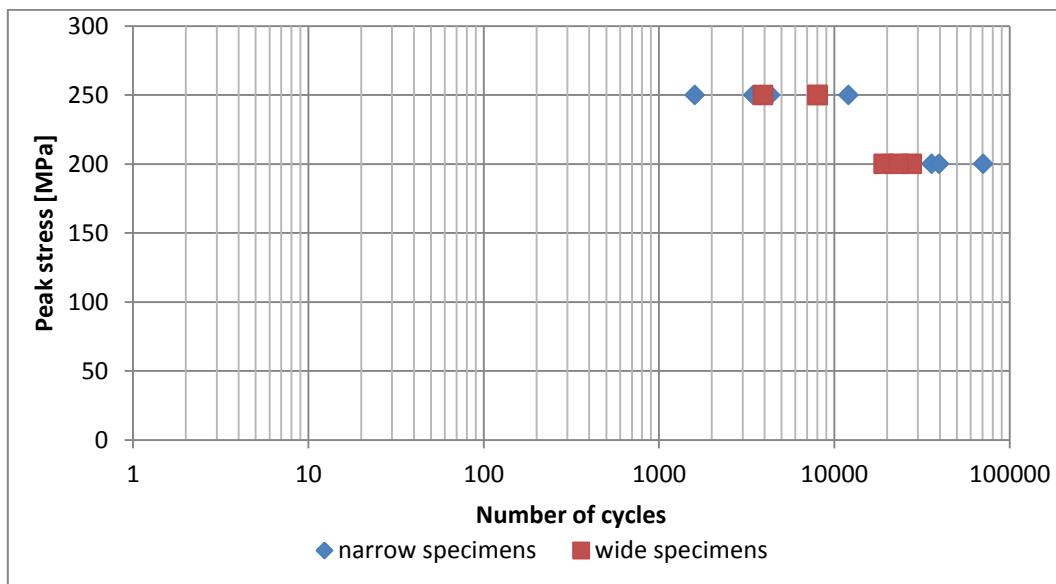


**Figure 6.15** S-N curve comparison between narrow and wide specimens

The outcomes of the experiments conducted suggest there is no effect of width for warp direction specimens. Narrow specimens have exhibited a longer fatigue-life when cycled with the lower maximum stress, and wide specimens showed an average longer fatigue-life when compared with narrow specimens for the higher fatigue stress level. However, the number of specimens may not be sufficient for conclusive results, and the investigation of the effect of width therefore, requires the conduction of more tests, here not performed for lack of time.

## 6.3 Response of the material tested along weft direction

### 6.3.1 S-N curve

In a similar way as for the warp direction, specimens have been cycled along the weft direction with maximum stresses of 350, 300, 250, 200 and 175 MPa until ultimate failure. The results for number of cycles to failure vs peak stress, or initial peak strain, permitted to get the S-N curve of the material for the fill direction, is shown in Figure 6.15. Table 6.3 also shows this data. All the specimens considered were fatigue cycled to failure.

**Table 6.3** Peak strain, peak stress, number of cycles to failure of fatigue tests performed

Peak strain	Dev Std	Peak stress	Number of cycles	Average	Dev Std
0,0176	0,00095	350	143	1678	68
0,0176		350	284		
0,0176		350	117		
0,0176		350	126		
0,0148	0,00059	300	401	511	252
0,0148		300	859		
0,0148		300	273		
0,0117	0,00079	250	1321	1595	315
0,0117		250	1429		
0,0117		250	2036		
0,0089	0,00042	200	12422	8345	2908
0,0089		200	6874		
0,0089		200	6177		
0,0089		200	11184		
0,0089		200	5070		
0,0075	0,00036	175	90034	36504	32872
0,0075		175	14669		
0,0075		175	5202		
0,0075		175	36112		

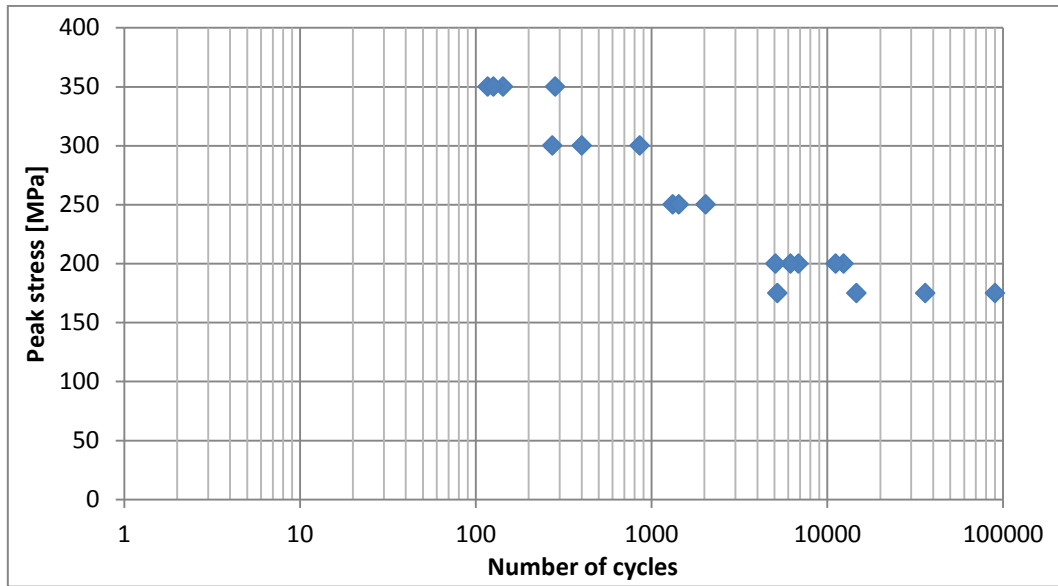


**Figure 6.16** *S-N curve for the 3D-96 specimens loaded into weft direction: number of cycles are reported vs values of peak stress.*

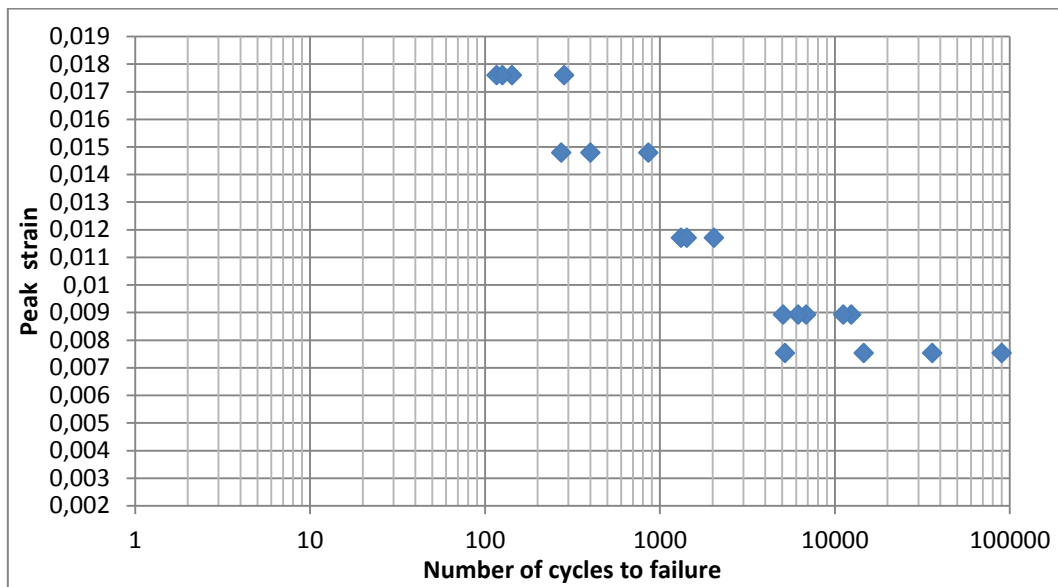


**Figure 6.17** *S-N curve for the 3D-96 specimens loaded into weft direction: number of cycles are reported vs values of peak strain*

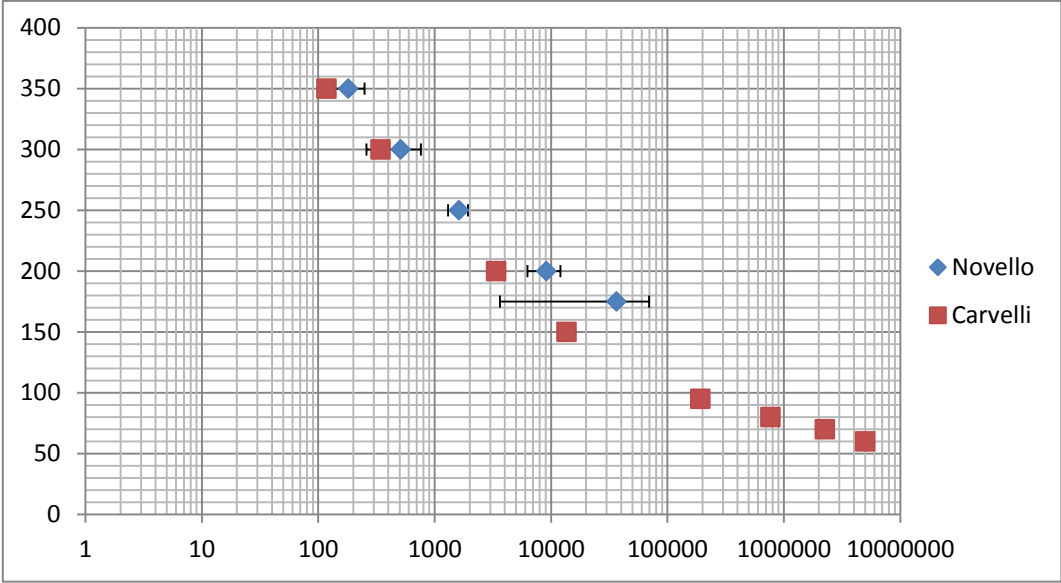
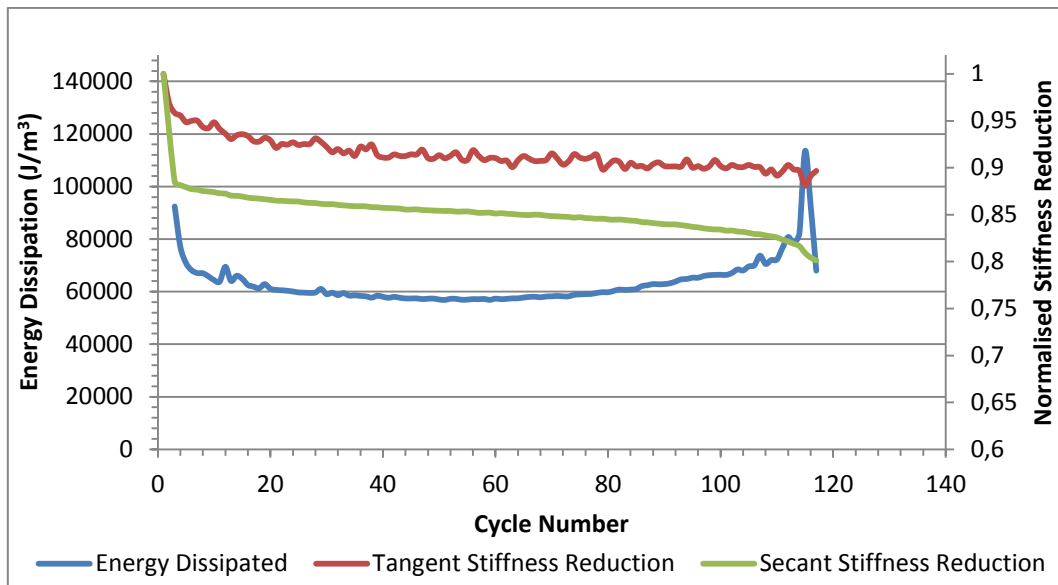


Figure 6.18 Comparison between S-N curve obtained from experimental work and S-N curve drawn from literature data (Carvelli et al.).

The S-N curve obtained was then compared with an S-N curve present in literature (Carvelli et al.) as shown in Figure 6.18. The comparison highlighted the fact that also in the case of fatigue loading in the weft direction, the average S-N curve obtained was shifted towards more extended fatigue-life for the epoxy-resin matrix specimens used in the present work, although the differences are less than for the warp direction. The causes of the differences existing between the two S-N curves remain the same: possible width of specimens effect, different resin used for the embedding of the 3D-96 fabric and different method of fabrication.

### 6.3.2 Mechanical investigation: energy dissipation and stiffness reduction

The curves of energy dissipation and stiffness reduction per cycle acquired for tests carried out with different peak stress values are shown below. All specimens have been tested until catastrophic failure occurred, while the use of the extensimeter having the 96 mm gauge length permitted the recording of strains, until the end of tests.



**Figure 6.19** Energy dissipation and stiffness reduction vs elapsed number of cycles for a test performed at a peak stress of 350 MPa. The specimen failed after 117 cycles in the gauge region.

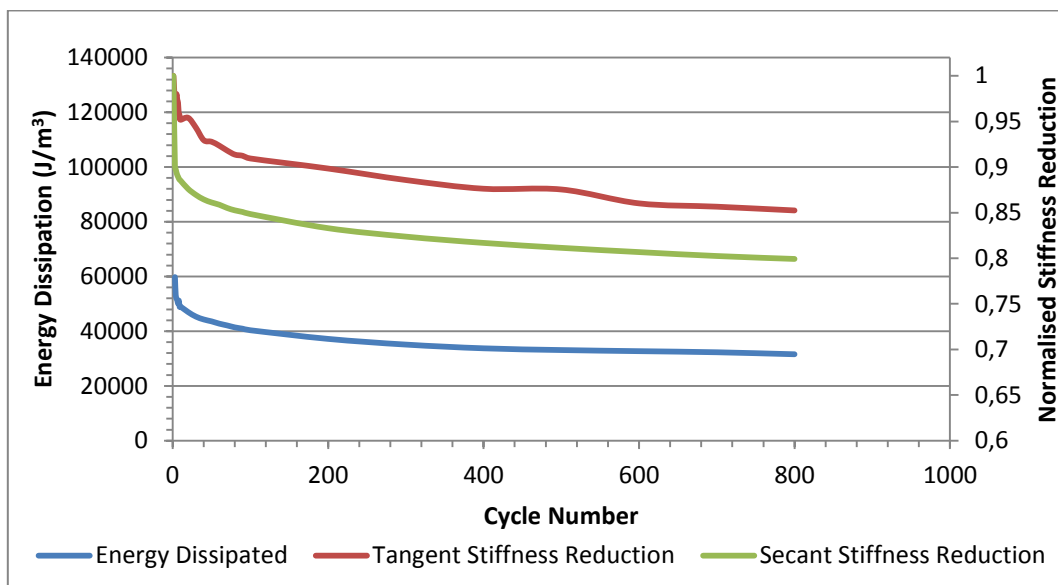


**Figure 6.20** Energy dissipation and stiffness reduction vs elapsed number of cycles for a test performed at a peak stress of 300 MPa. The specimen failed after 859 cycles in a region near the grips.

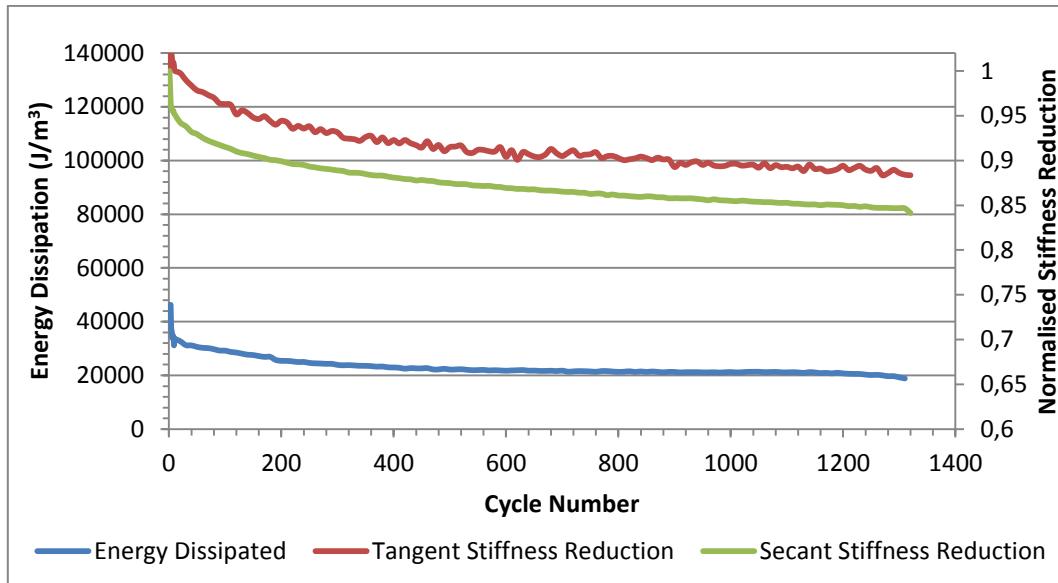


**Figure 6.21** Energy dissipation and stiffness reduction vs elapsed number of cycles for a test performed at a peak stress of 250 MPa. The specimen failed after 1321 cycles in a region near the grips.

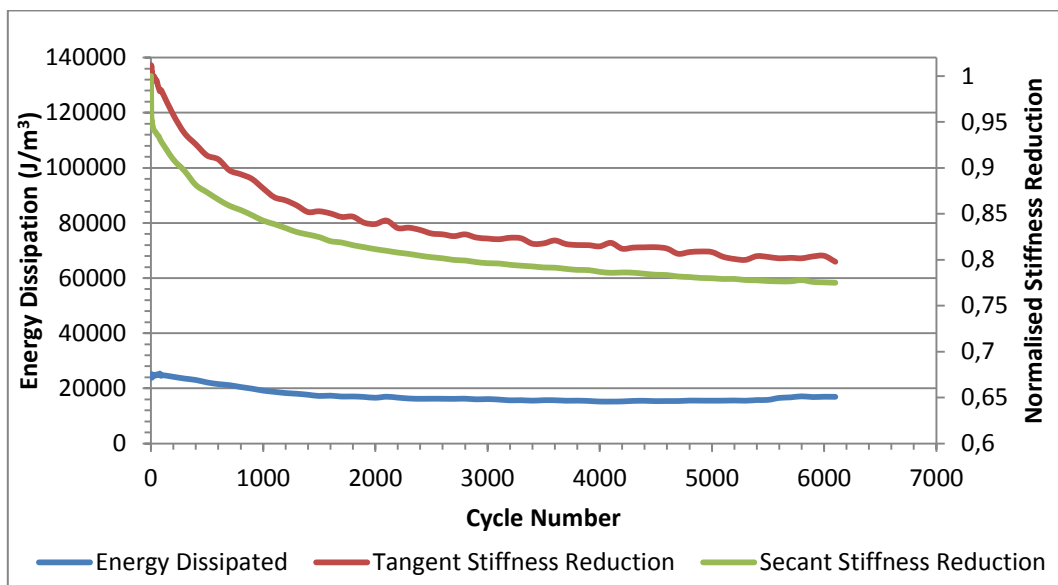


**Figure 6.22** Energy dissipation and stiffness reduction vs elapsed number of cycles for a test performed at a peak stress of 200 MPa. The specimen failed after 6177 cycles in the gauge region.

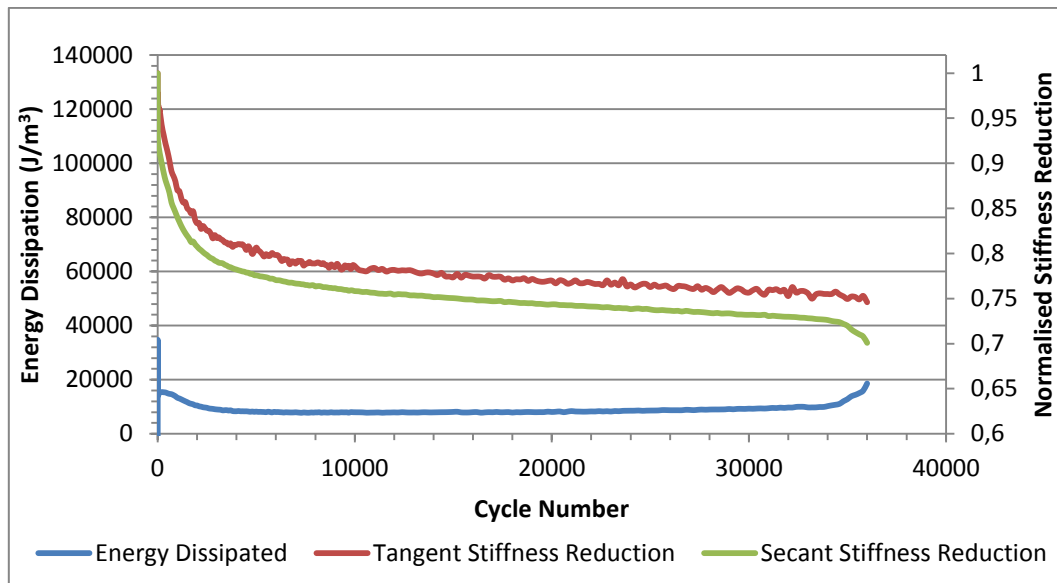


**Figure 6.23** Energy dissipation and stiffness reduction vs elapsed number of cycles for a test performed at a peak stress of 175 MPa. The specimen failed after 36112 cycles in the gauge region.

Observing and comparing the energy dissipation curves, it can be seen how the level of energy dissipation reduced with the decrease of stress. The curve kept the same trend, differing only if the failure occurred into the gauge length and could therefore be detected by extensometer, or occurred in regions influenced by the grips. The phases that were distinguishable in the case of tests performed along warp direction already described in §6.2.2, could be seen.

The trends described by the curves of energy dissipation and stiffness reduction are not dissimilar to the ones observed for specimens cycled along warp direction; the main difference consists in higher energy dissipated values for tests performed along weft direction compared with the values collected for the respective tests carried out with the same stress levels applied in the warp direction.

When specimens were cycled with peak stress levels of 350 MPa in the weft direction, energy dissipation curve obtained presented only slight difference in values reached in the case of warp direction: in the former case the peak was of 92000 J/m<sup>3</sup>, while the plateau reached values of about 57000 J/m<sup>3</sup>, energy recorded for warp direction however recorded an initial peak of 80000 J/m<sup>3</sup> while the plateau was of 60000 J/m<sup>3</sup>. In the case of tests conducted with 300 MPa, instead, the difference between the values increased: the maximum value of energy



recorded was around  $60000 \text{ J/m}^3$  for tests conducted along weft direction while for the ones conducted along warp the peak value was around  $40000 \text{ J/m}^3$ , energy values of plateau region were equal to  $33000 \text{ J/m}^3$  and to  $26000 \text{ J/m}^3$  for weft and warp. Same behaviour was observed for lower stress values. In the case of peak stress of 250 MPa, energy peak values were around  $46000 \text{ J/m}^3$ , while plateau values were of  $20000 \text{ J/m}^3$  for weft while for warp were of  $34000 \text{ J/m}^3$  and of  $20000 \text{ J/m}^3$  respectively. Passing to the case of 200 MPa, energy peak values registered maximum values of  $24000 \text{ J/m}^3$  in the case of tests conducted along the weft direction, that lowered to  $16000 \text{ J/m}^3$  in correspondence of the plateau regions, while for tests performed along the warp direction, peak values were of  $20000 \text{ J/m}^3$  while plateau values were around  $7000 \text{ J/m}^3$ . Finally, comparing the tests conducted with maximum peak stress of 175 MPa, a slight difference in values reached were still present: peak values were equal to  $14000 \text{ J/m}^3$  and plateau values were of  $8000 \text{ J/m}^3$  in the case of the weft tests, while they were equal to  $11000 \text{ J/m}^3$  and to  $7000 \text{ J/m}^3$  in the case of the warp tests. All values are indicated in Table 6.4.

**Table 6.4** Comparison between the energy dissipation values of tests carried out in the weft and warp directions

Peak stress [MPa]	Energy dissipation peak		Energy dissipation plateau	
	warp [ $\text{J/m}^3$ ]	weft [ $\text{J/m}^3$ ]	warp [ $\text{J/m}^3$ ]	weft [ $\text{J/m}^3$ ]
350	80000	92000	60000	57000
300	40000	60000	27000	33000
250	46000	34000	20000	20000
200	20000	24000	7000	16000
175	11000	14000	7000	8000

The energy dissipation values are connected with the different areas enclosed by loops of loading-unloading cycles. Consequently, the differences might indicate different mechanisms of damage, for warp and weft at the same stress levels.

### 6.3.3 Investigation of damage development

In a similar way to what has been already described for specimens tested along the warp direction, a specimen cycled with peak stress of 175 MPa loaded in the weft direction which failed in a region near the grips, was investigated using micro-computed tomography with the

aim of detecting the possible presence of fibre fractures in weft tows. The volume of examination was chosen far from the section where final failure was occurred, in a fashion to try to minimise the observation of further damage caused by the shock wave. The analysis, however, did not reveal the searched mechanism of damage, but highlighted the presence of different ones. Figure 6.22 shows two micro CT images representing the typical aspect of the damaged specimen in correspondence of a section taken in the middle of weft tows i.e. cracks that originated in correspondence of the middle plane of z-tows and extended along the resin rich regions, through the whole thickness of the specimen. Where z- tows crossed the underlying weft tows, furthermore delaminations located between the interfaces of the two were detected.

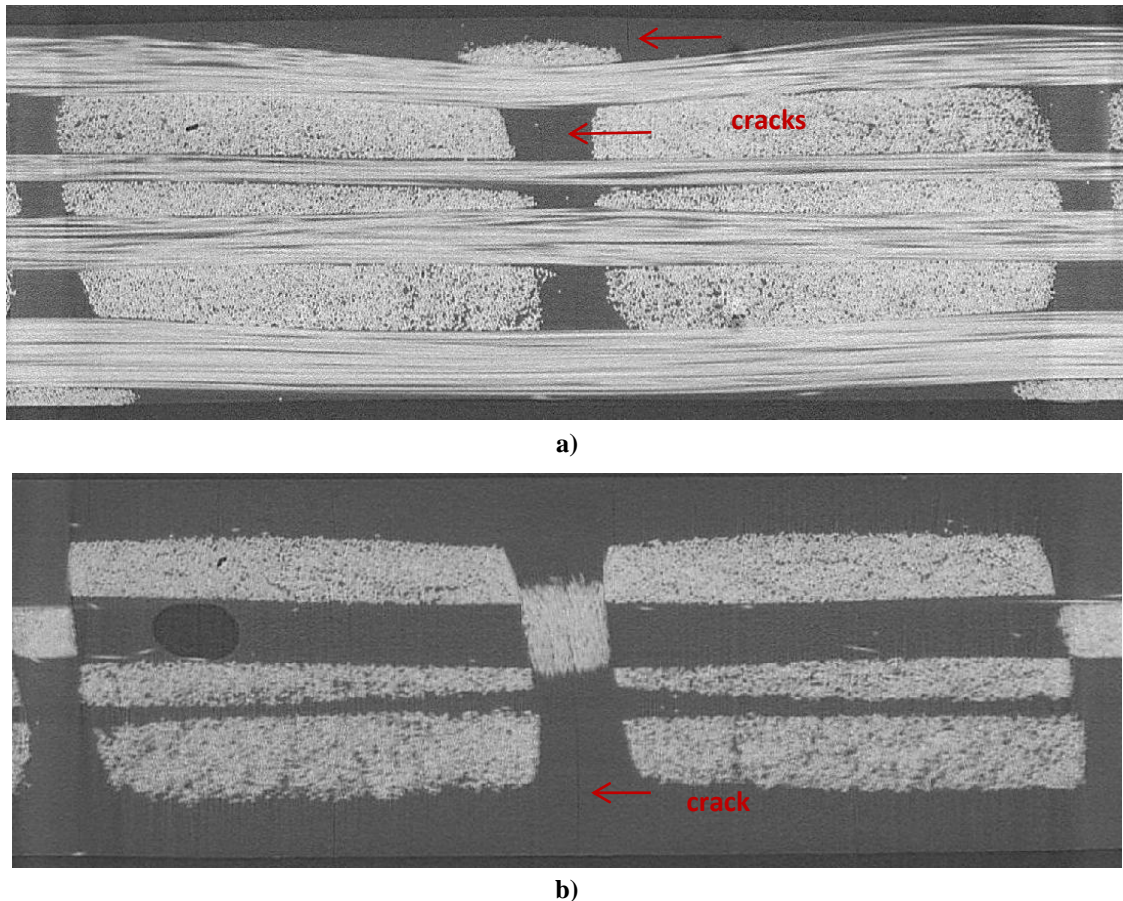


**Figure 6.24** CT images showing a) warp tows, weft tows and z-tows sections (plane Y-Z, in correspondence of weft tows) and b) warp tows and z-tows sections (plane Y-Z, in correspondence of resin rich channels).

The insufficient resolution characterizing the micro CT images collected did not permit to observe the whole amount of damage present into the specimen. This suggested the execution

of further observations of failed specimens through light optical microscopy, which results are shown in Figure 6.26.

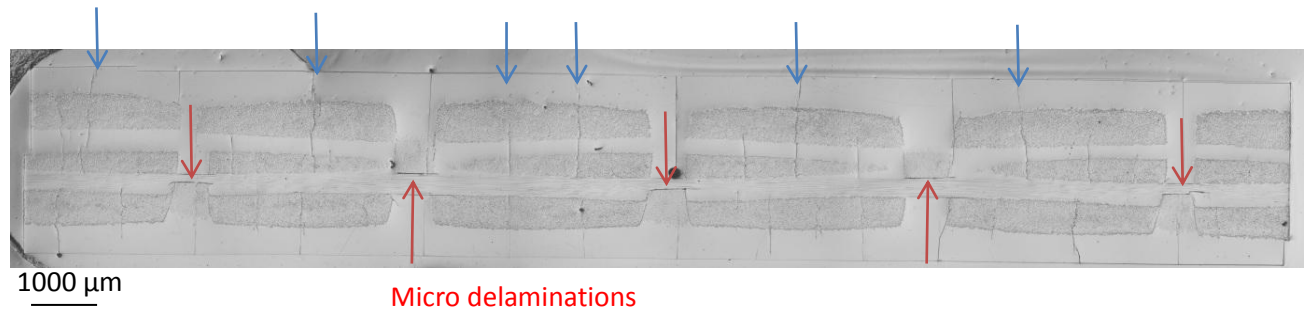
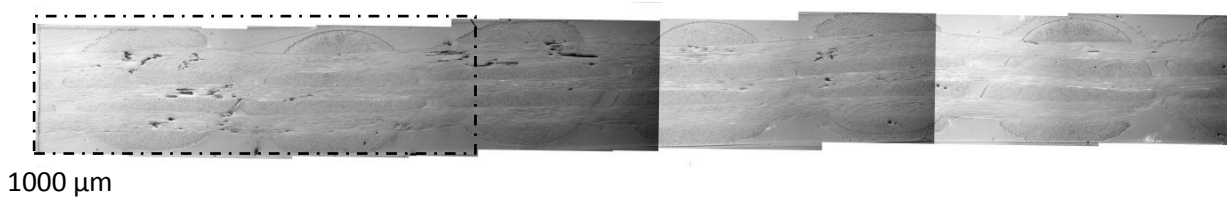


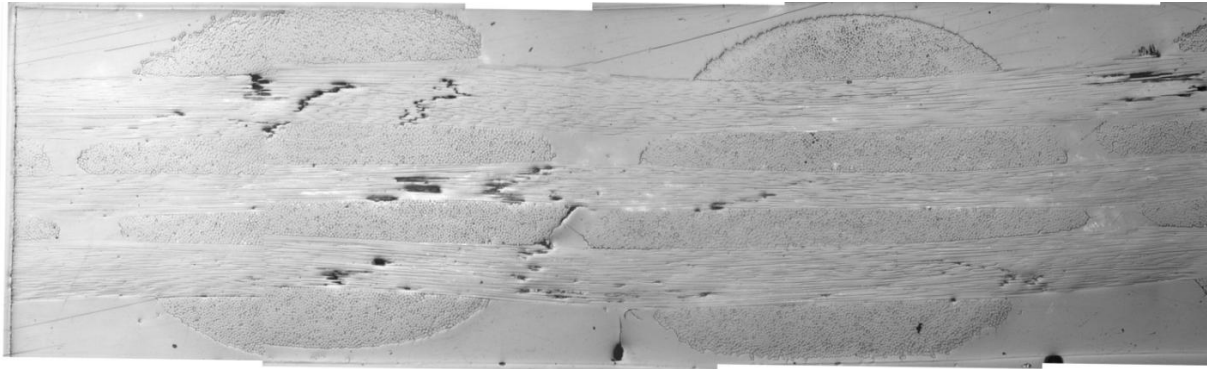
**Figure 6.25** Optical micrographs showing matrix cracks and micro delaminations between z-tows and underlying weft tows

As it can be observed in Figure 6.25, the damage consisted in formation of matrix cracks which developed through the warp tows extending and sometimes at the interface with the adjacent resin rich regions. In some cases, the cracks traversed the whole thickness of the sample, while the length of most of them was limited to the upper warp tows which were not separated by weft tows. The cracks already noted with micro computed tomography, which formed in correspondence of the sections occupied by z-tows, were clearly observable: they developed through the whole thickness of the sample, crossing the section of the z-reinforcements. Another further mechanism of damage visible was the presence of delamination between the interface shared between Z and weft tows.

When a specimen was sectioned in a plane parallel to the warp tows in a way to observe damage developed inside weft tows, the main damage detected was the fracture of fibres in warp tows. These fibres are oriented at 90 degrees to the loading direction so more research work is required to understand their origin.



a)

1000  $\mu\text{m}$ 

b)

**Figure 6.26** Optical micrographs showing a) warp fractures of a specimen tested along weft direction and b) a magnification of a tested area

### 6.3.4 Width effect in the fatigue of weft samples

To understand if the fatigue behavior of 3D 96 material in the weft direction could be influenced by the dimensions of the width of samples, three specimens were cut in the direction of the weft with an average value of width of about 9 mm, while three other specimens were cut with a width of 24 mm. The response of the two sets of specimens fatigue tested in the direction parallel to the weft tows with the same peak stress of 200 MPa was thus compared in terms of fatigue life exhibited, highlighting significant differences. Table 6.4. reports the number of cycles to failure collected from tests, their average value and the ratio calculated dividing the mean value resulting for wide specimens by the mean value for narrow specimens.

**Table 6.5** Results of fatigue tests on sets of samples characterized by different width dimensions. Number of cycles to failure of each test are reported together with the rate of average values calculated for each set

	Specimen tested in the weft direction					
	Width = 9mm			Width = 24 mm		
Number of cycles to failure	2367	1894	2262	6177	11184	5070
Average	2174,333333			7477		
Deviation Std	202,8075168			2659,91842		
Ratio	3,44					

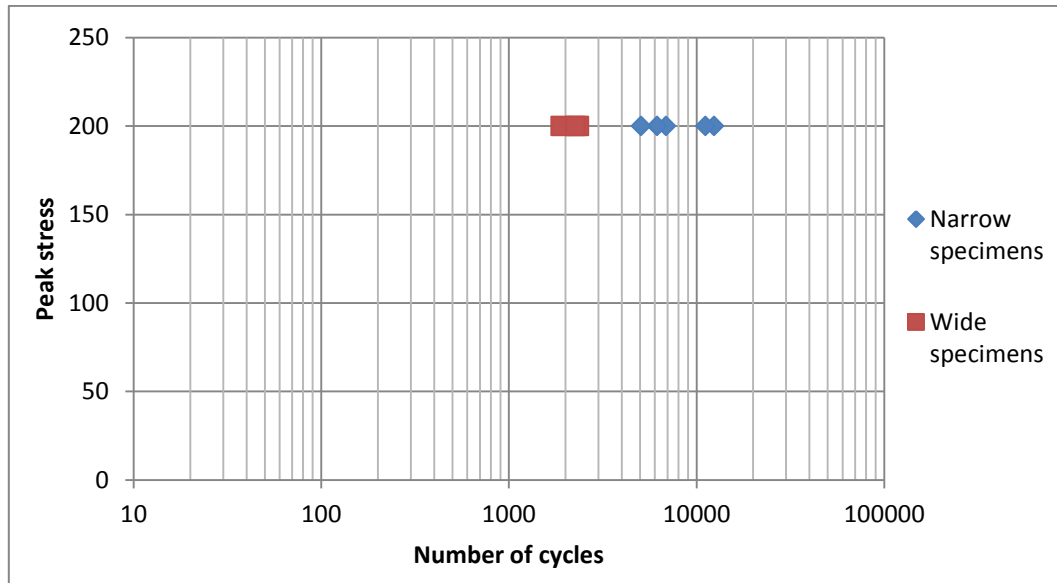


**Figure 6.27** *S-N curve comparison between narrow and wide specimens*

As shown in Figure 6.27, the narrower showed a smaller number of cycles to failure, suggesting the presence of a width effect that could affect samples subjected to fatigue tests along the direction parallel to weft tows. The lack of time, however, did not permit further tests which are required to confirm this possibility.

## 6.4 Concluding remarks

The present chapter has described the response to cyclic tensile loading at peak stress levels higher than the threshold of initiation of matrix cracking established in quasi-static tests. Data on the mechanical behaviour of specimens cycled with stress levels along both directions (warp and weft) was extracted.

Figure 6.28 shows a comparison of the results for both directions.

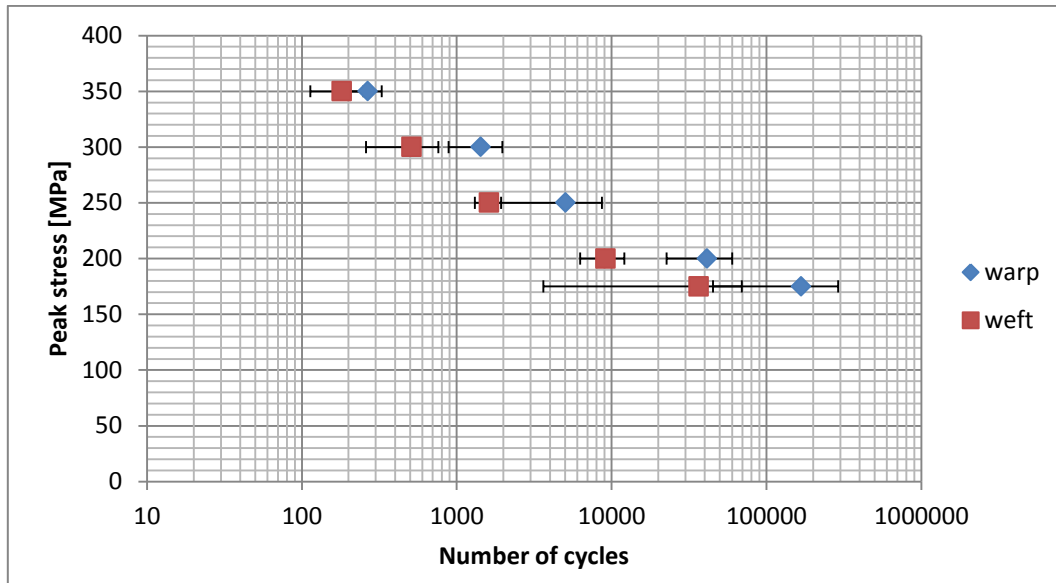


**Figure 6.28** Comparison between average S-N curves obtained cycling specimens respectively along the direction parallel to warp and weft tows.

As it can be seen, the 3D composite fatigued in warp direction showed slightly better performance when compared to the weft counterpart. Differences between the response of the material loaded along both directions were observed also by Carvelli et al.

After having presented the S-N curves, trends of energy dissipation and stiffness reduction were analysed. Although the values that characterized the peak and the plateau region of energy curves were sometimes significantly different, the phases that could be distinguished were the same:

- i. First stage characterized by a rapid stiffness reduction and a high energy dissipation per cycle;
- ii. Second stage presented a gradual stiffness degradation and a slight increase energy dissipation;
- iii. Third stage, which led to ultimate failure, showed a rapid stiffness reduction together with a large increase in energy dissipation.

Investigation conducted on specimens close to final failure, were conducted by means of micro-computed tomography X-ray combined together with optical microscopy. This permitted to observe the presence of bundles of fibre fracture in warp tows, which might originate due to the stress concentration due to formation of matrix cracks in the weft tow and

---

in the adjacent resin pocket, as already theorized for the similar 3D-78 composite (Baiocchi, 2013). One peculiarity to be highlighted is constituted by the fact that fibre fracture was observed not only in the outer warp tow near the crown-region, but also in the the inner tow.

Optical images taken from samples tested in the weft direction, revealed the presence of transverse matrix cracks extending the whole thickness of specimens. Further matrix cracks were observed in warp tows. The same warp tows, when observed in the section showing their length, were seen to contain fibre fractures, which is unexpected and as yet, unexplained.

The final aspect dealt in the chapter regards the possibility that fatigue life was subjected to the influence of width dimension chosen for specimens. Experimental tests shown a width effect for weft direction specimens (since wide specimens failed earlier than narrow specimens), while the same effect was not present for specimens fatigue tested along the warp direction.

The next chapter will present the results of thermography investigations conducted on specimens cycled with different stress levels, connecting the temperature evolution with the damage development, energy dissipation and stiffness reduction trends.





# Chapter 7

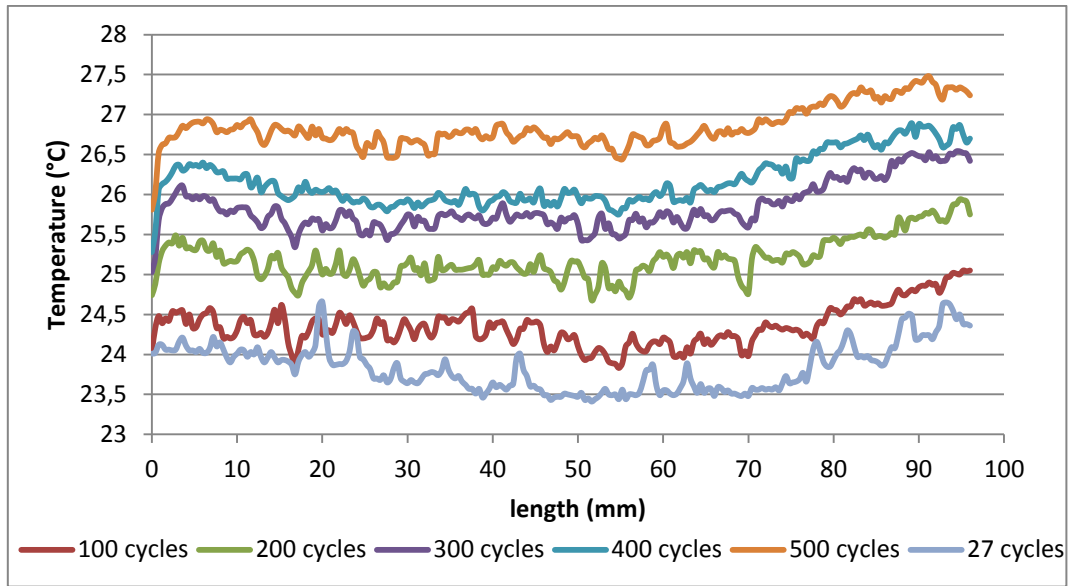
## Thermographic observations

### 7.1 Introduction

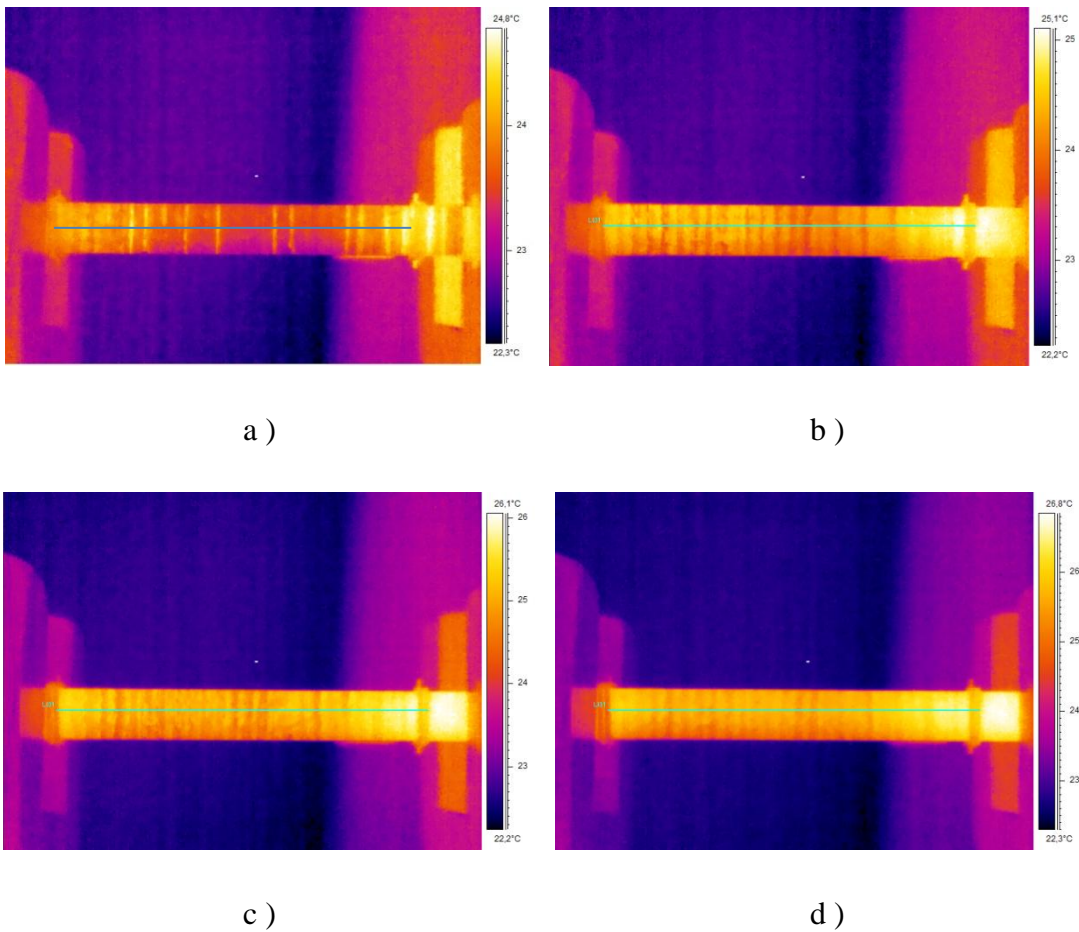
In order to obtain a comprehensive mapping of the damage developed inside the material, temperature evolution was monitored through the use of thermographic investigations. Two types of tests were carried out. On a first moment, a possible link between the changes of temperature and the structure of the specimen has been investigated. Later, instead, the comparison of the trend described by the temperature evolution with the elapse of fatigue life with the one described by energy dissipation was explored. Results will be shown in the present chapter.

### 7.2 Temperature evolution of early stages of damage

With the aim of observing if it was possible to establish a correlation between surface temperature changings and structure of the material, a video of temperature evolution was recorded with a frequency of 60Hz, using an IR thermo-camera, as previously explained on section §2.9. The specimen was cycled into the warp direction with a peak stress of 200 MPa. Since the interest was focused on the matrix cracks formation, the test has been stopped after 583 cycles. Figure 7.1 shows the temperature profile evolution of a line drawn onto the surface of the specimen, which extension was equal to the gauge length of the extensometer. In the x-axis the distance in mm from the left extremity of the drawn line is represented.



**Figure 7.1** Temperature profile development measured along a line on the surface of the specimen at the elapsing of cycles. The x-axis represents the x coordinate of the point where temperature has been measured in mm.  $X=0$  corresponds to the left extremity of the line.



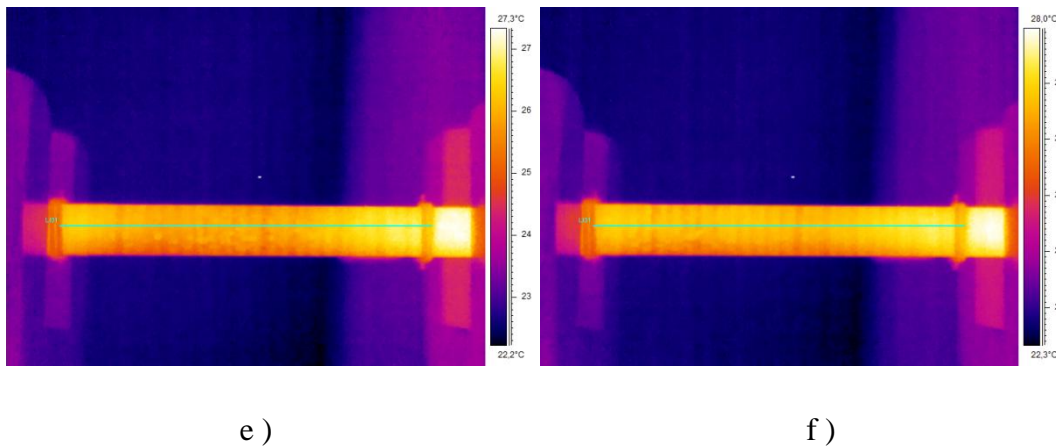


**Figure 7.2** Thermal IR images of specimen taken at different number of cycles; respectively at a) 27, b) 100, c) 200, d) 300, e) 400 and f) 500 cycles

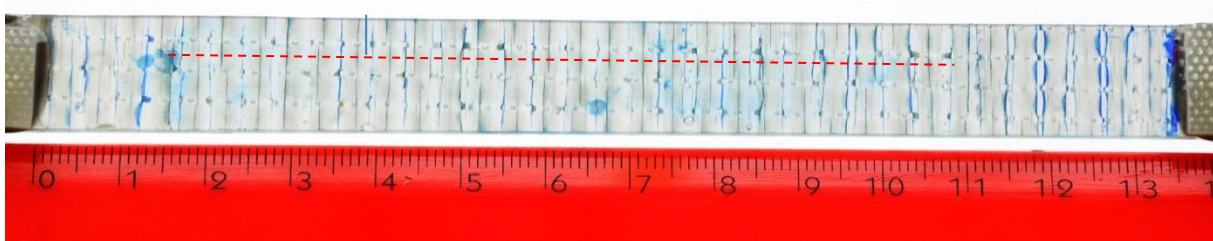


**Figure 7.3** Specimen fatigue tested to peak stress of 200 MPa after 583 cycles used for thermography. The dashed red line indicates the positions where temperature has been measured during test.

As predictable, the temperature measured on the line increased with the elapsing of the cycles. The explanation might be found in the fact that as the cracks grow and multiply in number inside the composite, energy increases, more heat is generated and temperature increases accordingly.

Another interesting aspect to highlight regards the link existing between temperature profile with the structure of the material. The temperature profile measured per cycle, in fact, presented a trend in which the sequence of peaks and valleys repeated itself with the same periodicity that characterized the 3D structure of the material. As to prove the assumption, after having calculated that the distance between two adjacent weft tows was equal to 0.378 cm, the typical distance between two sequent temperature summits was measured, making a particular attention to the unit of measurement. As the program Therma CAM Researcher Professional 2.9 used for the thermo-analysis, in fact, provided the distances in pixels, the conversion in mm was effectuated by dividing the measure given in pixel of a line drawn

between the two blades of the extensometer, for its note length. The passage is reported in equation 7.1. The ratio R gave the factor to pass from the unit of pixels given by the software to the unit of mm.

$$R = \frac{\text{distance in pixel}}{\text{distance in mm}} = \frac{240}{96} = 2.5 \quad (7.1)$$

The calculation was not deprived of errors, which had to be taken into account reading the distances reported into the x-axis, obtained using the procedure just described. The distance readable between two nearest relative temperature maximums was around 4 mm, as it is visible in Figure 7.1. Considering the inaccuracies of the conversion above reported, the distance could be considered equal to the period characterizing the weft insertion into the 3D fabric.

Comparing the two curves reported in Figure 7.1, correspondent to the 60<sup>th</sup> and the 98<sup>th</sup> cycle, it could be furthermore observed how in correspondence of the distances where the temperature peaks were shown in the first one, in the second they had been transformed in zones of relative minimums. This might be correlated with the stress relieving of portions of material interested by cracks. Since the lines of force deviate from the nearest areas to cracks, that cannot transmit the load, these areas result thus unloaded, and so they present themselves as zones of relative minimum temperature.

### **7.3 Thermo-mechanical response of the material during fatigue life**

Figure 7.2 shows the evolution of maximum temperature detected on the surface of the specimen recorded using an IR camera versus normalized number of cycles. The specimen was cycled with a peak stress of 200 MPa along the warp direction until final failure occurred after 27751 cycles were elapsed.

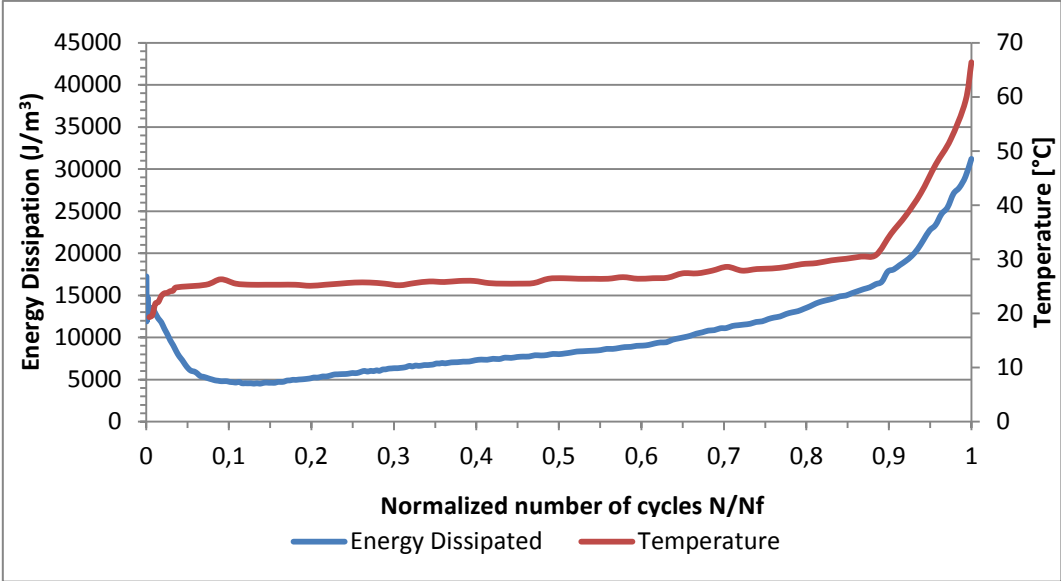
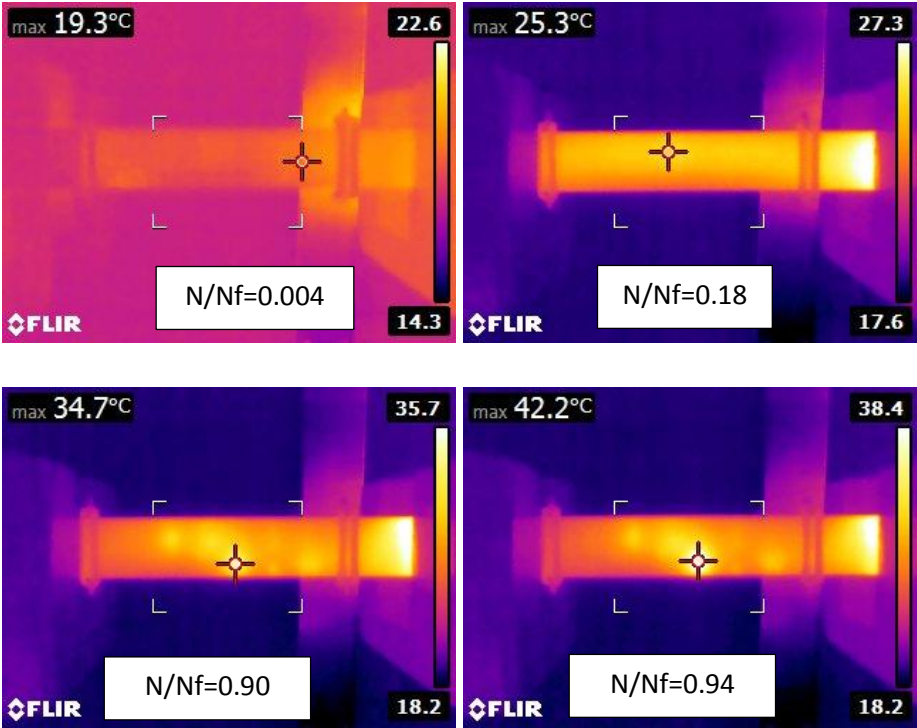
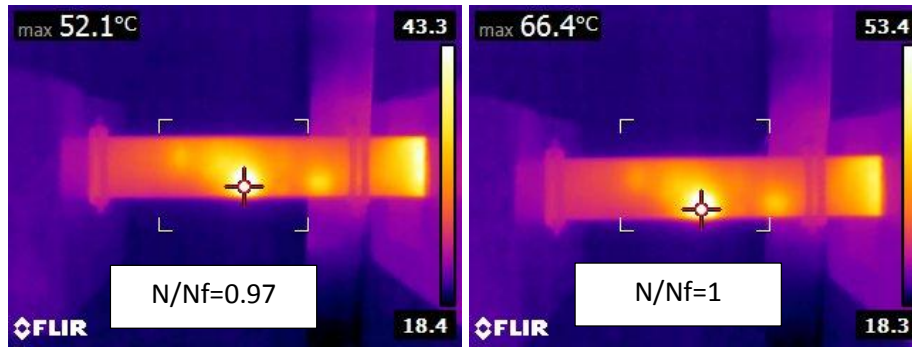


Figure 7.4 Evolution of maximum temperature compared with energy dissipated per cycle; specimen failed after 27751 cycles





**Figure 7.5** Thermal images of the specimen tested to failure; in the text box the normalized number of cycle is indicated

Figure 7.1 revealed that temperature followed an evolution very similar to the one observed for energy dissipation. Even in this case, in fact, three stages were distinguishable:

- I. Stage I consisted into an initial rise of maximum surface temperature;
- II. Stage II presented a slow and steady increase;
- III. Stage III showed a severe increase prior to failure.

The first stage was limited to the 10% of the whole lifespan of the specimen. It occurred in concomitance with the initial decrease recorded by the energy dissipation curve, which was due to the occurrence of micro-delaminations between z-tows and adjacent weft tows near the z-crowns regions and initiation of matrix cracks into the weft tows nearest to the z-crowns.

The second stage coincided instead with the growth of the matrix cracks present into weft tows, it continued until damage evolution became stable and a saturation level of matrix crack density was reached. The duration of this phase was extended from the 10% to the 80% of the lifespan, representing thus the longest part of the three.

In the third and last stage, which lasted only the final 10% of the lifetime of specimen, the temperature rose severely, following the trend depicted by energy dissipation. This stage was believed to be associated with the formation of bundles of fiber fracture into warp tows parallel to the loading direction, that then finally could have brought the specimen to catastrophic final failure. This drastic increase of temperature is comprehensible, as the advance of cracks, so far concerning only matrix regions, has to involve the cutting of fibers, hence much energy is required, resulting in a considerable heat generation.

A second type of experiment was carried out. The peak stress level was always of 200 MPa, while temperature evolution was monitored measuring the changes occurring along a line, which extended through the whole gauge length of the extensimeter. Figure 7.3 shows the

temperature development at the elapsing of cycles vs the distance expressed in mm from the left blade of the extensometer, while Figure 7.4 illustrates the curves of energy dissipation and stiffness reduction measured during the test. Once that the point that registered the maximum excursion of temperature was individuated, the temperature evolution at the elapsing of cycles of that point was reported, as represented in Figure 7.5.

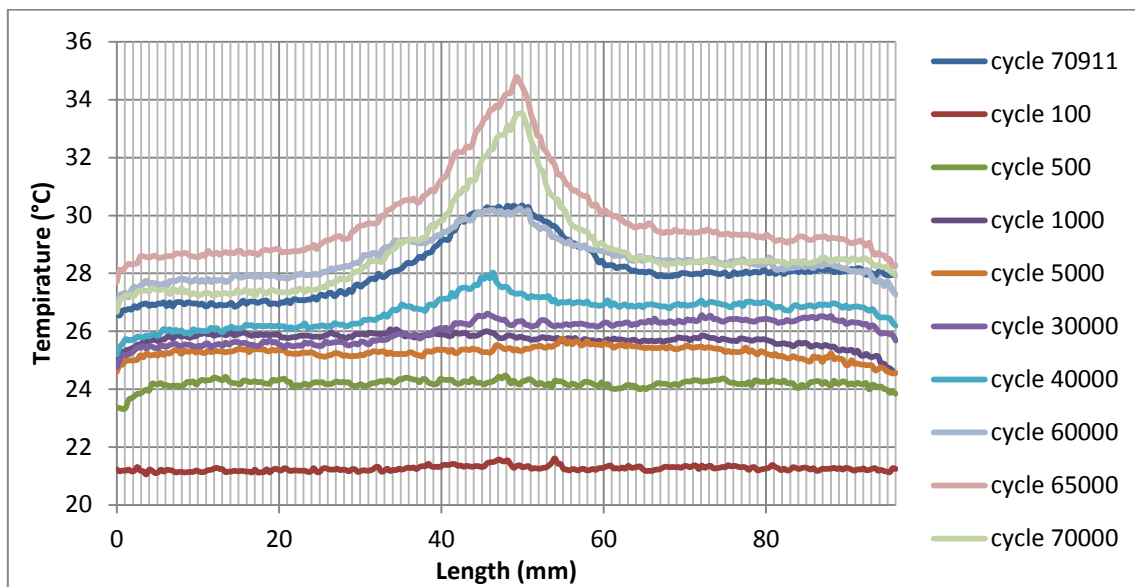


Figure 7.6 Temperature evolution with the increase of number of cycles measured along the gauge extensimeter.

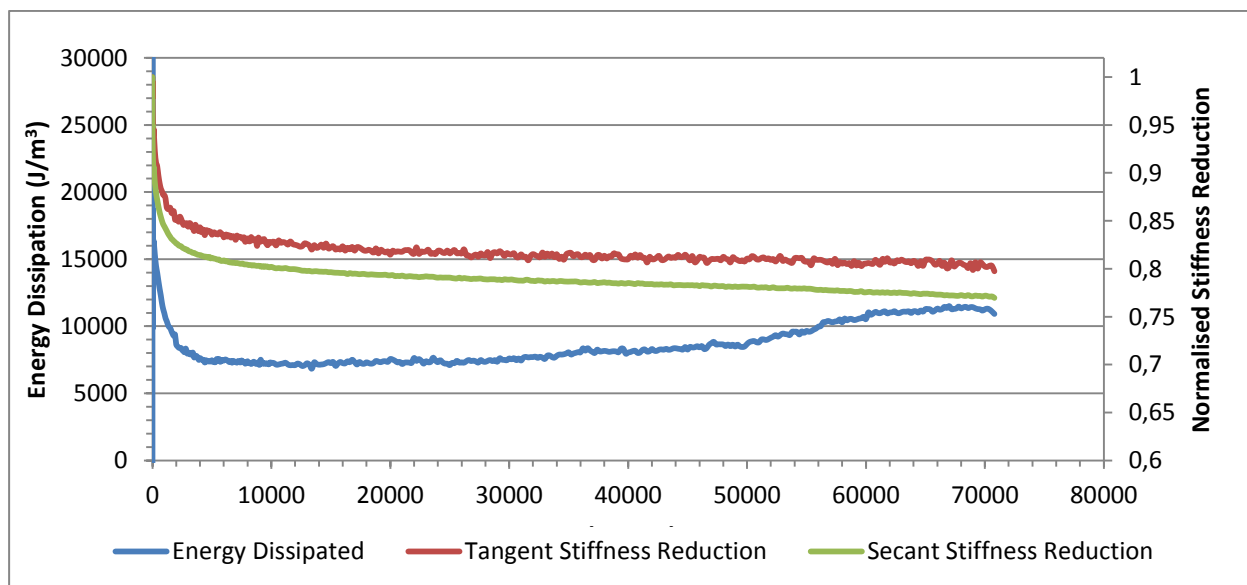
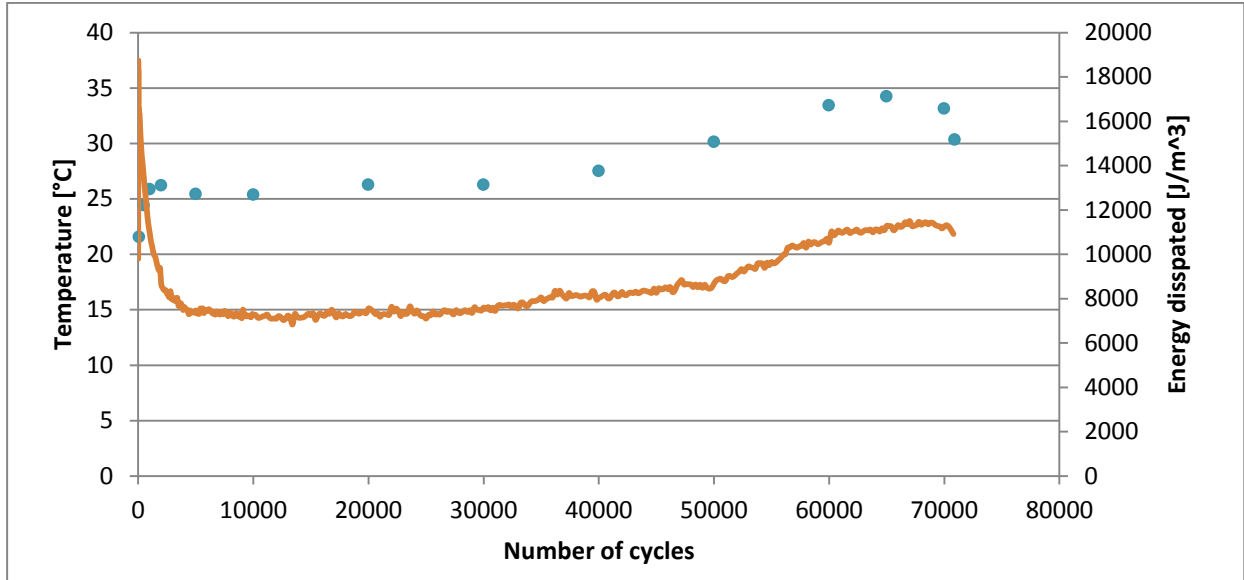


Figure 7.7 Energy dissipation and stiffness reduction per cycle





**Figure 7.8** Comparison between energy dissipation and evolution of maximum peak of temperature vs number of cycles

The first two stages of high and then steady increase of maximum temperature are visible in Figure 7.5. Then, starting from cycle number 40000, the third stage began as the temperature recorded a renewed sharp increase, which continued along almost the rest of lifespan of the test.

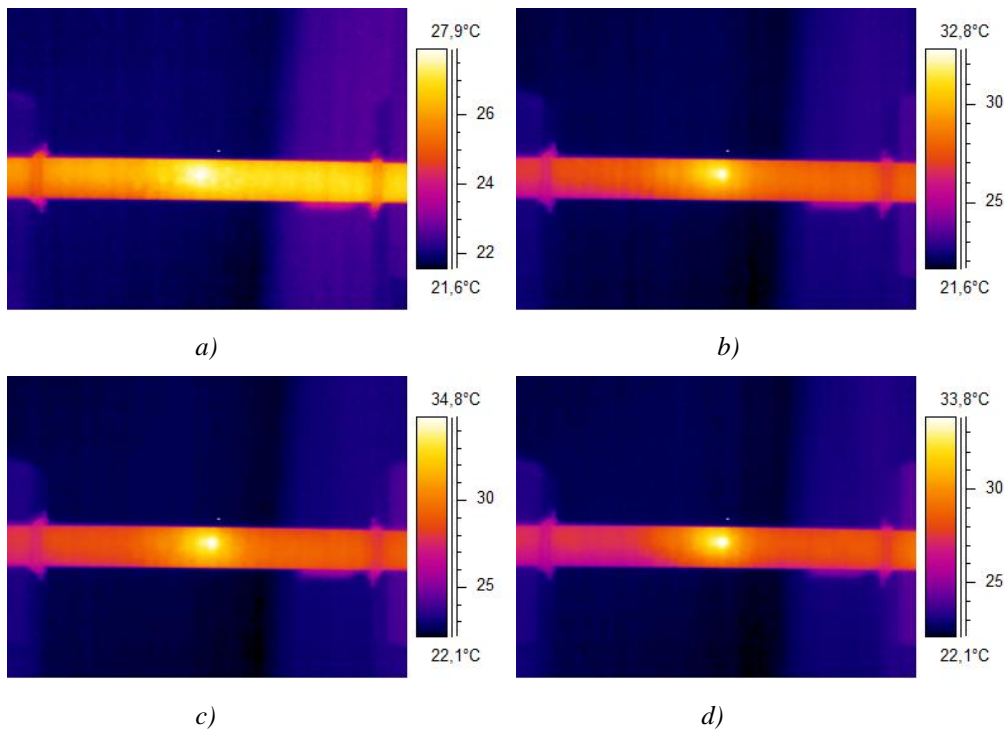


**Figure 7.9** Thermal images collected at a) 40000 cycles, b) 55000 cycles, c) 65000 cycles and d) 70000 cycles.



Looking and comparing the thermal images shown in Figure 7.9 collected during the test with the profile of temperature measured, it has been revealed that the initiation of the last stage coincided with the formation of an hot spot into the centre of the gauge length of the specimen. The rise of temperature of the hot spot is visible in Figure 7.3, readable in correspondence of a distance  $x=49$  mm from the left blade of the extensometer. The peak of temperature was hence reached after 65000 cycles were elapsed. After that, the whole profile of temperature measured decreased and the peak smoothed, until the final failure of the specimen occurred after 70911 cycles, in a zone that underwent the influence of the vicinity with the grip, which had not signalled dramatic different changings of temperature.

The decrease of the peak was believed to be due by the origination of the second site of critical damage inside the material that would have brought the specimen to ultimate failure. This might have relieved the amount of damage imparted to the zone where the temperature increase had been formerly observed.

## 7.4 Concluding remarks

In the present chapter, the results of different thermography investigations have been reported. Beforehand the correlation existing between the peaks revealed into the temperature profile detected per cycle and the 3D structure of the material has been investigated. The comparison between thermal images, the profile of temperature measured along the length of the specimen and the aspect of the damaged specimen after the test, permitted in fact to associate the origin of the peaks of temperature with the growth of those matrix cracks that reached the surface of the specimen.

After that, the entire profile described by the maximum temperature on the surface of the specimens fatigue tested was represented vs the elapsing of cycles. The trend presented three stages, in analogy with what observed for the trend of energy dissipation. The first stage was characterized by a high increase of temperature, followed by a second stage where the increase became slow and steady and by the final third stage where the increase recommenced to increase with a sharp steep, until final failure occurred.

The usage of the temperature monitoring is believed to be of help to localize the principal sites where massive damage occurred. However, this affirmation needs to be confirmed by further tests followed by tomography and microscopy analysis.



# Chapter 8

## Conclusions and further work

### 8.1 Conclusions

The actual work have presented an investigation of damage development of a 3D woven composite carried out by means of a wide range of experimental techniques. The complexity of the architecture of the fabricated composite resulted in fact into a multiplicity of mechanisms of damage involved, which required the use of different experimental investigations for being better analysed and understood.

To this end, a transparent composite was first of all fabricated using the non-crimp single ply 3D orthogonal glass reinforcement (provided by 3TEX Inc, USA) and a Shell Epikote 828 (Bisphenol-A) epoxy resin.

The 3D fabric was hence initially characterized in terms of total fibre content of the material (volume fraction) and presence of pre-existing defects due to the complexity of the structure and its manufacturing process. Waviness of Z-binder, fibre crimps and initial micro-delaminations due to the thermal shrinkage that occurs during the manufacturing of the material were detected by optical microscopy analyses on untested specimens.

Conventional tensile tests were carried out on specimens both in warp and weft directions, in order to characterize the stress-strain behavior under quasi-static loadings, while monitoring and recording the damage evolution by optical techniques. This enabled the identification of relevant stress and strain levels corresponding to damage initiation (onset of transverse cracking) and accumulation, leading to the final failure.

Subsequently, fatigue tests were carried out for several maximum stress levels, both in warp and weft directions, and the average S-N curve was drawn and compared to results for similar

materials available in the literature (Bogdanovich and Mohamed, 2009; Carvelli et al, 2010; Lomov et al, 2009).

In addition, damage evolution during the fatigue tests was quantified by measuring the stiffness reduction as well as computing the stress/strain hysteresis loop areas which, in turn, corresponds to the dissipated energy. These analyses allowed to identify three main stages to be regarded as typical of the 3D orthogonal structure studied in this work. In more details:

1. The first stage was characterized by a rapid stiffness reduction and a high energy dissipation per cycle, both of them due to matrix cracking, originated by fibre-matrix debonding and crack coalescence.
2. In the second stage, while increasing the number of cycles, the crack density saturated giving rise to a gradual loss of stiffness and a slowly increase of the energy dissipated per cycle.
3. Eventually, a third stage was noted characterized by a rapid stiffness decrease accompanied by a slowly increasing energy dissipation per cycle. This phase corresponded to the specimen ultimate failure.

During the experimental campaign carried out, each of the above mentioned stages was investigated separately. Damage initiation sites and propagation paths were studied in situ using optical techniques (pictures and videos taken during the tests) and quantified by evaluating the trend of the dissipated of energy and the stiffness reduction.

Moreover, some of the tested specimen were sectioned and analyzed by optical microscopy and Scanning Electrical Microscopy.

In addition, thanks to the cooperation with the University of Manchester, some specimens have been cycled up to the beginning of the third stage and later analyzed using the X-ray micro computed tomography (CT). This allowed to observe the presence of fibre fracture, thought of as responsible for the specimen final failure, and to identify the potential sites where this phenomenon can occur. A hypothesis, still to be confirmed by further micro-CT analyses, is that the main driving factor is the stress intensification caused by cracks extending around the circumference of the warp tows.

With the aim to get further information on these events an infrared camera has been used during the fatigue tests to identify the sites where potential fibre fracture started to occur. This non-destructive technique could allow the in situ detection of failure zones and, in

---

combination with the micro CT analyses, could permit to reach a comprehensive damage mapping, especially during the latest stages of life.

Another topic on which preliminary investigations have been conducted, is the influence of the specimen width. Preliminary results indicate that the material 3D 96 is affected by a significant scale effect on weft direction, since wider specimens have resulted to be characterized by a shorter lifespan.

## 8.2 Further work

Since the present work has regarded only the presentation of results of experimental investigations, the generation of a finite element model built ad hoc for the 3D-96 composite material could be useful to complete the scenery of damage development. So far a preliminary finite element analysis has been conducted only on 3D orthogonal composites constituted by a similar 3D-78 fabric. However, the modelling of 3D composite materials made up with the different fabric could help to understand the effect that the presence of a different number of layers of warp and weft tows exercised on the response of the material subjected to tensile load.

Furthermore, additional investigations are required to establish the effective influence of the width effect on fatigue-life, since in the present project only preliminary investigations have been carried out. In fact, specimens that had different breadth values have been fatigued with few different peak stress levels, while an investigation that includes at least the whole range of stress levels adopted for narrower specimens will provide the complete picture of the width effect on fatigue life.

For concluding, starting from the surface temperature measurements conducted, the development of a model that estimates the dissipated thermal energy could permit to distinguish the amount of stored energy as the difference between the mechanical hysteresis loss and the heat dissipated through convection, conduction and radiation



# Appendix A

## Definitions

**Non crimp fabrics** are defined as multiaxial multi-ply fabrics, where the fibers of each layers are orientated straight and are laid upon each other only during the process of production. The fixation of the single layers is done by warp-knitting or by binder application.

**Areal weight** is defined as the ratio  $\frac{m}{A} [\frac{g}{m^2}]$ , where m is the mass of specimen in grams and A is the area of the specimen in m<sup>2</sup>. The ISO 3374 (valid for glass, carbon and aramid yarns) prescribes that the specimens must be cut out of the textile with a circular or square shape and an area of 100 cm<sup>2</sup>. Being careful not to lose any fibres in the following manipulation's procedures, the specimen must be dried in a ventilated oven at 105°±3° for an hour and then cooled down to room temperature in a dessicator. immediately after there operations, the weighing can be performed.

**Tex** is defined as the mass in grams per 1 kilometer, constituting a unit of measure for the linear mass density of fibers. The diameter of a filament yarn using tex can be calculated with the following formula where density in grams per cubic centimeter and the diameter is in mm

$$Diameter = \sqrt{\frac{Tex}{1000 * density * 0.7855}}$$





# Appendix B

## Quasi-static tensile tests

In the present section, stress-strain curves of 3D-96 resulting from quasi-static tests carried out along warp and weft directions not included in Chapter 4 are shown. In each figure the ultimate tensile test and the modulus of Young are indicated.

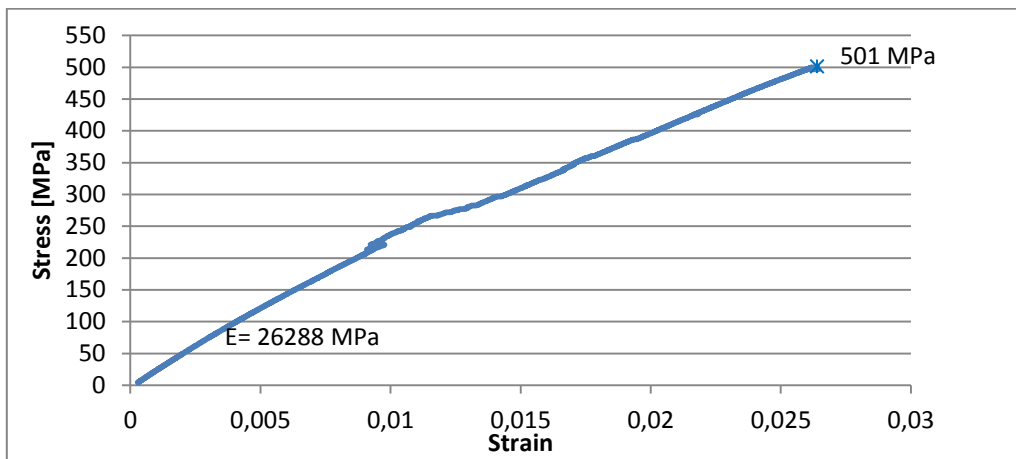


**Figure B.1** Stress-strain curve of 3D 96 along warp direction

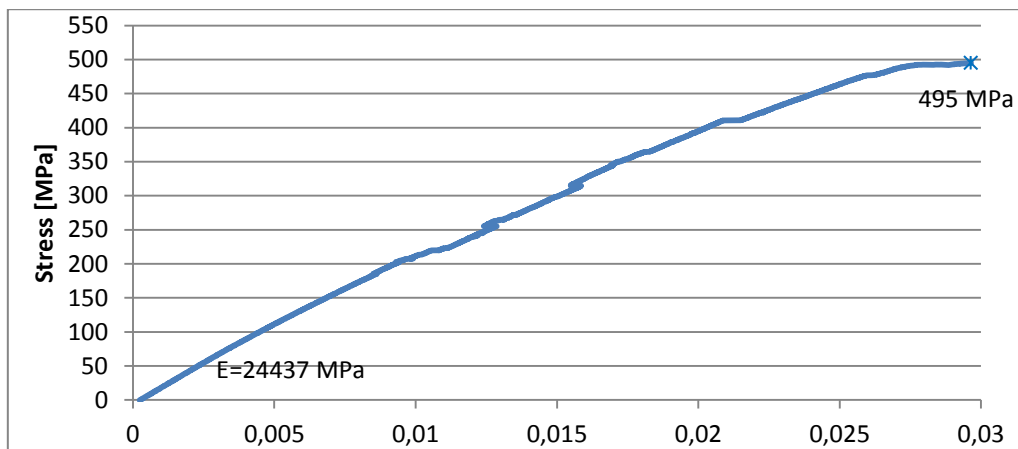


**Figure B.2** Stress-strain curve of 3D 96 along warp direction

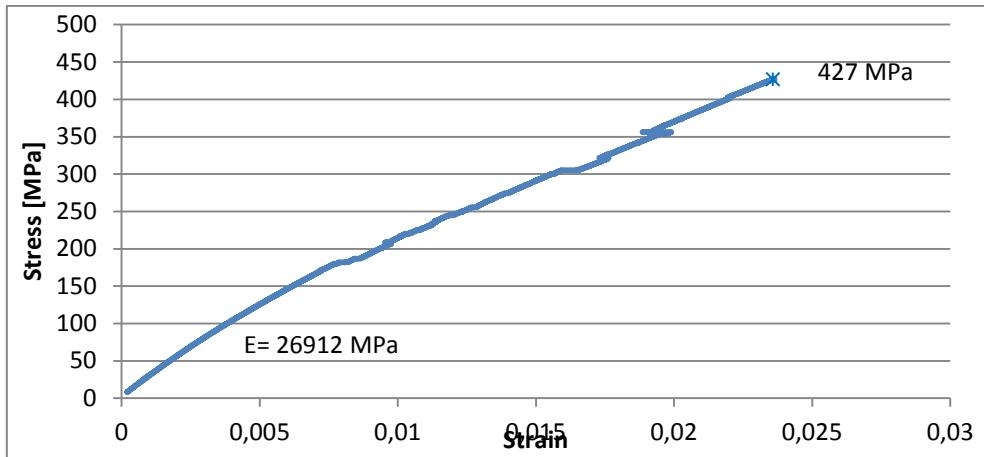


**Figure B.3** Stress-strain curve of 3D 96 along warp direction

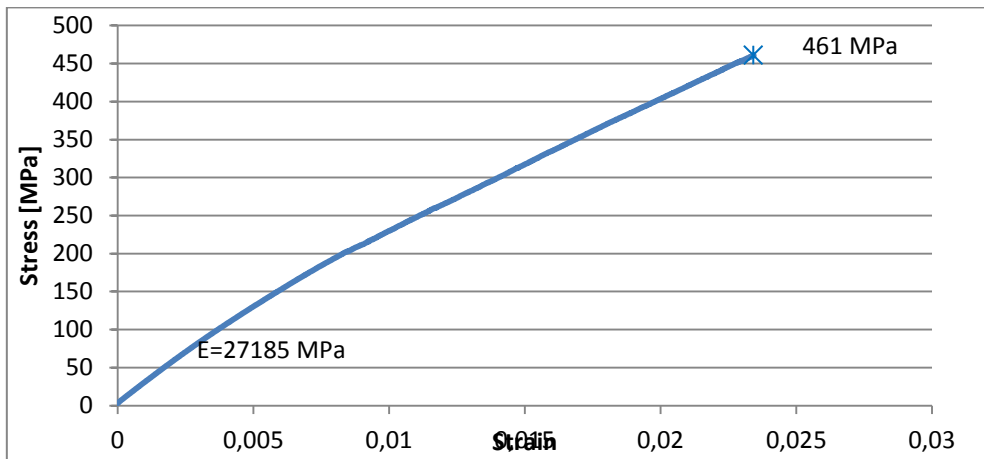


**Figure B.4** Stress-strain curve of 3D 96 along warp direction

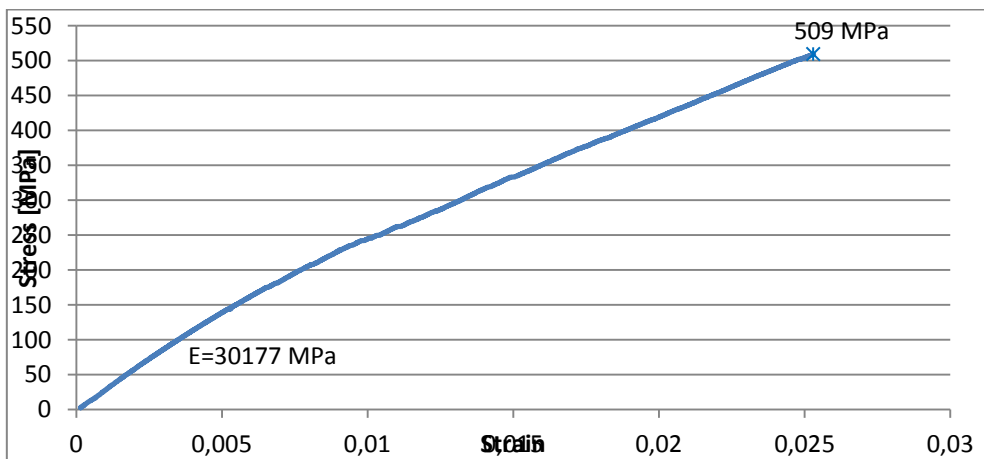


**Figure B.5** Stress-strain curve of 3D 96 along weft direction

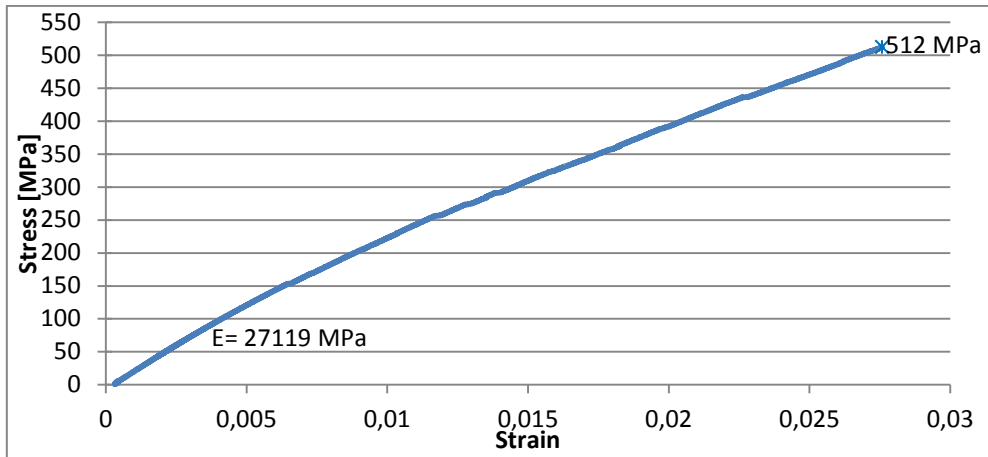


**Figure B.6** Stress-strain curve of 3D 96 along weft direction

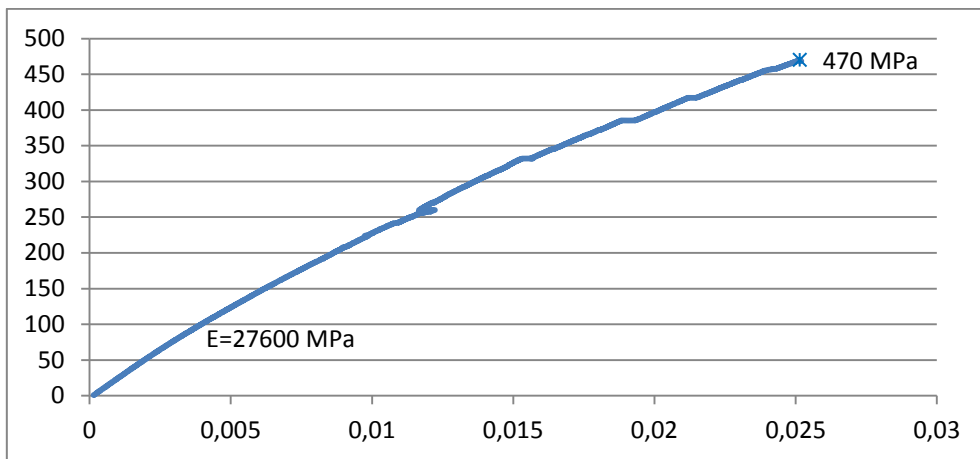


**Figure B.7** Stress-strain curve of 3D 96 along weft direction



# Appendix C

## Fatigue tensile- tensile tests

The following figures illustrate the curves of energy dissipation and the normalized stiffness reduction calculated considering the secant and the tangent method for fatigue tests conducted with different peak stress levels. These curves are complementary to the ones included in Chapter 6.

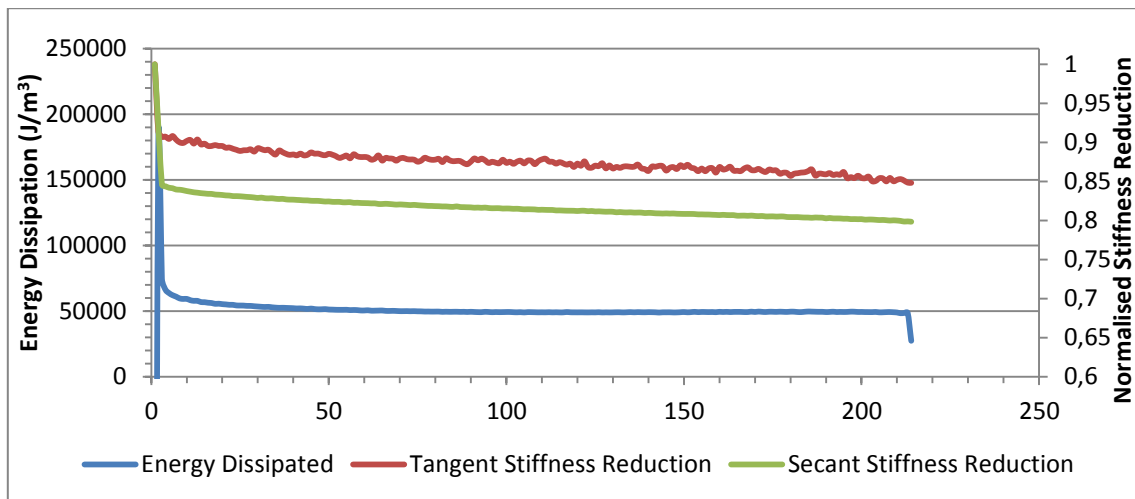


**Figure C.1** Energy dissipated and stiffness reduction curve of 3D 96 fatigued along warp direction, fatigued with peak stress of 350MPa and failed after 211 cycles

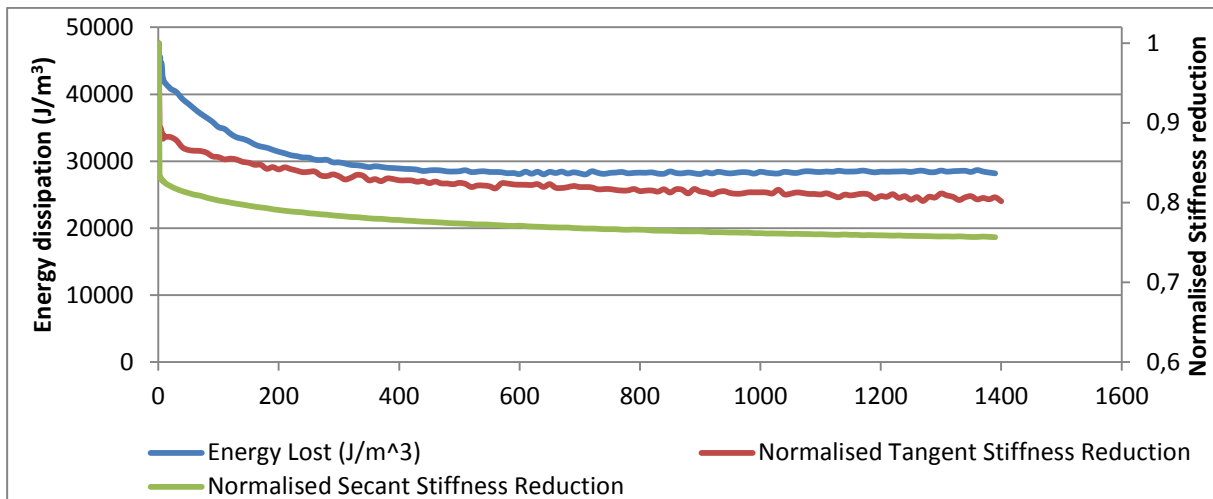


**Figure C.2** Energy dissipated and stiffness reduction curve of 3D 96fatigued along warp direction, fatigued with peak stress of 300MPa and failed after 1400 cycles

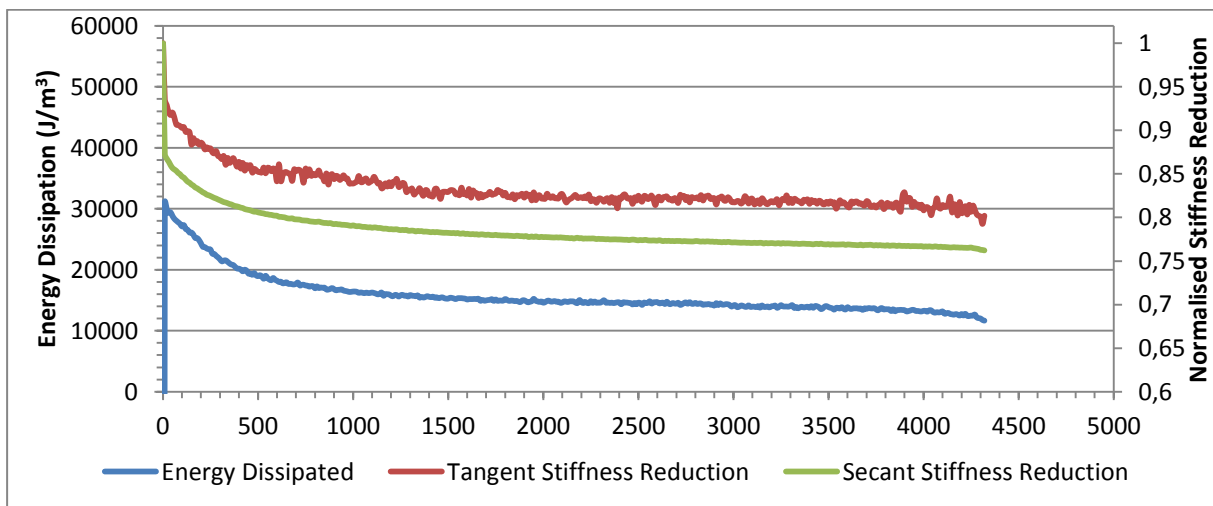


**Figure C.3** Energy dissipated and stiffness reduction curve of 3D 96fatigued along warp direction, fatigued with peak stress of 250MPa and failed after 4320 cycles

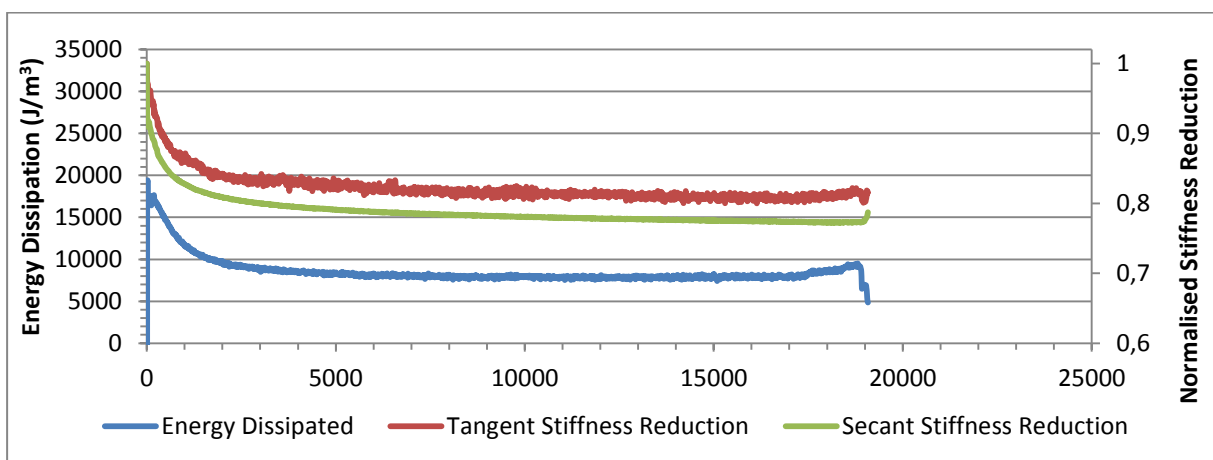


**Figure C.4** Energy dissipated and stiffness reduction curve of 3D 96fatigued along warp direction, fatigued with peak stress of 200MPa and failed after 19080 cycles

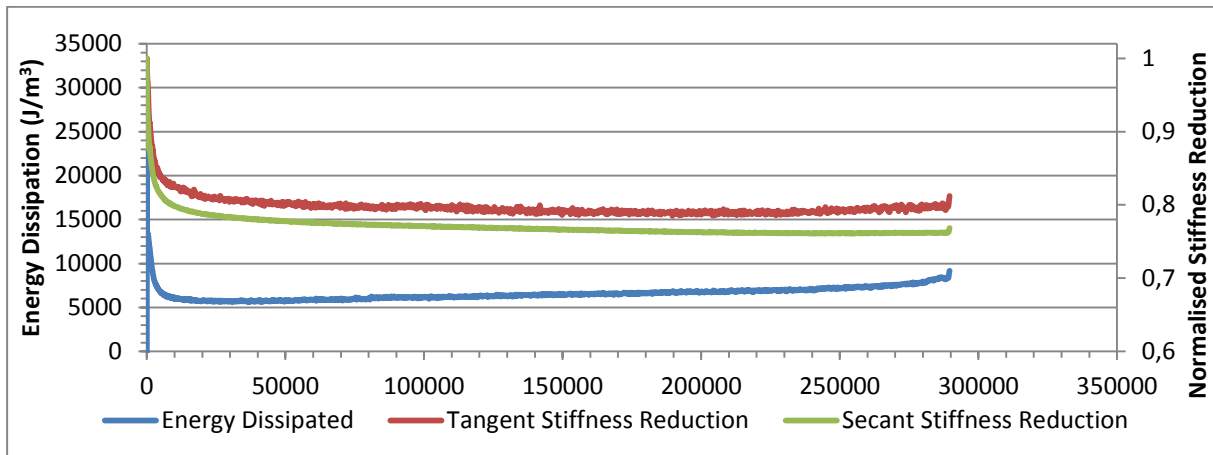


**Figure C.5** Energy dissipated and stiffness reduction curve of 3D 96fatigued along warp direction, fatigued with peak stress of 175MPa and failed after 289600 cycles

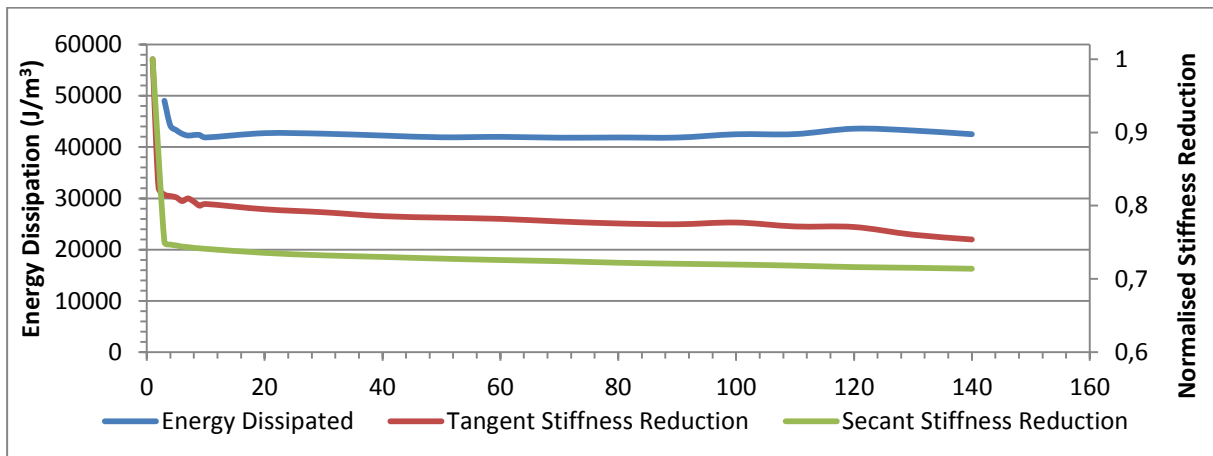


**Figure C.6** Energy dissipated and stiffness reduction curve of 3D 96fatigued along weft direction, fatigued with peak stress of 350MPa and failed after 147 cycles

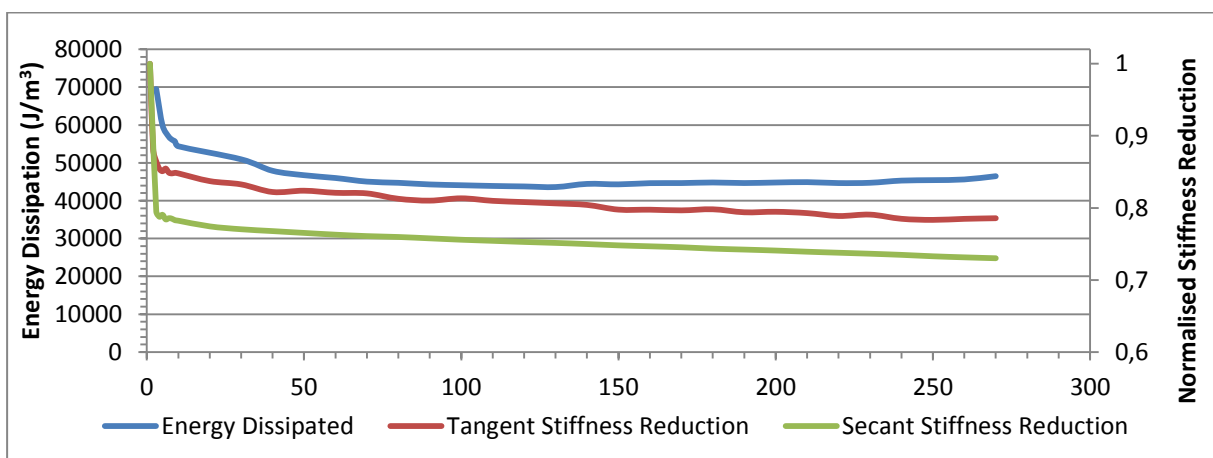


**Figure C.7** Energy dissipated and stiffness reduction curve of 3D 96fatigued along weft direction, fatigued with peak stress of 300MPa and failed after 270 cycles

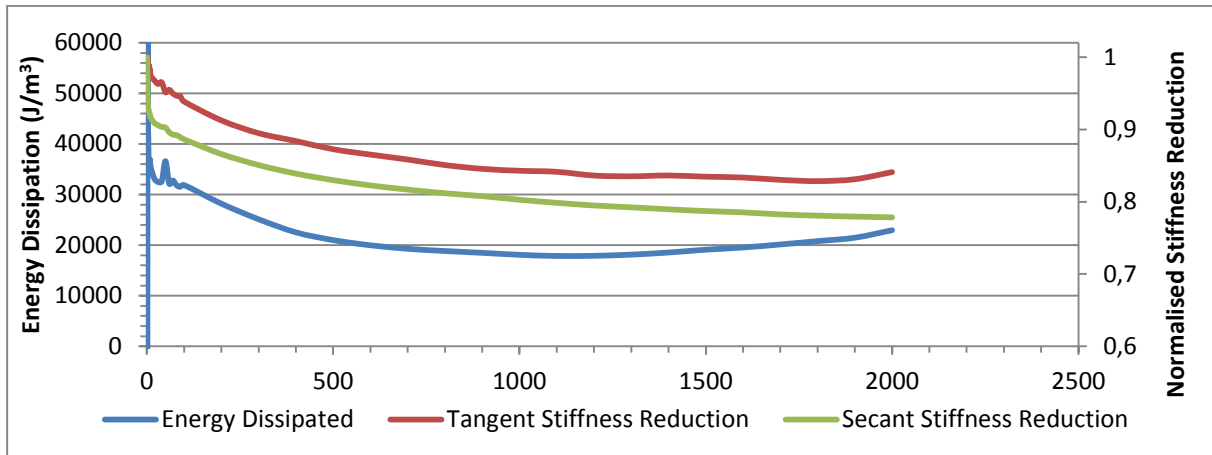


**Figure C.8** Energy dissipated and stiffness reduction curve of 3D 96fatigued along weft direction, fatigued with peak stress of 250MPa and failed after 2000 cycles

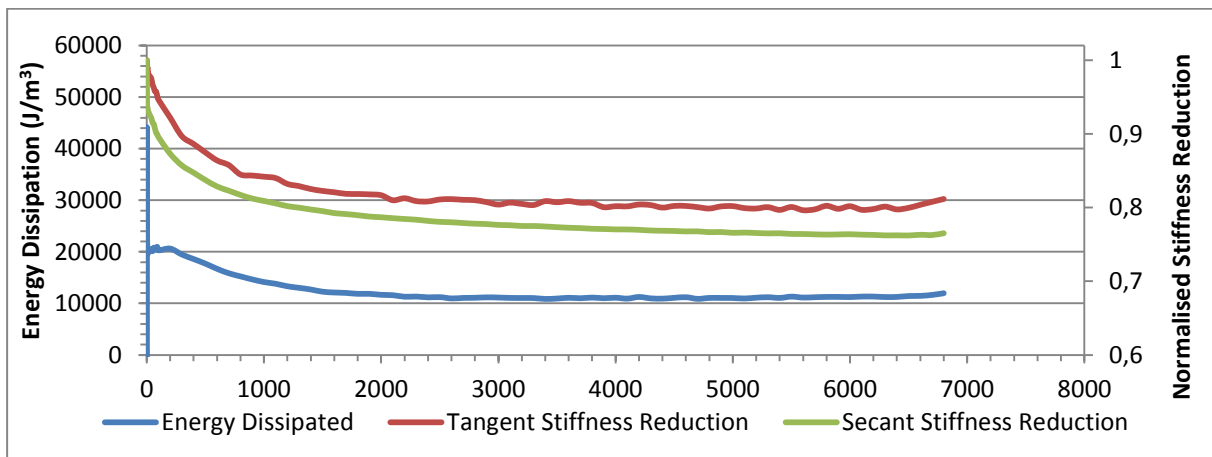


**Figure C.9** Energy dissipated and stiffness reduction curve of 3D 96fatigued along weft direction, fatigued with peak stress of 200MPa and failed after 6800 cycles

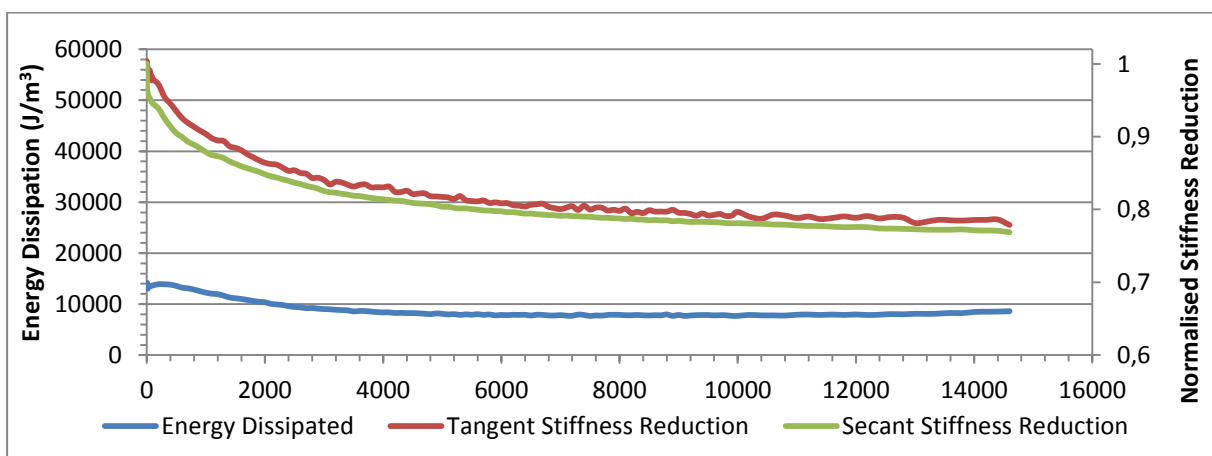


**Figure C.10** Energy dissipated and stiffness reduction curve of 3D 96fatigued along weft direction, fatigued with peak stress of 175MPa and failed after 14600 cycles



# Appendix D

## Optical micrographs

The following figures are micrograph images taken from specimens fatigued at different peak stress levels that are not included in Chapters 5 and 6. If not specified, the section plane runs parallel to the z-tow direction.

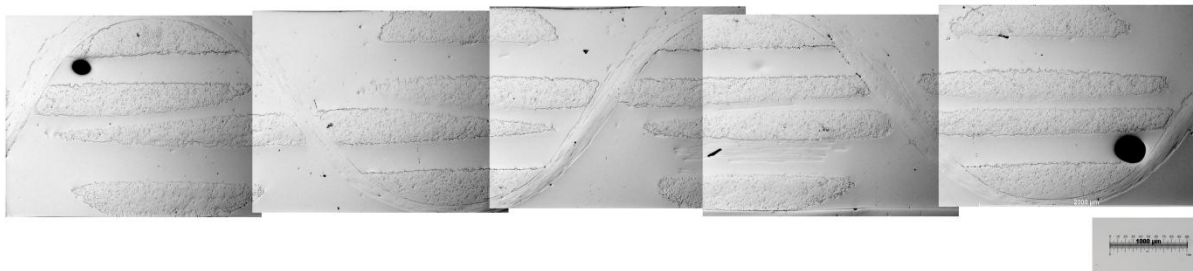


**Figure D.1** *Micrograph image taken from a specimen fatigued at a peak stress level of 50 MPa. The test was stopped after 100000 cycles.*

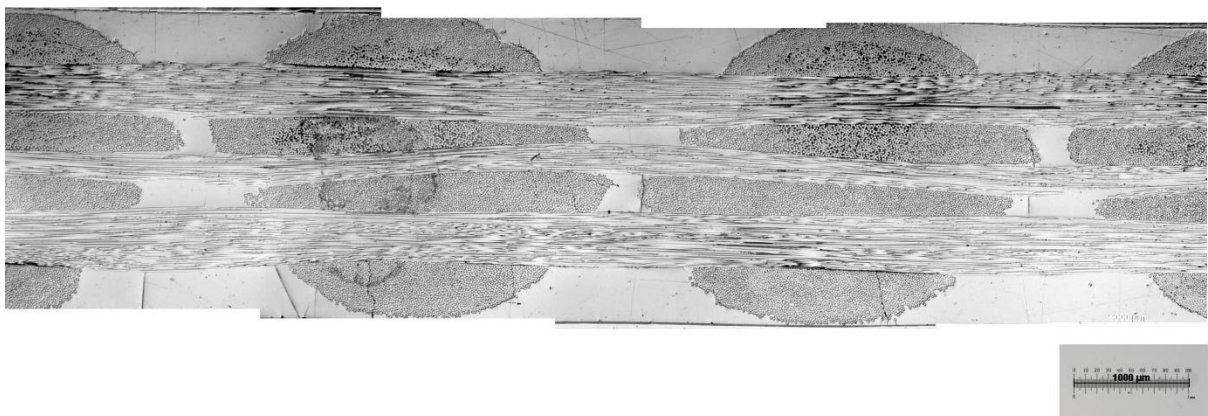


**Figure D.2** *Micrograph image taken from a specimen fatigued at a peak stress level of 150 MPa. The test was stopped after 100000 cycles.*

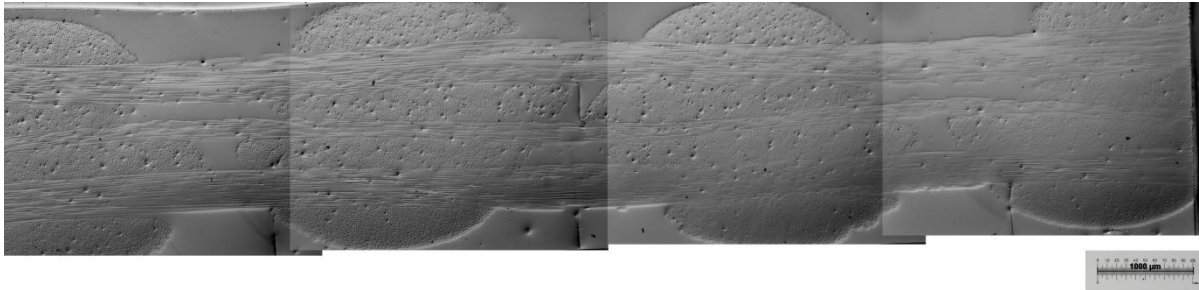


**Figure D.3** Micrograph image taken from a specimen fatigued at a peak stress level of 150 MPa. The test was stopped after 100000 cycles.

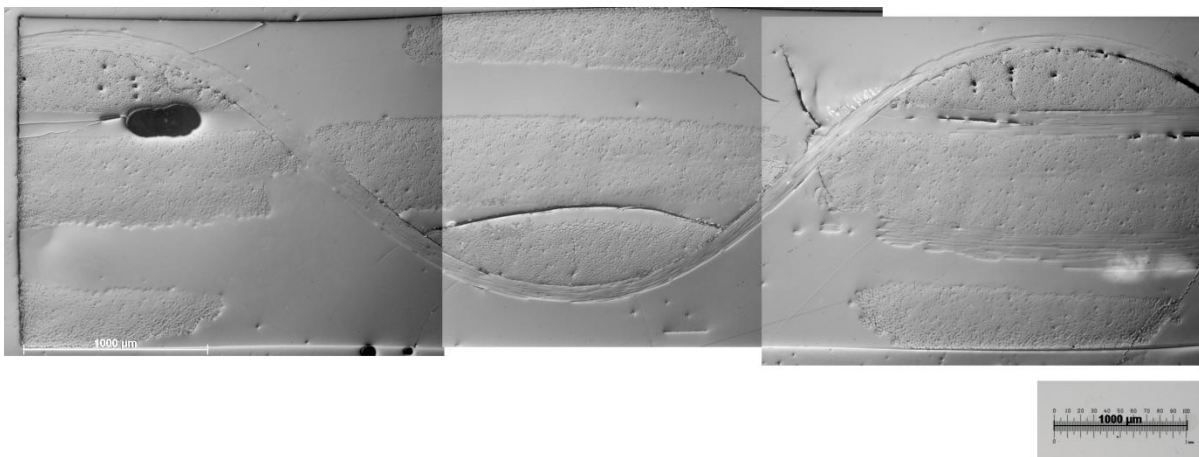


**Figure D.4** Micrograph image taken from a specimen fatigued at a peak stress level of 200 MPa along the weft direction until final failure of the specimen.

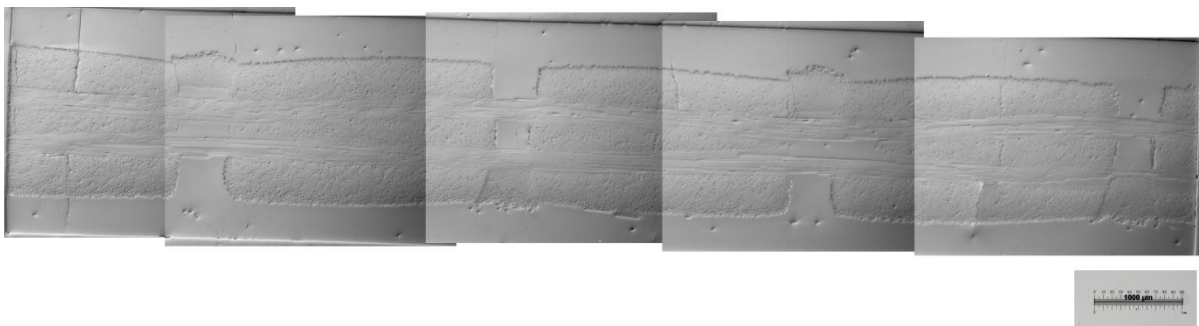


**Figure D.5** Micrograph image taken from a specimen fatigued at a peak stress level of 200 MPa along the weft direction until final failure of the specimen. The section plane is orthogonal to the warp direction.

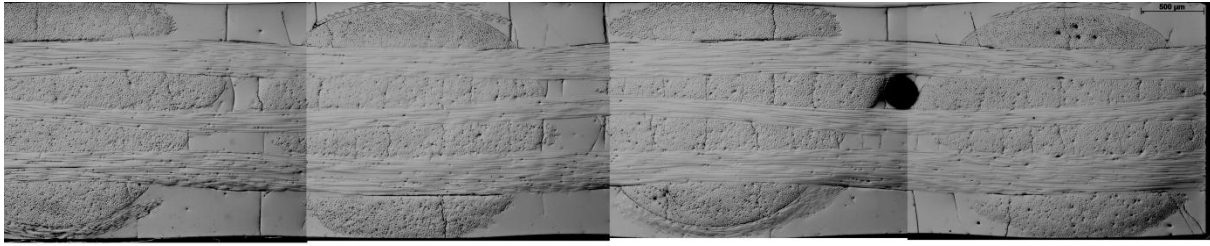


**Figure D.6** Micrograph image taken from a specimen fatigued at a peak stress level of 200 MPa along the warp direction until final failure of the specimen.

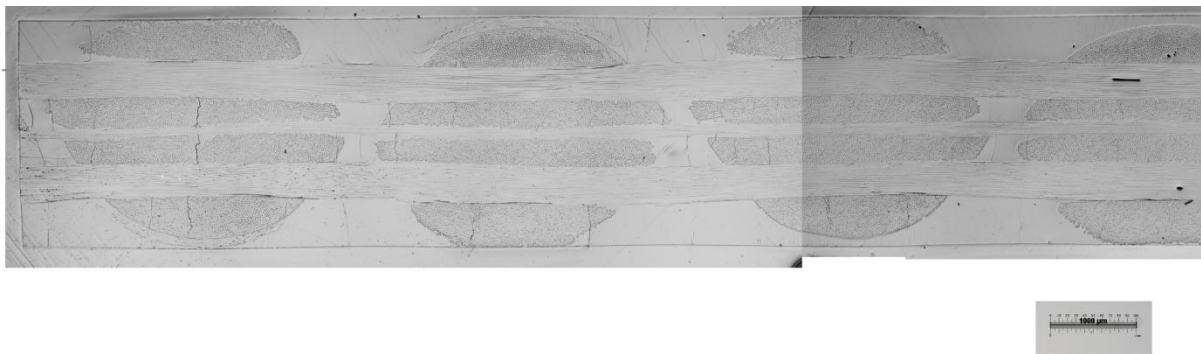


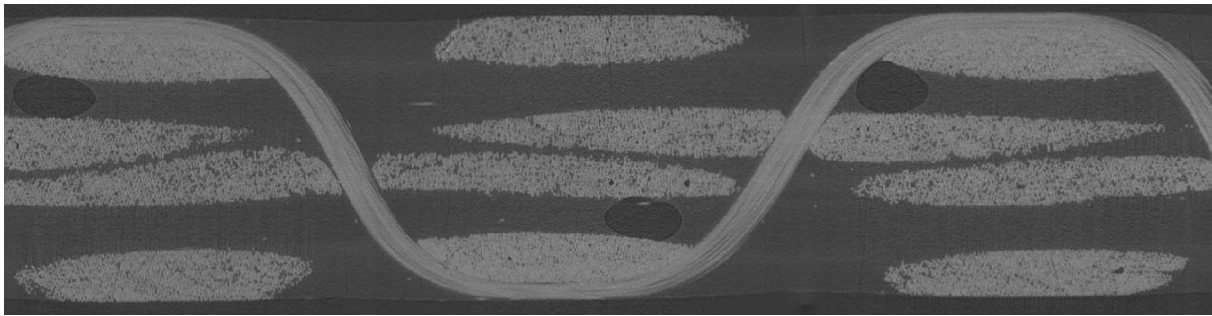
**Figure D.7** Micrograph image taken from a specimen fatigued at a peak stress level of 200 MPa along the warp direction until final failure of the specimen.



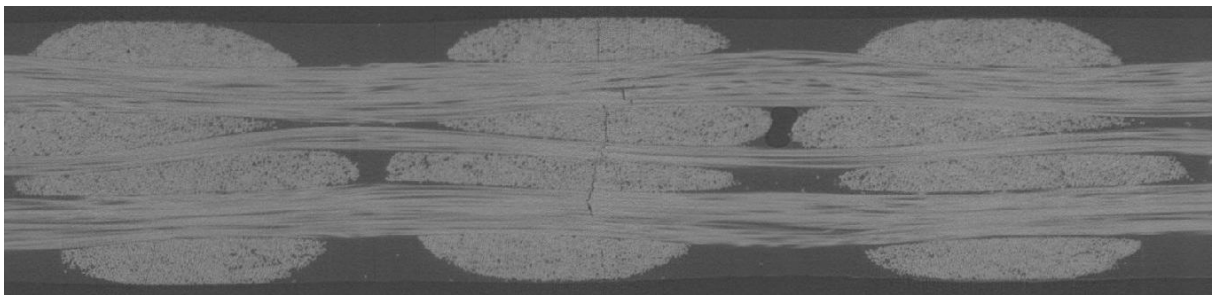
# Appendix E

## Micro CT images

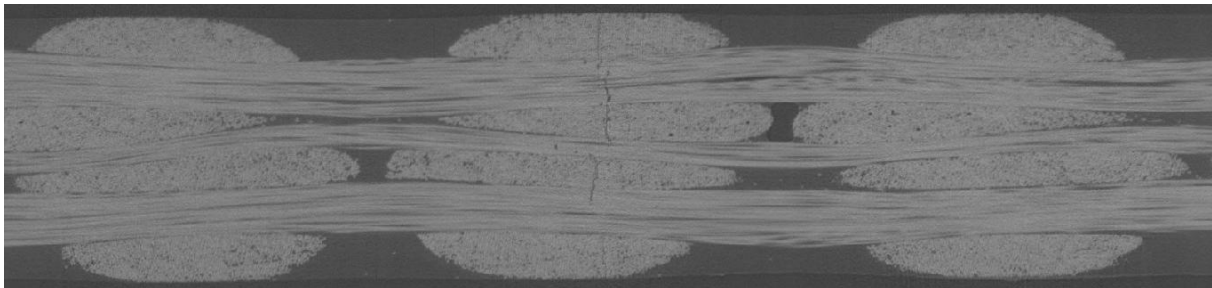
The following figures show a sequence of micro CT images taken from a specimen fatigued at a peak stress level of 200 MPa and brought in a condition near to failure. The sequence illustrate the development of the crack along the width of the coupon.



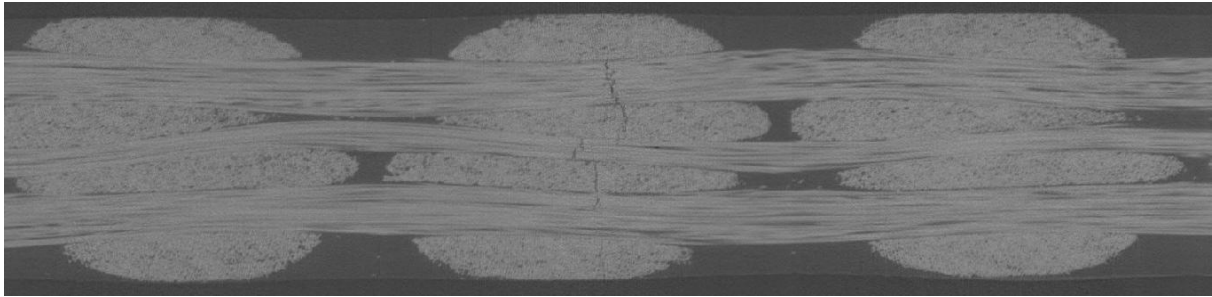
*a)*



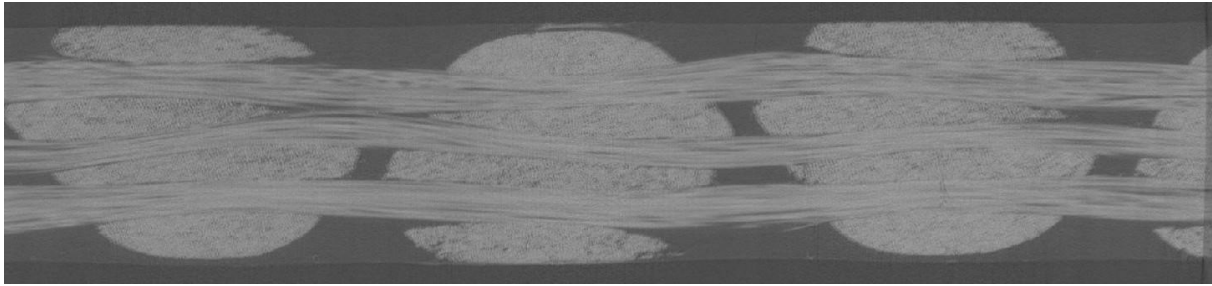
*b)*



*c)*



d)



e)

**Figure E.1** Sequence – a),b),c),d),e) – of micro CT images taken from a specimen fatigued at a peak stress level of 200 MPa near to failure.

# References

1. Baiocchi, L. (2013). Late Fatigue Damage Development in a 3-D Woven E-glass/Epoxy Composite M.Sc. Thesis Università di Padova.
2. Baiocchi, L., T.F. Capell, S.A. Mc Donald, S.L. Ogin, P. Potluri, M. Quaresimin, P.A. Smith, P.J. Withers, A. Bogdanovich (2013). Late-stage Fatigue Damage Development in a glass/epoxy non-crimp 3D orthogonal woven fabric composite. Proc:16th European Conference on Composite Materials, Seville, Spain, 22-26 June 2014.
3. Pagano, N.J. (1978). Stress Fields in Composite Laminates, *International Journal of Solids and Structures*, 14, 385-400.
4. K.Ko, Tsu-Wei Chou and Frank (1989). *Textile Structural Composites*, Elsevier science, Oxford, UK.
5. A.E Bogdanovich and M.H. Mohamed (2009). Three-Dimensional Reinforcements for composites, *SAMPE journal*, 45, 1-20
6. Chang, P., A.P.Mouritz, B.N.Cox (2007). Flexural properties of z-pinned laminates, *Composites Part A*, 38, 244-251
7. Bilisik, K.(2012).Three-dimensional braiding for composites: A review, *Textile Research Journal*, 83
- 8 Lomov, S. V., A. Bogdanovich, D. S. Ivanov, D. Mungalov, M. Karahan, I. Verpoest (2009). A comparative study of tensile properties of non-crimp 3D orthogonal weave and multi-layer plain weave E-glass composites. Part 1: Materials, methods and principal results, *Composites: Part A*, 40, 1134-1143.
9. Carvelli, V., G. Gramellini, S.V. Lomov, A.E. Bogdanovich, D.D. Mungalow and Verpoest I (2010). Fatigue behaviour of non-crimp 3D orthogonal weave and multi-layer plain weave E-glass reinforced composites. *Composites Science and Technology*, 70, 2068;
10. Mouritz, A.P. (2008). Tensile fatigue of properties of 3D composites with through-thickness reinforcement. *Composites Science and Technology*, 68, 2503.
11. S.Rudov-Clark, A.P. Mouritz (2008). Tensile fatigue properties of a 3D orthogonal woven composite, *Composites: Part A*, 39,1071.
12. Tong, L., A.P. Mouritz, M.K. Bannister (2002).*3D Fibre Reinforced Polymer Composites*. Elsevier, Oxford UK.



13. Bader, M G. and B L. Mok-Yeo, (1995. )Use of laser diffraction to detect sub-critical damage in E-glass Fibre/ Epoxy-resin laminates. Proc:3rd International Conference on Deformation and Fracture of Composites, Institute of Materials, Guildford UK, March 27-29.
14. Dharan, C K H, T.F.Tan (2010). Cyclic Hysteresis Evolution as a Damage Parameter for Notched Composite Laminates, *Journal of Composite Materials*, 44, 1977-1990
15. Varna, J., F. Paris, C. del Cano (1996).The effect of crack-face contact on fiber/matrix debonding in trasverse tensile loading. *Composites Science and Technology*, 57, 523-532
16. Correa, E., E.K. Gamstedt, F. Paris and V. Mantic (2007). Effects of the presence of compression in transverse cyclic loading on fibre-matrix debonding in unidirectional composite plies, *Composites Part A*, 38, 2260-2269.
17. Sutherland, L.S., R.A. Shenoi, S.M. Lewis (1998). Size and scale effects in composites: I. Literature review. *Composites science and technology*, 59, 209-220.
18. Zagenberg, J., P.Bronsted and J.W. Gillespie (2013). Fatigue damage propagation in unidirectional glass fibre reinforced composites made of a non-crimp fabric. *Journal of composite materials*
19. Ivanov, D.S., S.V. Lomov, A.E. Bogdanovich, M. Karahan and I. Verpoest (2009). A comparative study of tensile properties of non-crimp 3D orthogonal weave and multi-layer plain weave E-glass composites, Part 2: Comprehensive, *Composites: Part A*, 40,1134-1143
20. Naderi, M., M.M Khonsari, (2012). On the role of damage energy in the fatigue degradation characterization of a composite laminate, *Composites: Part B*, 45,528-537.
21. Naderi, M., M.M Khonsari, (2012). A comprehensive fatigue failure criterion based on thermodynamic approach. *Journal of Composite Materials*, 46, 437-447.
22. Topal, S., S.Ogin, A.Crocombe, P.Potluri (2014). Finite element modelling of 3D orthogonal non-crimp wovencomposites. Presented at 11th World Congress on Computational Mechanics (WCCM XI), July 20-25, 2014, Barcelona (Spain)
23. Zagenberg, J.H. (2013) The effects of fibre architecture on fatigue life-time of composite materials. Ph.D. Thesis, Technical University of Denmark DTU
24. 3TEX, Inc. [Online] <http://www.3tex.com/>. (last access: 05/08/2014)
25. Ashton, Poole and Ogin (2014). Private communication.



# Ringraziamenti

*Desidero ringraziare innanzitutto il prof. Marino Quaresimin, che ha reso possibile quest'esperienza e mi ha instillato la passione riguardo tutto ciò che ha a che fare coi materiali compositi ed il prof. Stephen Ogin, che mi ha insegnato molto, supportandomi con il suo entusiasmo e la sua serenità d'animo in tutti i mesi trascorsi a Guildford.*

*L'esperienza non sarebbe stata la stessa senza i miei mentori Serra Topal e Matthew Poole, a cui spetta un riconoscimento speciale. Soprattutto a Matthew, che mi ha aiutato sin dal primo giorno, facendo da Cicerone non solo tra i macchinari ma anche nella cultura britannica, cercando di spiegarmi (inutilmente) il senso del sarcasmo e dell'humor inglese.*

*Un ringraziamento va anche a Matteo e Nicolò, miei cari amici con cui ho condiviso le gioie e i dolori di questi cinque anni accademici.*

*Ma il riconoscimento più grande va alla mia famiglia, che si allarga a vista d'occhio (benvenuta Camilla!).*

*Ai miei fratelli, Marghe, Luca e Raffa, va un caro pensiero: senza il loro esempio e incitamento non sarei mai arrivata fin qui.*

*Ma è ai miei genitori che devo la dedica di questa tesi. Ci sono stati in ogni momento, brutto o bello che fosse, mi hanno sempre sostenuto dandomi forza e coraggio. Alla mia mamma, una leonessa, che ancora non capisce come possa aver studiato cose da uomini e a mio papà, che mi ha fatto toccar con mano le cose che studiavo, fossero motori o chissà cos'altro. Forza papà, adesso è il tuo turno di lottare!*

*A Mario va il pensiero più dolce, con il suo sostegno e il suo affetto mi è stato vicino in tutti questi anni, costituendo la mia roccia e riparo. Grazie amore mio.*

# Acknowledgements

*I want to thank first of all prof. Marino Quaresimin, who made this experience possible and instilled in me the passion about everything that has to do with composite materials and prof. Stephen Ogin, who taught me a lot, sustaining me with his enthusiasm and his serendipity in all the months I spent in Guildford.*

*The experience would not have been the same without my mentors Serra Topal and Matthew Poole. Especially Matthew, who has helped me from day one, making my Cicero not only about the machinery but also in British culture, trying to explain (unsuccessfully) the sense of sarcasm and English humor.*

*Thanks also to Matteo and Nicolò, my dear friends with whom I shared the joys and sorrows of these five academic years.*

*But the greatest recognition goes to my family, which widens to the eye (welcome Camilla).*

*To my brothers and sisters, Marghe, Luca, and Raffa, goes a dear thought: without their example and encouragement I would never have come this far.*

*But it is to my parents that I have to dedicate this thesis. They have been present all times, ugly or beautiful they were, have always supported me, giving me strength and courage. To my mother, a lioness, who still does not understand how I could have studied 'men-stuff' and to my dad, that made me experience first-hand the things that I studied, they were engines or whatever.*

*To Mario goes the sweetest thinking, with his support and his love he stood by me all these years. Thanks my love.*